

Noble Metal Clusters and C₆₀-Buckminsterfullerenes on Carbon Surfaces: A Photoelectron Spectroscopy Study

Inauguraldissertation

zur
Erlangung der Würde eines Doktors der Philosophie

vorgelegt der
Philosophisch-Naturwissenschaftlichen Fakultät
der Universität Basel

von
Michael Büttner
aus Göttingen (Deutschland)

Basel, 2006

Genehmigt von der Philosophisch-Naturwissenschaftlichen Fakultät
auf Antrag von

Prof. Peter Oelhafen
Prof. Christian Schönenberger

Basel, den 14.2.2006

Dekan Prof. Hans-Jakob Wirz

Contents

Abstract	v
Foreword	vii
Overview of Chapters	xi
1 Introduction	1
1.1 History of Metal Clusters	1
1.1.1 Motivation for Modern Metal Cluster Research	2
1.2 Introduction to Fullerenes	4
2 Experimental Methods	7
2.1 Sample Preparations	7
2.1.1 Deposition Methods	7
2.1.2 Preparation of thiol-passivated gold clusters	9
2.2 Photoelectron Spectroscopy (PES)	10
2.2.1 PES basics	10
2.2.2 Photoelectron Spectroscopy Applied to Metal Clusters	13
2.2.3 PES Setup at the ESCA Laboratory	16
2.2.4 Experimental Parameters Used in This Work	21
3 Results	23
3.1 Thiol-Passivated Nanoparticles	23
3.1.1 X-ray Radiation Damage of Thiol-Passivated Gold Particles	23
3.2 Thiol-gold Interactions	32
3.2.1 Noble Metal Cluster Nucleation on Carbon Substrates	32
3.2.2 Thiol Adsorption on Noble Metal Clusters	44
3.2.3 Ongoing Work / Outlook	52
3.3 C ₆₀ on Carbon Substrates	54
3.3.1 Adsorption / Desorption Studies	54
3.3.2 Comments on Deposition Methods	60
3.4 Summary of Main Results	63
A Supplementary Information	65
A.1 Photoelectron Spectroscopy in the Historical Context	65
A.2 Evaporation of Metals on Surfaces	67
A.2.1 Classical Treatment of Thin Film Growth Processes	67
A.2.2 Computational Simulations	70
A.3 Towards Thiol-Passivated Nanoparticles	72
A.3.1 Sample Preparation Techniques	73

A.4	A Pedestrian's Guide to Band Structure Calculations	76
A.4.1	Density Functional Theory	76
A.4.2	Car-Parrinello Molecular Dynamics (CP MD)	78
	Bibliography	81
	Acknowledgments / Danksagung	89
	Curriculum Vitae	91
	Publications	93

Abstract

In this work the growth of noble metal clusters on defect-rich carbon surfaces and their interaction with thiol molecules was studied by means of monochromatized X-ray Photoelectron Spectroscopy. Motivated by the growing interest in nanoparticle research and the demand for extensive knowledge of particle properties, studies were performed to investigate the stability of chemically synthesized thiol-passivated gold nanoparticles. In addition, thiol-cluster interactions were more thoroughly examined by preparing clusters under vacuum conditions and exposing them to a thiol atmosphere. Results show that thiol-gold interaction has significant impact on the clusters' electronic configuration hinting to a thiol-induced metal-insulator-transition.

Furthermore, C_{60} molecules deposited on carbon surfaces were studied with Ultraviolet Photoelectron Spectroscopy. Their interaction with surface defects was elucidated by temperature-controlled desorption experiments. It will be reported that fullerenes on defect-rich carbon surfaces are more stable against desorption than on pristine Highly Oriented Pyrolytic Graphite (HOPG). This result is interesting with respect to applications based on surface nanostructuring by Focused Ion Beam techniques.

Foreword

The nano world – A world populated by objects and structures of dimensions in the order of 10^{-9} m. It forms a bridge between the atomic (10^{-10} m) and the macroscopic scale. In solid state physics it represents a transitional state of materials between atomic and bulk properties. In chemistry it stands for the molecular scale of fullerenes, benzene rings and more complex structures. It corresponds to the length scale of DNA strands, enzymes, cell double walls and other subjects of biological research. The semiconductor industry is approaching the lower nanoscale region with their still ongoing downscaling of logic circuits in modern computer chips. Nanometer sized objects present a challenge and also an opportunity for human medicine, since such particles are able to traverse the blood-brain barrier and may do either good or harm there. The impact on human health is probably the most important issue that has to and is going to be discussed now and in the future to be able to handle the emerging nano science business. On the other hand nano science brings together the different scientific professions and allows fruitful interdisciplinary research and development probably never encountered before.

It is clear that one has to be able to reliably tailor and manipulate nanometer structures to obtain good experimental results and to apply the gained knowledge to the development of new devices (e.g., quantum computing, molecule sensors, etc.). Therefore, new instruments and tools had and still have to be conceived and built in order to handle nanometer-sized objects. The advent of scanning probe microscopy, beginning with Scanning Tunneling Microscopy (STM) in 1981 started a new era as it allowed to image surface structures down to the atomic scale for the first time. The same method turned out to be also applicable to the creation and manipulation of such structures and to locally measure certain properties (e.g., conductance, friction). Progress in chemical synthesis methods enlarges the availability of nanoparticles with respect to material composition, quantity and quality. Exploitation and optimization of self-assembly mechanisms provide ordered structures on a larger scale.

Nanostructured objects (e.g., nanoparticles) are expected to exhibit physical properties diverging from those of the bulk material, as quantum effects play an increasingly dominating role when reducing the size in this length scale. This provides an excellent chance to study the transition from atomic to bulk behavior and to better understand the underlying quantum nature. Due to the small dimensions interfacial properties become important as they may be the governing part defining properties of the whole particle. For clusters consisting of 10^3 atoms approximately 40% of them are surface atoms. For a total of 10^2 atoms this value increases to nearly 90%!¹ Therefore, the influence of the cluster's environment (organic shell, supporting substrate, etc) on its properties has to be known to tailor them to individual needs.

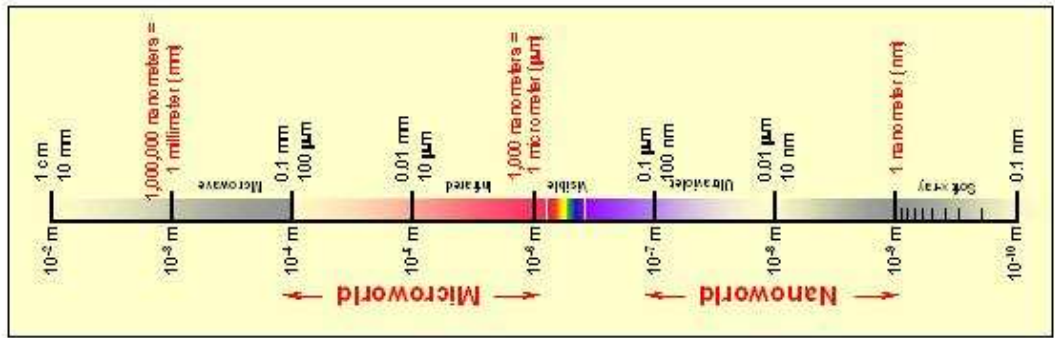
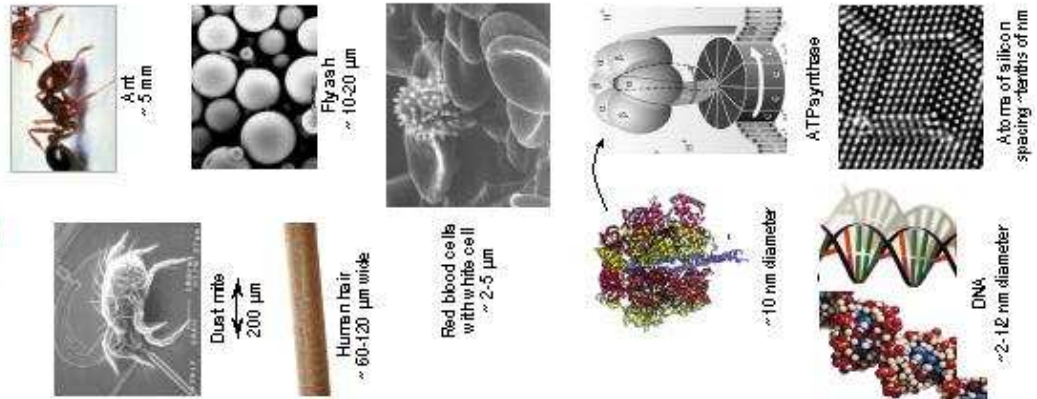
Photoelectron Spectroscopy, a long established and commonly used analytical method in surface science, represents a very useful tool for studying nanoparticles. Its surface sensitivity qualifies it for studying supported particles on substrates, while its elemental and chemical sensitivity provides information about the electronic configuration of particles, surfactant molecules and the substrate. However, unlike STS (Scanning Tunneling Spectroscopy), which is a highly

¹The simple calculation projects the cross-sectional area of an atom onto a sphere surface, cf. Ref. [2]

local probe, photoemission spectroscopy averages over an area orders of magnitude larger than the structures under investigation. Furthermore, the photoemission process results in expulsion of a photoelectron, and thus, the final state consists of an ionized atom. These issues have to be considered for the interpretation of photoelectron spectra. Some impose unavoidable limitations (final-state effect), other can be overcome by preparative improvements (smaller size dispersion in chemical synthesis, removal of organic residues).

The Scale of Things – Nanometers and More

Things Natural



Things Manmade

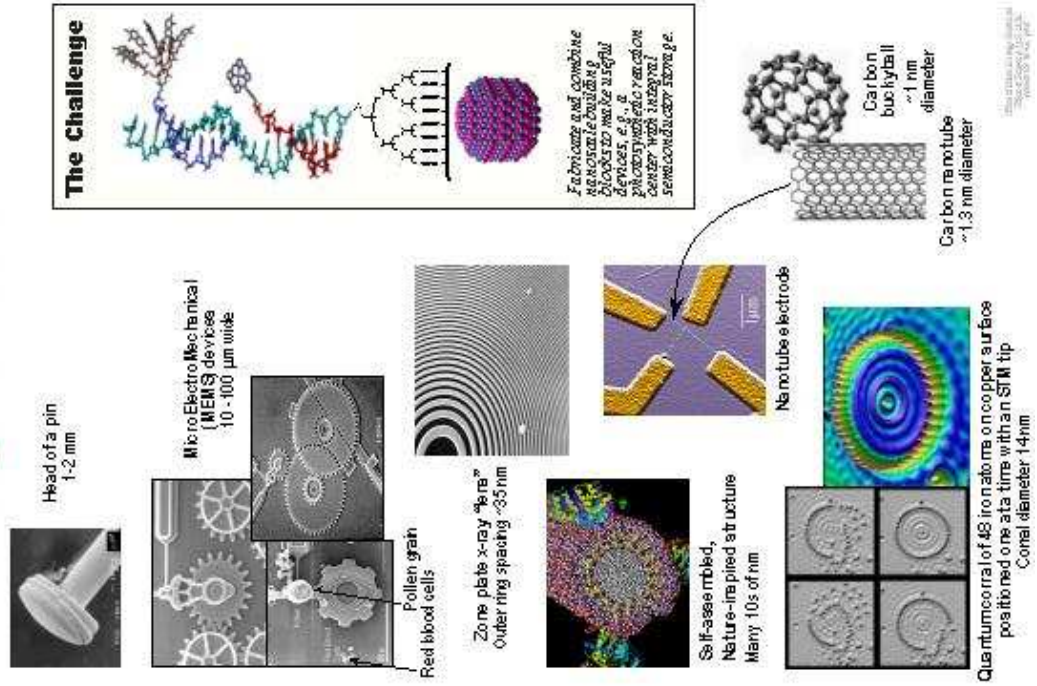


Figure 1: Comparison of length scales for different cell objects in nature and technology (from [1])

Overview of Chapters

In the first part of this work studies on noble metal clusters (gold and silver) and their interaction with alkanethiol molecules are presented. The second part examines buckminsterfullerenes (C_{60}) supported on carbon substrates and their stability against thermal desorption. Photoelectron Spectroscopy (X-ray and Ultraviolet) was employed as the primary analytical method for the studies. The common part that is linking the different subjects can be summarized as ‘interface properties’, as the studies investigate both cluster-substrate and molecule-gold interfaces. The chapters of this text are organized as follows:

Introduction This part gives a short overview of metal clusters in a historical context and outlines the motivation for modern nanoparticle research. It introduces the reader to fullerene molecules and some of their most important features.

Experimental methods The preparative methods are shortly described and a more detailed introduction to Photoemission Spectroscopy with focus on the study metal clusters will be given.

Results The discussion of the experimental results is divided as follows:

- Investigations on thermal stability and X-ray induced damage of chemically synthesized thiol-passivated gold nanoparticle
- Studies on the nucleation and growth of noble metal clusters on defect-rich carbon substrates and on the influence of adsorbed thiol molecules on the particles’ electronic configuration.
- Examination of thermal desorption of C_{60} molecules from carbon surfaces and changes in spectral features due to interaction with surface defects..

Each section is preceded by a short introduction about the motivation and relevance of the study and a more detailed description of the experiment.

Appendix (Supplementary Information) Background information on the history of Photoelectron Spectroscopy, surface processes of cluster nucleation and growth, chemical routes of nanoparticle synthesis and introduction to Density Functional Theory.

Chapter 1

Introduction

1.1 History of Metal Clusters

Though nanoparticle research appears to be a quite modern subject (partly owed to the nowadays availability of suitable instruments for manipulation and analytical devices), metal clusters were already put into application in antiquity. Noble metals, for example, played an important role in the coloring of glasses and ceramics. One of the most famous examples is the roman Lycurgus Cup, dated between 5th and 4th century B.C.. It transmits ruby-red and reflects green light, see Fig. 1.1a. Examination with modern equipment revealed gold (40 ppm) and silver (300 ppm) clusters present in the cup (Fig. 1.1b).[4] It is likely that the roman glassmaker obtained this results as an accident as this excellent work remained unique.[3]

In the 17th century colored glasses were studied and refined in a more systematic manner. Gold was used to produce deep red or purple colors, like the *Purple of Cassius*, named after Andreas Cassius, who developed the method around 1685. Johann Kunckel perfected the procedure in 1700, obtaining *gold-ruby* colored glasses.[5] Molten glass can easily dissolve up to 0.1% gold ($\approx 0.01\%$ typically used for gold-ruby color) and retains its clear and colorless appearance when cooled in the usual, rapid step. The cooled, gold-containing glass has to be reheated to 600-700 °C. At this temperature supersaturation of gold is reached and precipitation of gold crystals initiates, assisted by antimony and cerium oxide additives. This process is called *striking* and lasts several hours during which clusters grow, reaching sizes between 1-10 nm. Glass composition, temperature and striking time have to be carefully controlled to get high-quality glass. In a similar manner, silver and platinum were employed to get coloring

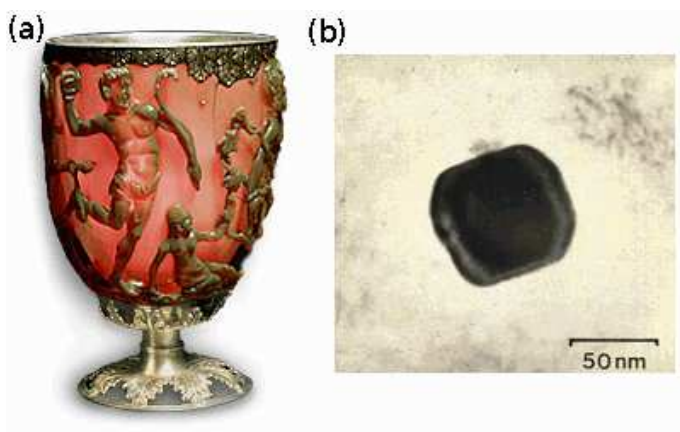


Figure 1.1: Left: The Lycurgus Cup. It appears red for transmitted and green for reflected light. Right: Transmission Electron Micrograph revealing metal clusters present in the glass. (from [3])

of yellow and pink, respectively. Due to the difficulties in manufacturing, such glasses were precious and only used for luxury glassware and church windows. At that time, of course, the existence of nanoparticles was unknown and it was not until 1857 that Faraday found out about the significance of small particles on coloring when he dissolved colloidal gold particles and observed the same deep ruby color.

In the Middle Ages colloidal gold potions were considered to have curative powers for many different diseases, such as heart and venereal problems, epilepsy, tumors, and for the diagnosis of syphilis. However, these beliefs were mainly based on superstition. A detailed description of the different medical applications was given in a book by F. Antonii, probably the first book on colloidal gold, written in 1618.[6] Even today there is a huge business about noble metal colloids promising the most fabulous healing capabilities. This, however, is just a good (or bad) example of marketing.

1.1.1 Motivation for Modern Metal Cluster Research

The point that makes nanoparticles scientifically interesting nowadays is the fact that they represent a kind of transition state between atom and bulk solid. Therefore, the investigation of physical and chemical properties of clusters may reveal new surprising features giving insight to fundamental issues of solid state physics (e.g., origin of catalytic activity, metal-insulator transitions, experimental verification of theoretical predictions). The reader shall be reminded that semiconductor nanoparticles (e.g., Si, GaAs) and clusters consisting of more than one atomic species (e.g., FePt) represent large and active fields of nanoscience, too. They are, however, beyond the scope of this work.

The electronic configuration (the *initial-state*) of nanosized particles is known to be different from the bulk state.[7, 8] As electrons define most of a solid's physical and chemical nature, nanoparticles can be expected to show behavior absent for the bulk material. For example, metals can exhibit isolating behavior when reduced to small particles. This can be explained with a simple model which takes into account the density of states at the Fermi energy. In large enough clusters or bulk material individual electronic states form a continuum, the band structure. For small particles the band structure starts to exhibit discrete levels corresponding to a transition to atomic structure and arising due to spacial confinement of conduction electrons. If the energetic difference δ between the levels exceeds values for thermal energies, the cluster can be expected to show nonmetallic behavior. The critical particle size can be estimated by the *Kubo criterion*: [9]

$$\delta \approx \frac{2}{3} \frac{E_f}{N_A z} > k_B T \quad (1.1)$$

where N_A is the number of cluster atoms, z their valence and E_f the width of the conduction band. For gold ($z = 1$) one finds $\delta \approx 8 \text{ eV}/N_A$. This means clusters with less than 320 atoms are necessary to increase the level spacing above the ambient temperature (25 meV), implying that the discrete nature of energy levels can be observed at room temperature only for very small particles. Certainly this model is very crude and does not take into account changes of the electronic configuration being part of the quantum size effect (QSE), but it gives an upper size limit of when QSE's are to be expected. It also illustrates that metal-to-insulator transitions are an intrinsic feature arising with decreasing particle size. This has to be distinguished from metal-insulator-transitions due to chemical interaction (e.g., oxidation) with the environment. The thermodynamic properties of small particle are known to be different to the ones of the bulk material. Due to the highly increased ratio of surface atoms such cluster can exhibit a lowered melting point.[10, 11]

Nanoparticles are interesting for a variety of electronic applications, such as Single-Electron Transistors (SET),[12, 13] diodes[14], quantum dots[15, 16] and as electronic contacts to molecules.[17] The investigation of optical properties of individual clusters and cluster arrays is a very active field.[18, 19, 20, 21] Catalytic activity can be strongly enhanced for nanosized metals that normally do not or do only weakly show such behavior as bulk material[22, 23]. Much effort is put in the examination of such finite-size effects, as they promise to be useful for future application.[24] In this context it is clear that *cluster-substrate interactions* and their thorough investigation become increasingly important as research shifts from fundamental studies of intrinsic cluster properties to the development of devices. This is a future challenge for surface science and its set of analytical tools.

Different chemical and physical techniques to grow nanoparticles have been developed,[17, 25, 26, 27]. In contrast to physical methods wet chemical procedures usually have the advantage of yielding macroscopic amounts of particles. Using sophisticated recipes different kinds of molecules can be attached to the clusters. This allows to synthesize *passivated* particles, i.e., particles with surrounded by a shell of organic molecules, preventing particle aggregation and stabilizing them.[28, 29] However the statistical nature of particle growth normally leads to a distribution of cluster sizes. In most cases this cannot be overcome totally, but reduced to a minimum by optimization of the chemical procedure or additional size separation steps (e.g., centrifuging, High Performance Liquid Chromatography (HPLC)).[30, 31] Physical methods may provide size-selected particles, however, with usually much lower yields. Organic shells around the particles play a crucial role in the so-called *self-assembly*. Particle-particle and particle-support interaction promotes the organization of clusters in well-ordered structures. Such a mechanisms are mainly determined by the nature of shell molecules.[32]

The above discussions make it obvious that a detailed knowledge of nanoparticle properties and their dependence on the cluster's environment (like passivating molecules) is of primary interest in order to build nanoscale structures.

1.2 Introduction to Fullerenes

Fullerenes represent the third allotropic form of carbon (with diamond, graphite). They were first observed in mass spectra of laser ablated graphite by H. Kroto (University of Sussex) and R. Smalley (Rice Univ., Houston) in 1985.[33] They detected unusually stable carbon clusters consisting of 60 and 70 atoms. The same group came up with a model of the C_{60} molecule having a soccerball shape (truncated icosahedron) with 12 pentagons and 20 hexagons, built by threefold-linked carbon atoms. The pentagons, which are not present in graphite layers, allow to bend the carbon sheet to build up the closed fullerene structure. The model of such molecule is shown in Fig. 1.2. It is often referred to as a *buckminsterfullerene* or buckyball.¹ Among the different fullerene species, the C_{60} molecule is the most popular and most studied one.

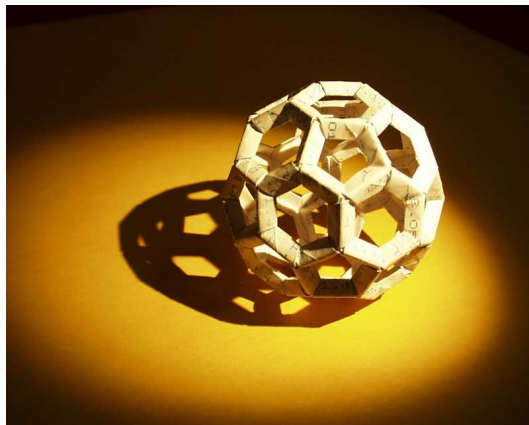


Figure 1.2: Origami model of C_{60} . (Courtesy of T. de los Arcos)

Although there also exist larger fullerenes with more atoms (macroscopic amounts of C_{100} have been successfully synthesized), C_{60} has undoubtedly the highest scientific popularity and the discussion will be therefore primarily focused on this species. C_{60} molecules are composed of carbon atoms that exhibit a hybridization state somewhat in between sp^3 (diamond) and sp^2 (graphite). Each atom connects to three neighbors, which is comparable to sp^2 bonds. However, the three bonds are not exactly in-plane due to the molecule curvature and therefore the π -orbital perpendicular to the bonds is partly hybridized with an s orbital. The s-character increases with increasing curvature. Fig. 1.3 illustrates the dependency between the pyramidalization angle and the π -orbital s-character. The data are calculated values and are obtained by applying the so-called π -orbital axis vector (POAV) theory.[35, 34] A quantitative estimation for the hybridization yields $s^{2.278}$ with a fractional s-character of the π -orbitals of 0.085. Due to the high symmetry of the C_{60} molecules each carbon atom experiences identical chemical environments.[36] C_{60} has a very large electron affinity and in electrochemical voltammetry² experiments up to five electrons have been successfully added to the molecule in solution.[37] The closed-shell electronic structure leads to an energetic gap between the highest occupied molecular orbital (HOMO) and the lowest unoccupied molecular orbital (LUMO) of ≈ 2.3 eV (experimentally determined).[38] The valence band electrons on each carbon atom are hybridized into three strongly localized σ -bonds and one less localized π -bond perpendicular to the surface. The σ -bonds are 3 to 6 eV below the Fermi energy. Therefore, the states near E_f (taking part in electronic and optical interactions) are dominated by π -electrons. In a C_{60} molecule, for example, 60 π -electrons have to be distributed into molecular orbitals. Fig. 1.4 shows calculated molecular orbitals and the corresponding symmetric classification obtained by tight-binding or *Hückel-methods*. [39] “+” and “-” denote filled and empty states, respectively.

¹Buckminster Fuller (1895-1983) studied mathematics in Harvard and, after finishing his studies, devoted himself to the investigation of new design and architectural concepts. His principles were based in minimizing energy and material consumption in industrial construction (of cars, buildings). His most famous work was the geodesic dome (right), a lightweight roof construction meant to be used as a multi-purpose space for industry, military, trade fairs, etc.



²A method to determine oxidation and reduction potentials of molecules. Performed in liquids, a changing potential is applied between two electrodes and the current measured.

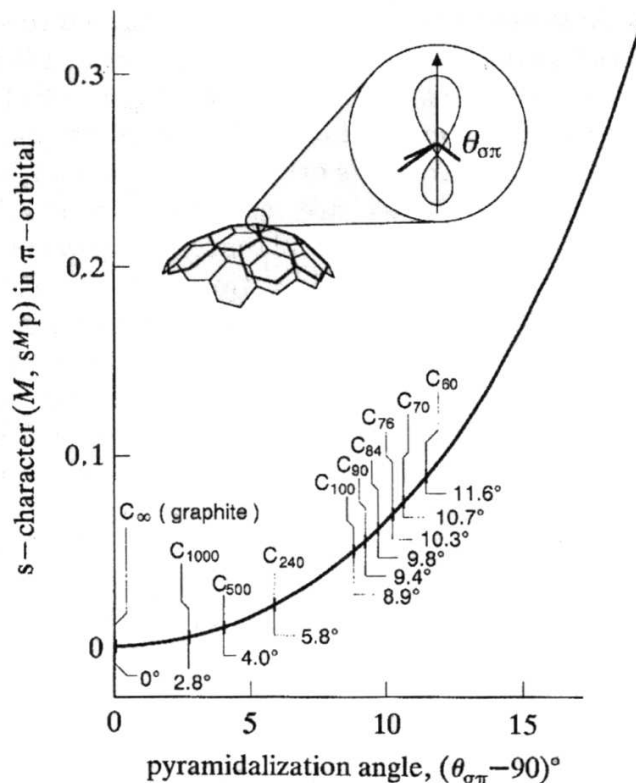


Figure 1.3: Carbon atom hybridization for different fullerene species. The increasing s-character in the π -orbitals is a consequence of the fullerene surface curvature distorting the planar sp^2 -geometry.[34]

In this scheme, the HOMO-LUMO gap can be found between levels with h_u (occupied) and t_{1u} (unoccupied) symmetry.

C_{60} can be crystallized forming a solid material, called *fullerite*. The buckminsterfullerene building blocks arrange in a close-packed face centered cubic (fcc) lattice, held together by van-der-Waals forces. Similar to inter-planar bonds between graphite sheets, this weak interaction results in a low material hardness. When heated up C_{60} powder sublimates between 500-600 °C. Because of the closed structure of the individual fullerene building blocks, the material retains most of its molecular features (electronic, optical) in the solid state. Furthermore, NMR investigations revealed, that fullerene molecules rapidly rotate, even in solid state due to the low binding forces between each other.[40, 41]

One would expect the fullerene to be chemically rather inert, as the closed geometry suggests. However, this is not true. For example, deposition on molybdenum promotes decomposition of the molecular cage due to chemical reactions with the Mo surface.[42] Chemical modifications of the cage can be applied to attach functionalized molecules.[43, 44] Ultraviolet and electron irradiation has proven to induce polymerization within a deposited fullerene film.[45, 46, 47] If brought in contact with a metal, electrons are transferred to the fullerene cage filling unoccupied states (LUMO) above the HOMO. These additional electrons create an increased intensity at near the Fermi level, thus enhancing conductivity.[48, 49, 50] Endohedral doping has been successfully applied, e.g., on alkali atoms, which donate their conduction electrons to the C_{60} cage filling empty LUMO states. Superconductive behavior has been observed for such systems.[51, 52]

Since their discovery fullerene molecules have been studied to a great extent. Due to the availability of macroscopy quantities, C_{60} and C_{70} , respectively, have been and still are object to many investigations exploring new applications for these exceptional molecules. Their closed-

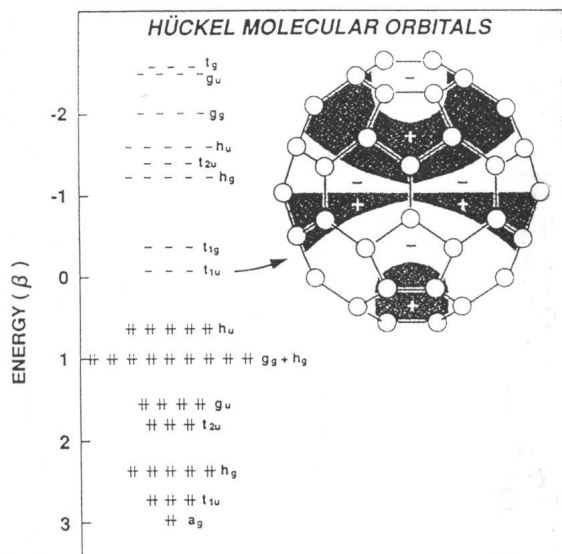


Figure 1.4: Configuration of the occupied and unoccupied Molecular Orbitals (MO) of a buckminsterfullerene showing the degeneracy of the levels and their corresponding symmetry group. The molecule model illustrates the orientation of the LUMO wavefunction.

cage structure makes fullerenes promising candidates for use as nanoscale building blocks in many fields of research. They are widely employed in physics, chemistry and medical research as scaffolds to attach functionalized molecules and to tailor the physical and chemical properties to the individual needs (e.g., novel solar cell materials, drug delivery, optical limiters).[44, 43]

The application of fullerenes as scaffolds decorated with functionalized molecules suggests to examine possibilities to build nanostructures out of these functional units. A first step therefore would be to investigate methods to deposit fullerene molecules on substrates in a controlled manner.

Chapter 2

Experimental Methods

A short and general description of the experimental methods is presented in this part. Photoelectron Spectroscopy will be introduced more elaborately. More details concerning the experiments will be given later in the *Results* section when the corresponding studies are discussed.

2.1 Sample Preparations

2.1.1 Deposition Methods

Noble metals

Submonolayers of gold and silver were deposited using an electron beam evaporator (Omicron EMF), as shown schematically in Fig. 2.1. Small pieces of the metal are placed in the molybdenum crucible. The crucible is electrically isolated from the rest of the device and connected to a high voltage power supply. Electrons are emitted from a surrounding filament and accelerated to the biased crucible, heating it up by electron impact. The source parameters (HV, filament emission current) have to be thoroughly adjusted to obtain a stable deposition rate. Typical values for gold and silver are 900 V and 14 mA emission current. In a well baked-out system deposition could be performed under good UHV conditions (order of 10^{-9} mbar). The divergence of the metal vapor beam is small, resulting in a spot size slightly larger than the sample holder (≈ 20 cm distance). This prevents other devices from being spoiled during deposition. The source is equipped with a shutter mechanism to quickly block the vapor beam when the deposition is finished.

Amorphous Carbon

The carbon thin films used throughout this work were grown by magnetron sputtering of a graphite target in an argon atmosphere. Silicon (with native oxide layer) was used as substrate and has been ultrasonically cleaned in acetone and ethanol before transfer to the vacuum system. The magnetron was driven by a DC power supply operating at 20 W. The argon partial pressure was $5 - 10 \times 10^{-3}$ mbar.

Fullerenes

High purity (99.95%, MERCorp) C_{60} powder was employed in this study. Two different sources have been used to deposit C_{60} molecules: The electron beam evaporator described above and a home-made sublimation source. For the e-beam evaporator the setup was the same as for metals, however, much lower values for high voltage and emission current were chosen. The

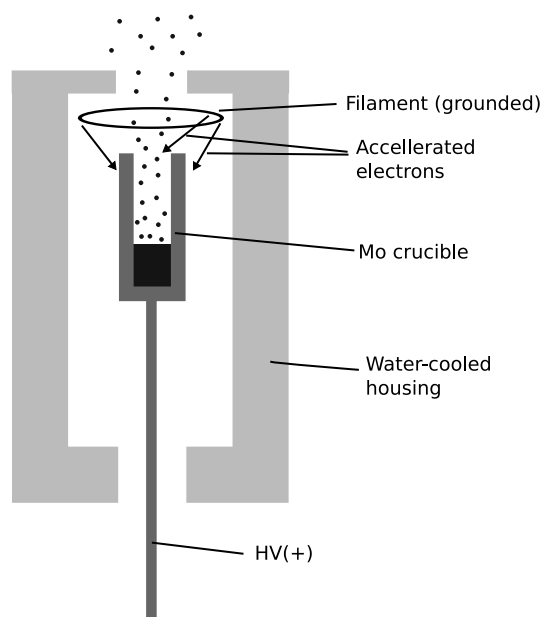


Figure 2.1: E-beam source (Omicron) schematics: The crucible is connected to high voltage and is heated by electron impact.

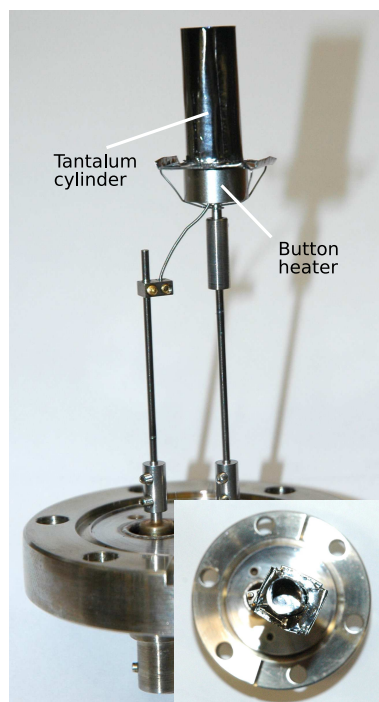


Figure 2.2: Home-made fullerene sublimation source: A cylindrical tantalum crucible mounted on a button heater. The device is held only by the heater contacts to improve thermal isolation.

voltage had to be chosen as low as possible in order not to damage the fullerene cages by electron impact. Typical values were 300 V and 5 mA.

In order to compare two different deposition methods, a sublimation source was built as displayed in Fig. 2.2. It consists of a resistive button heater mounted underneath a tantalum cylinder, which contains the fullerene powder. To reduce thermal losses to a minimum the whole device is held only by the button heater leads fixed to electrical feedthroughs. Approximately 30 W have to be applied to the heater to begin fullerene sublimation. To reduce time spent to reach thermal equilibrium the heater was not fully switch off between depositions, but the power was put below the sublimation threshold. This slow degassing may also improve the purity of the fullerene powder.

Films Thickness Measurement

The deposition rate was measured with a quartz crystal microbalance. The fundamental frequency f is a function of the amount of deposited material. If f is known the thickness T can be calculated using the *Sauerbrey* equation

$$T = - \left(\frac{N_q d_q}{d_f f_q^2} \right) (f_c - f_q), \quad (2.1)$$

where T = film thickness (cm), d_q = density of quartz (g/cm^3), d_f = density of the film (g/cm^3), N_q = frequency constant for AT-cut quartz crystal (Hz/cm), f_q = oscillation frequency for unplated quartz (Hz) and f_c = oscillation frequency for loaded quartz (Hz). This equation yields sufficiently accurate results if the frequency shift $f_q - f_c$ is less than 2% of f_q .

The oscillation is measured by a frequency counter (HP 5334B), which is connected to a computer via IEEE GPIB interface. A home-written labview program communicates with the counter and reads out its data. The measured values are continuously plotted in a graph displaying data of a 20-30 min time span. This feature is especially important when a high stability of the deposition rate is needed.

2.1.2 Preparation of thiol-passivated gold clusters

The chemical synthesis of passivated gold particles has been performed by Thomas Belser during his PhD studies in the group of Prof. A. Pfaltz, Institute of Organic Chemistry, Basel. The purified and dried colloids were dissolved in toluene. Small drops of the solution were put on freshly cleaved HOPG substrates. A short description of the chemical steps can be found in Sec. A.3

2.2 Photoelectron Spectroscopy (PES)

2.2.1 PES basics

Photoelectron spectroscopy¹ nowadays is in principle performed in the same way it has been done 100 years ago. The sample under investigation is irradiated with light and due to the photoelectric effect electrons are emitted from the sample. The kinetic energy of the excited electrons is then determined by an electrostatic analyzer. Thus, if the energy of the impinging photon $h\nu$, the kinetic energy of the photoelectron E_{kin} and the sample's workfunction Φ is known, one can calculate the binding energy E_B of the state the photoelectron was in before photoexcitation.

$$E_B = h\nu - \Phi - E_{kin} \quad (2.2)$$

In this term, the binding energy is given with respect to the vacuum level E_{vac} , which is usually done for spectroscopy of free atoms and molecules. However, for experiments on solids (which is the case here) one chooses the Fermi level as the reference point for binding energy determinations and avoids the necessity to deal with (often unknown) workfunctions Φ . The different excitations sources used in photoelectron spectroscopy cover a wide spectrum of photon energies: several ten eV (UV-light), using gas-discharge lamps, to several hundred or thousand eV (soft / hard X-rays) by means of X-ray tubes. Synchrotron facilities represent quite sophisticated light sources. Their photon flux is several orders of magnitude larger than conventional X-ray tubes. The energy of the monochromatized light can be chosen over a wide range, covering UPS and XPS. Each energy range has certain advantages and disadvantages (e.g. information depth, photoemission processes, sensitivity), some of which will be addressed in this work. Nevertheless, the variety of available light sources make photoelectron spectroscopy a versatile surface science tool and allows to obtain different kinds of information, such as electronic structure, chemical bonds, crystal structure, elemental composition, conductivity, with only one method.

Electron Escape Depth

One important parameter for PES is the electron escape depth. It determines the distance perpendicular to the sample surface from which photoelectrons still manage to reach the analyzer and be counted.² Electrons travelling through a solid may experience energy losses due to electron-electron (excitation of plasmons, scattering, creation of electron-hole pairs) and electron-phonon interaction (creation / destruction of phonons). The energy loss function is connected with the solid's dielectric function. The described interactions reduce the kinetic energy of a photoelectron in such way, that it reaches the analyzer with lower kinetic energy or even not at all. The longer way the electron has to travel, the higher the probability for an energy loss event. Typically, one defines the electron escape depth, or the Inelastic Mean Free Path (IMFP), as the distance for which an initial electron current I is diminished to $1/e$. Although the IMFP (for a certain kinetic energy) is in principle element specific (due to the dielectric function) comparison of IMFP's of different elements as a function of the electron kinetic energy leads to a *universal* curve (Fig. 2.3) describing the electron escape depth. Deviation from this behavior can be expected for solids with non-metal character (oxides, semiconductors, insulators). The mean free path varies between 3 Å and 50 Å and the minimum of the curve is located around 50 eV. Three typical photo energies are indicated in the figure, corresponding to Ultraviolet PES (UPS, He I, He II) and X-ray PES (XPS, Al $K\alpha$). Even for XPS the mean

¹Also called Electron Spectroscopy for Chemical Analysis (ESCA)

²assuming the sample surface perpendicular to the analyzer's optical path.

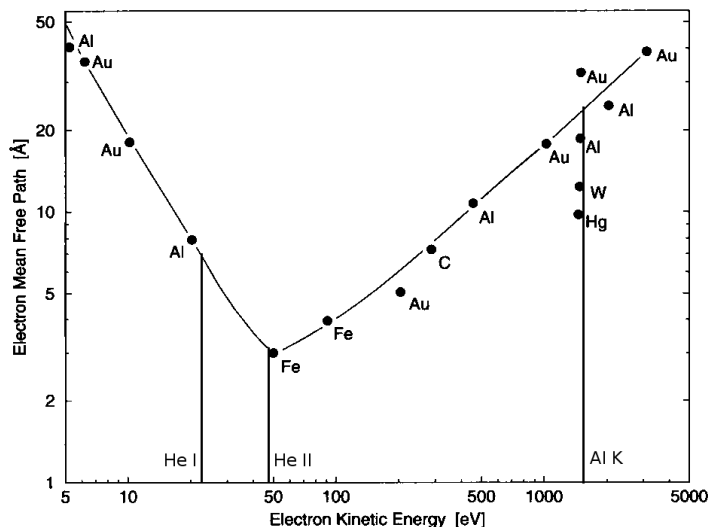


Figure 2.3: Inelastic Mean Free Path of Electrons. Typical photon energies used for PES are indicated.

free path is not larger than 15 Å, underlining the nature of PES to be mainly surface sensitive.³

Three Step Model

In this part an approach to describe the rather complex photoemission process is presented. It is called the *Three Step Model*, in which photoexcitation is broken into three consecutive processes. Many phenomena can be explained by this theory, however, one should keep in mind that this separation is an artificial simplification of the many-body one-step process. According to the three step model photoemission proceeds as follows:

1. Optical excitation of the electron by a photon
2. Transfer of the electron to the surface
3. Escape into vacuum

In the first step interaction with a photon excites the electron from its initial state ϕ_i into a final state ϕ_f . The transition probability ω is expressed by the famous *Golden Rule* (Fermi's Golden Rule)

$$\omega = \frac{2\pi}{\hbar} |\langle \Psi_f | H_{Int} | \Psi_i \rangle|^2 \delta(E_f - E_i - \hbar\omega), \quad (2.3)$$

where H_{Int} is the Hamiltonian for the electron-photon interaction, Ψ_i the initial and Ψ_f the final N-electron states. Allowed transitions have to obey energy and momentum conservation and selection rules for dipole transitions. Implications on photoemission spectra will be discussed later. During the transfer to

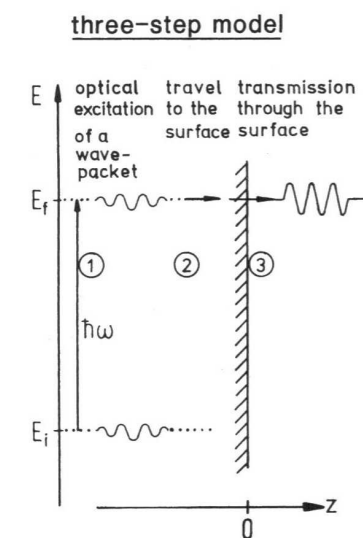


Figure 2.4: Three Step Model.[53]

³However, it should be mentioned that XPS spectra to a great extent represent bulk material character. This is because electronic changes due to a different organization of surface atoms or variations in lattice constants are usually compensated within two or three atomic layers and thus add only a small fraction to XPS spectra.

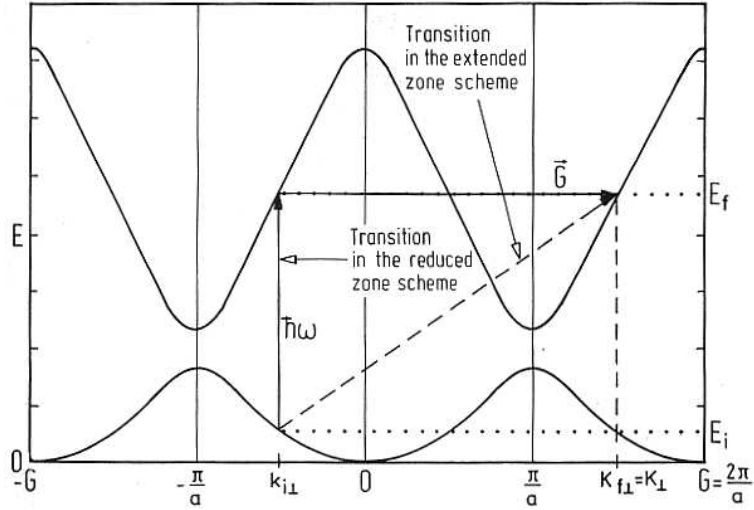


Figure 2.5: Direct dipole transition in extended band scheme

the surface the photoelectron experiences scattering and energy losses mainly due to electron-electron interactions. Here we can refer to what has been said earlier about the inelastic mean free path of electrons in solids. These processes may lead to plasmon peaks and to additional tails on the high binding energy side of core-level peaks. The last step is the transmission of the photoelectron into the vacuum. To be able to leave the solid, the kinetic energy E_{\perp}^{kin} perpendicular to the surface has to be large enough to overcome the surface potential barrier (e.g. the work function). Electrons whose E_{\perp}^{kin} is too small get reflected back inside the solid. This effect shows up, for example, in UPS spectra, where a *cut-off* of signal intensity can be observed above a certain binding energy and can be used to determine the samples work function.

Electron Excitation Issues

As mentioned in the last paragraph electron excitation has to obey conservation and selection rules. At first, photons in the UV range shall be discussed, with kinetic energies typically below 100 eV. The wave vector $k_{h\nu}$ corresponding to this energy range is small compared to a typical Brillouin zone, which justifies to define $k_{h\nu} \approx 0$. In consequence, all transitions in a (reduced) band structure diagram are vertical, thus *direct transitions*, and only additional reciprocal lattice vectors G take part for momentum conservation. This is shown (for an extended band scheme) in Fig. 2.5. Therefore, the photoemission current in UPS is very sensitive to the photon energy and to the electron emission angle, which on the other hand allows to obtain (map) the band structure with Angle Resolved UPS (ARUPS) at a synchrotron radiation facility (possibility to tune photon energy).

The situation changes when going to higher photon energy in the order of kilovolt (XPS). The transitions are not vertical (in the reduced band structure scheme) anymore, as the photon's wave vector now has to be taken into account concerning momentum conservation. Energy conservation is still valid, however, due to the high energy transfer it is always possible to find a suitable final state.⁴ Last, but not least, the acceptance angle for emitted photoelectrons (for XPS) is usually in the order of 10° , allowing to collect electrons with wave vectors (parallel to the surface) covering almost the whole Brillouin zone. All this averages out wave vector

⁴One can imagine that the extended band structure as to be folded several times (to obtain the reduced scheme) to account for the photon energy. Therefore, the unoccupied states density significantly increases for high kinetic energy, forming practically a continuum of possible final states.

sensitivity and selectivity of initial/final state transitions, which leads to the common notion that XPS probes the integrated Density of States (DOS) of a solid.

One-Step Model

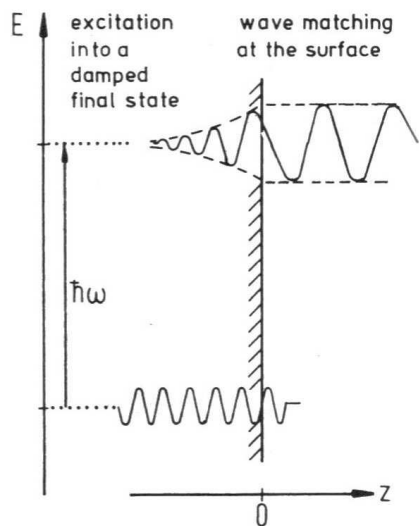


Figure 2.6: One Step Model.[53]

Although the three-step-model can help to understand a lot of photoemission phenomena, it does not account for damping processes and energetic shifts in the quasi-particle spectrum. Within this model, the initial and final states are regarded as Bloch states with infinite lifetime, rendering it impossible to describe photoexcitation into band gap states (exponential decay into the solid) and photoemission from surface states. To improve accuracy one also has to take into considerations changes in the electron self-energy due to many-body effects. The basic equation in the one-step model is the same as in the three-step model, namely the Fermi Golden Rule (2.3) with the proper many-electron wave functions Ψ_N . Fig. 2.6 illustrates the ideal behind the model: Electrons are excited from their initial state into a final state, which propagates freely in the vacuum, but decays from the surface into the bulk. The formalism is very complicated and cannot be presented here, however, a detailed description of the quantum-mechanical calculations can be found in [54].

2.2.2 Photoelectron Spectroscopy Applied to Metal Clusters

Several issues have to be taken into account for the interpretation of spectra when performing photoemission on nanosized objects. Let us first summarize photoemission from bulk material. This situation is depicted in Fig. 2.7a. The impinging photon excites a (core/valence) electron from the bound state into a continuum state above the vacuum level. The photoelectron escapes from the solid and travels towards the analyzer where it is counted. The photohole that is left behind can be regarded as a positive charge. The electronic system responds to this disturbance by realigning its energy levels (relaxation), which influences the photoelectron binding energy (through relaxation energy correction of the Koopman energy⁵), i.e., $E_B = E_{Koopman} - E_{Relaxation}$. In the case of a metallic solid, the conduction electrons also move towards the positive photohole and try to shield the Coulomb field (screening). In the non-conductive case polarization is the main screening mechanism. All these phenomena affect the photoelectron in the vicinity of the hole. Far away (from the surface), however, the electron travels undisturbed (granted that there are no sample charging effects).

For clusters supported on a substrate the situation looks like in Fig. 2.7b. The photoemission process itself proceeds as described before. Relaxation and photohole screening may, however, be changed due to effects caused by the finite particle size, but can be neglected for this discussion. The removal of one electron from a nanosized object leads to a net positive charging of the whole particle. To annihilate this charge, an electron has to be transferred from the underlying substrate to the cluster. However, this is a much slower process compared to relaxation and screening, typically in the order of 10^{-15} s. In a first approximation the particle

⁵In the Koopman theory the electron-electron correlation effects are left out and the binding energy energy is in principle the Hartree-Fock one electron orbital energy.

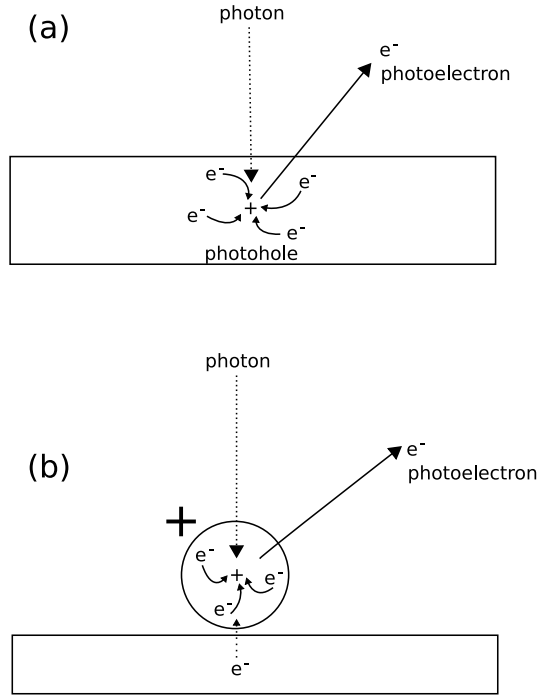


Figure 2.7: Photoemission from bulk material and from clusters: In addition to normal relaxation processes the cluster gets charged and retains its charge until the photohole is neutralized by an electron from the substrate. The charge affects the photoelectron’s kinetic energy due to Coulomb interaction.

can be regarded as a spherical capacitor positively charged by the removal of one electron. The change in electrostatic energy ΔE is given by

$$\Delta E = \frac{\alpha e^2}{4\pi\epsilon_0 R}, \quad (2.4)$$

where R denotes the cluster radius and α a parameter dependent on the actual sample (e.g. $\alpha = 0.41$ for Ag clusters [55]). The photoelectron experiences an attractive Coulomb force towards the charged particle which reduces its velocity, thus, its kinetic energy. Hence, it will appear at higher binding energy in the photoemission spectrum. This is a *final-state effect* of Photoemission Spectroscopy.[56, 57] The time τ necessary to annihilate the positive charge is the governing factor that influences the strength of this effect. Metal clusters on metallic supports represent one extreme where the charge is quickly neutralized and BE shifts in the photoemission spectrum are largely absent. Clusters on an insulating substrate mark the other extrem where is charge is neutralized when the photoelectron is far away from the particle surface, yielding a strongly shifted photoemission spectrum.⁶ We now discuss the intermediate situation where neutralization proceeds in a time scale comparable to the photoelectron traveling a distance of a few cluster radii. One has to account for τ being a *mean* value for the charge lifetime, therefore introducing a probability distribution and consider consequences for photoemission spectra. Such framework is summarized under the so-called *dynamic final-state effect*.[58, 59] The probability $P(t)$ of charge elimination in an interval $[t, t + dt]$ is described by

$$P(t)dt = \frac{1}{\tau} \cdot e^{-\frac{t}{\tau}} dt. \quad (2.5)$$

⁶However, the neutralization is faster than the average time between photon impingements on the same particle to prevent charge build up. Otherwise this would lead to charging phenomena observed for photoemission on highly insulation bulk materials.

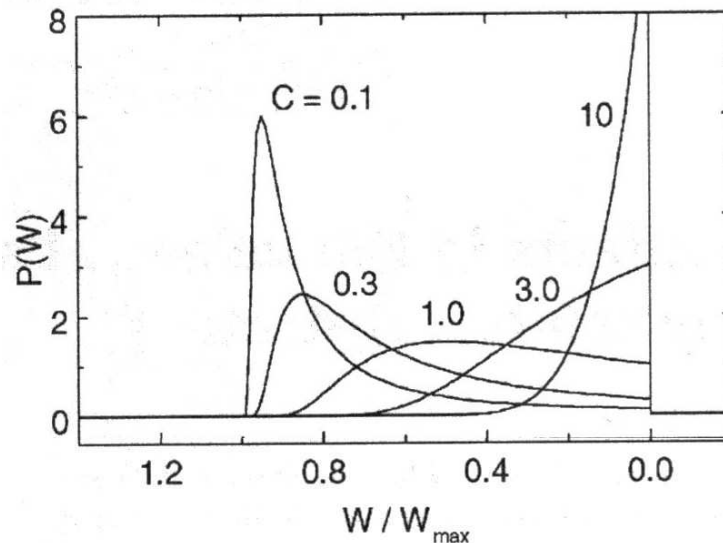


Figure 2.8: Dynamic final state: The curves show the energetic broadening that is incorporated in measured spectra. It is dependent on the coupling C between cluster and substrate. (from [59])

Next, we need an expression for the Coulomb potential acting on the photoelectron as a function of the travelled distance at time t . With the help of Eqn. (2.4) one finds

$$W(r) = \frac{\alpha e^2}{4\pi\epsilon_0} \left(\frac{1}{R} - \frac{1}{r} \right), \quad (2.6)$$

which yields the energy shifts $W(R - vt)$ for a photoelectron with velocity v at the time of charge neutralization t . Due to the probability distribution $P(t)$ this automatically leads to a binding energy shift distribution

$$P(W)dW = P(t(W)) \left(\frac{dt}{dW} \right) dW \quad (2.7)$$

$$\Rightarrow P(W)dW = \frac{CW_{max}}{(W_{max} - W)^2} \cdot e^{\left(-\frac{CW}{W_{max}-W}\right)} dW \quad (2.8)$$

with $W(r) = W(R - vt) \in [0, W_{max}]$, $W_{max} = \Delta E$ from (2.4) and $C = \frac{R}{v\tau}$, the "strength" of cluster-substrate interactions.

Fig. 2.8 shows plots of function 2.8 for different C , ranging from weak ($C=0.1$) to strong ($C=10$) coupling to the substrate. Comparing these two extremes one observes delta-function-like line shapes situated at $W/W_{max} = 0$ ($C=10$) and $W/W_{max} \approx 0.9$ ($C=0.1$), thus correctly reproducing binding energy shifts for clusters on metallic and isolating substrates, respectively. Due to the small line widths, spectral features are only weakly (if at all) broadened. In the intermediate region, however, the curves exhibit a strongly increased width, indicating that under these conditions (with respect to C) the photoemission spectra are not only shifted but their spectral features also significantly broadened. One has to keep on mind that the above discussion dealt with clusters of exactly one size, nevertheless leading (under certain circumstances) to a peak broadening in photoelectron spectra. Extending the model by incorporating a (Gaussian) distribution of particle sizes, the most significant changes occur for C values between 0.1 and 1, where the line widths are considerably increased.

As C contains the photoelectron velocity v , it is interesting to examine the dynamic final-state effect for different photon energies. The photon sources commonly available in an ESCA machine are X-ray tubes and helium-discharge lamps. In [60] this study has been performed for

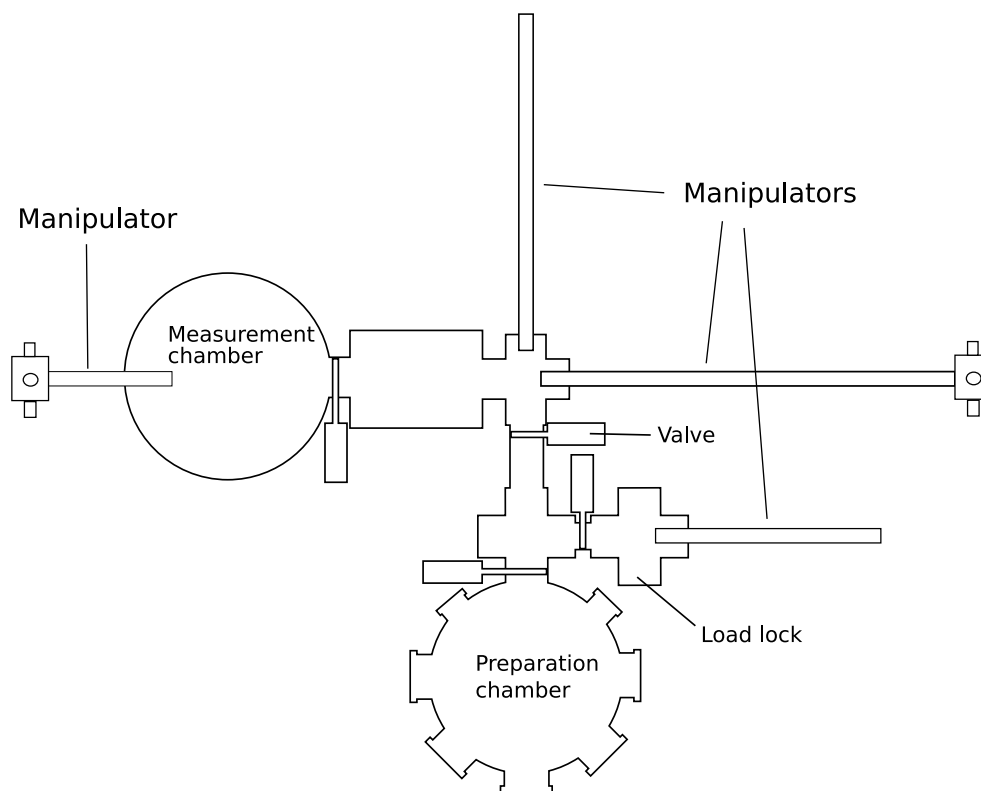


Figure 2.9: Overview of the ESCA machine: The samples are inserted via the load lock and transferred to either preparation or measurement chamber by means of sample manipulators.

1486.6 eV (Al K_{α} , XPS) and 21.2 eV (He I line, UPS) on silver clusters deposited on graphite. The Fermi region was measured with both energies and the spectra compared with references taken on bulk silver. To shortly summarize the results, it could be shown that the dynamic final-state model quite well reproduces the change of the Fermi level shape observed for small clusters with respect to the bulk reference. It turned out that the limited energetic resolution of XPS prevents the observation of subtle line shape changes well distinguished in UPS. However, the positive binding energy shift is well reproduced by the model. The effects induced by the dynamic final-state demands thoroughly considered when interpreting PES spectra, especially the Fermi level region. It is clear that a zero spectral intensity at the usual Fermi edge position (BE=0 eV) does not necessarily imply non-metal behavior of the investigated system. The final-state effect may have shifted the spectrum to positive BE and smeared out the Fermi edge making it difficult to identify.

2.2.3 PES Setup at the ESCA Laboratory

In this section the setup of the ESCA machine used for this work will be presented. The machine (VG EscaLab 210) was purchased from Fisons. Fig. 2.9 shows the top view schematics of the vacuum system. Samples are introduced through the a load-lock chamber and can be transferred via different sample manipulators to either the preparation or the measurement chamber. This mechanism allows sample preparation and analytics to be performed without breaking the vacuum. The preparation chamber is equipped with various flanges to provide a maximum of flexibility for mounting devices and deposition sources.

Fig. 2.10 shows the sample holder facility in the preparation chamber. The sample with the combined sample holder/heater is surrounded by the cooling fingers. This allows to temperatures from -196 °C (liquid nitrogen cooling) up to 900 °C. Just below the sample holder one

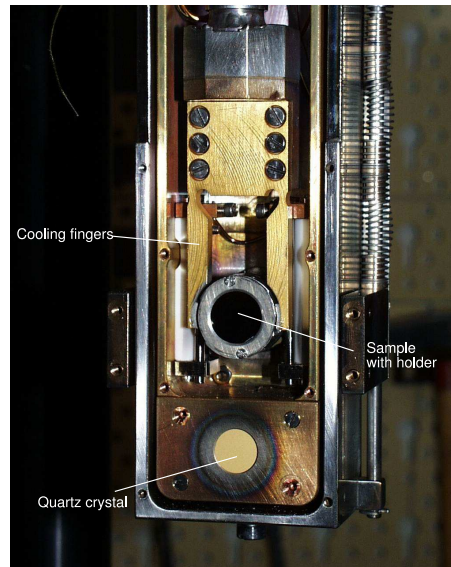


Figure 2.10: Sample holder in preparation chamber (covers removed): The sample sits between two copper clamps that are used for cooling.

can see the quartz crystal, which is used (in connection with a frequency counter) to determine deposition rates. The compact design and the vicinity to the sample allows to monitor rates even during deposition (e.g., with a magnetron, which has a large deposition cone) to avoid large rate deviations. On the other hand, heating of the substrate leads to measured 'deposition rate' as the resonance frequency of the crystal is temperature-dependent. Thermal conduction to the crystal is weak and it takes long time (up to 45 min, depending on the sample's temperature) to reach a thermal equilibrium. Thus, for deposition experiments with heated samples, one has to account for the temperature-induced rate offset.

A detailed schematic view of the measurement chamber is given in Fig. 2.11. The most important part in this arrangement is the hemispherical analyzer (HMA). Combined with electrostatic lenses (located in the tube) it is used for counting electrons as a function of their kinetic energy. An X-ray tube with a monochromator is attached to the chamber, allowing MXPS measurements with $h\nu = 1486.6$ eV (Al K_{α}). Additionally, a He-discharge lamp is mounted for UPS measurements ($h\nu_{HeI} = 21.2$ eV, $h\nu_{HeII} = 40.82$ eV) and a non-monochromated X-ray tube with $h\nu = 1253.6$ eV (Mg K_{α}). An electron and an ion gun ($E_{kin,max} < 5$ keV for both) are available to irradiate the sample with accelerated electrons or ions (e.g., argon ions for cleaning purposes).

The Hemispherical Analyzer (HMA)

The inside of the HMA (see Fig. 2.12) consists of two concentric hemispheres, entry and exit slits, and 5 channeltrons (detection assembly) for electron detection. The transfer lens system creates an image of the measured sample area in front of the analyzer's entry slit (aperture) to allow optimal performance (especially: area of detection independent of electron kinetic energy). High voltages are applied to the hemispheres, allowing only electrons with a chosen kinetic energy (the *pass energy*) to successfully reach the detection device and be counted. The analyzer can be driven in two different modes: constant analyzer energy (CAE) and constant retardation ratio (CRR).

CAE In this mode of operation the pass energy E_p is set to a fixed value (usually between 5 and 50 eV), implicating a constant energy resolution ΔE , as this is a function of the slit width,

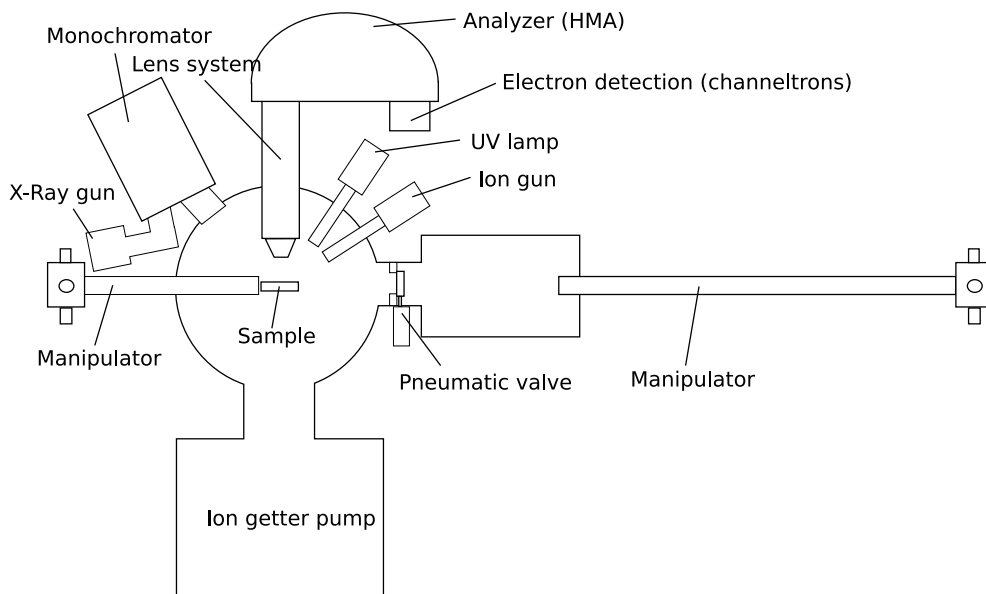


Figure 2.11: ESCA measurement chamber: The device is equipped with a monochromator for MXPS measurements ($h\nu = 1486.6$ eV), a non-monochromated X-ray tube ($h\nu = 1253.6$ eV), a He-discharge lamp ($h\nu_{HeI} = 21.2$ eV), an electron and an ion gun ($E_{kin,max} < 5$ keV for both).

the HMA radius, and E_p . Electrons are retarded to E_p and the retardation voltage is ramped during one scan according to the momentary electron kinetic energy. The overall (analyzer and transfer lenses) transmission function $T(E_{kin})$ follows the dependence

$$T(E_{kin}) \propto \frac{1}{\sqrt{E_{kin}}}.$$

This mode is used for XPS measurements, as a constant resolution over the whole kinetic energy range (typically 1486.6 eV to 400 eV) is crucial for reliable evaluation of the spectra.

CRR Photoelectrons are retarded by a constant factor $K = \frac{E_{kin}}{E_p^*}$. As K is constant and E_{kin} is varied throughout a scan, the pass energy E_p^* cannot be constant anymore, but increases with E_{kin} . Therefore, the resolution ΔE is not constant⁷ and the transmission function simply

$$T(E_{kin}) \propto E_{kin}.$$

This mode is suitable for UPS and AES (Auger Electron Spectroscopy), however, sometimes it can be more favorable to use CAE for UPS.

The whole vessel is shielded against magnetic fields by μ -metal housing. Additional trimming coils around the transfer lens and inside the HMA (not shown) allow fine-tuning of magnetic compensation fields. This is especially recommended for UPS with its low electron kinetic energies (5 - 20 eV E_{kin} for He I). Bad compensation leads to a much earlier intensity cut-off in VB spectra.

Fig. 2.13 shows the relative positions of the energetic levels in the sample and the photoelectron analyzer. The scheme is plotted for a metallic sample, as this facilitates the following discussion. The left side of the drawing corresponds to the situation near the sample, whereas the right side describes the level positions in the analyzer. Normally, the sample is in good contact with the sample holder, which is grounded through the vacuum chamber. Consequently,

⁷However, $\frac{\Delta E}{E_{kin}}$ is constant

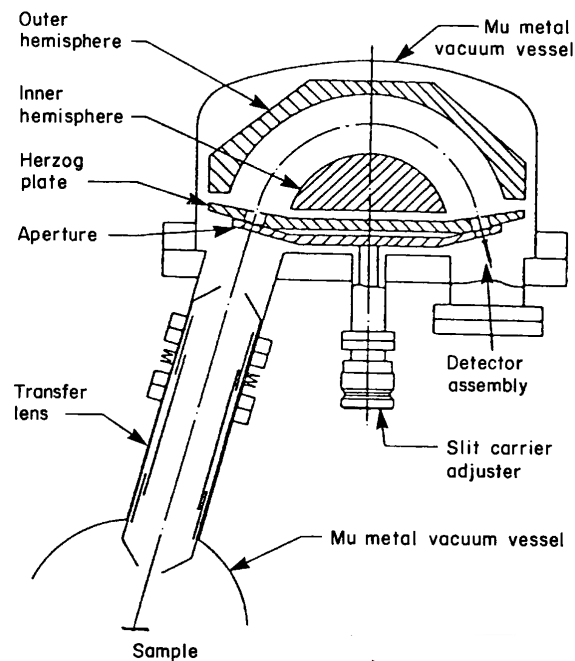


Figure 2.12: Hemispherical Mirror Analyzer: The transfer lens system casts an image of the detection area on the sample in front of the analyzer aperture.

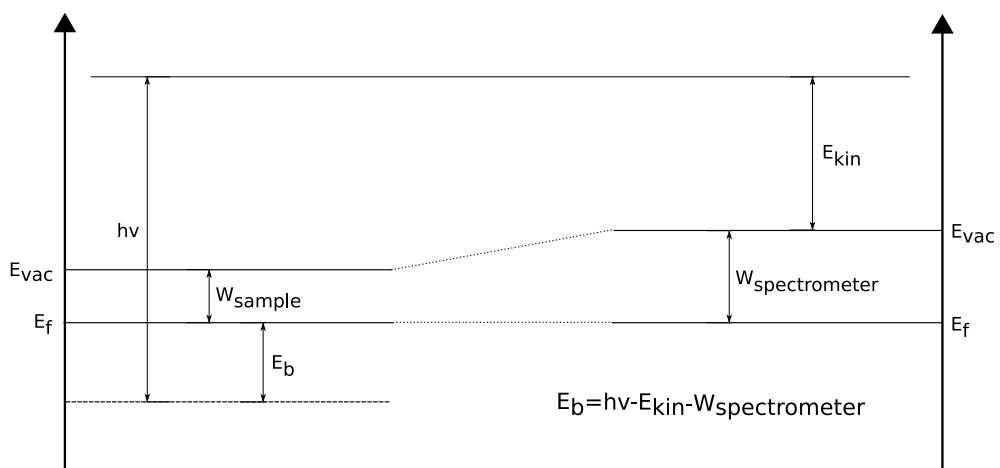


Figure 2.13: Relation between energy levels of the sample and the spectrometer. As the sample is in contact with the rest of the machine, the Fermi levels have to be aligned. Binding energies are referenced to E_f and the influence of W_{sample} eliminated.

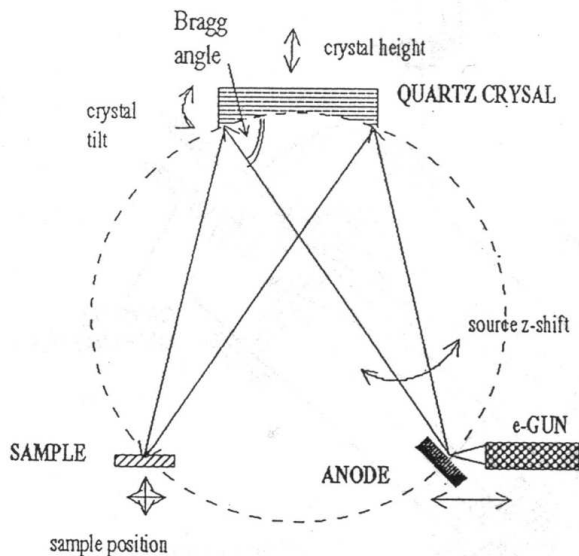


Figure 2.14: Rowland circle: The anode X-ray spot and the sample surface have to be on the Rowland circle to assure proper monochromatization (correct Bragg angle) and focus.

the Fermi level (E_f) of the sample must be aligned with E_f of the likewise grounded analyzer. As there is usually a work function difference $W_{spectrometer} - W_{sample}$, a corresponding potential difference for E_{vac} appears. The natural measurable quantity is the kinetic energy of the photoelectrons E_{kin} . If a photoelectron has been excited from a bound state (dotted line), the binding energy E_b (with respect to E_f) can be obtained with the knowledge of the excitation energy ($h\nu$), the spectrometer's work function ($W_{spectrometer}$) and E_{kin} through

$$E_b = h\nu - E_{kin} - W_{spectrometer}.$$

One should note, that the sample's work function does not go into the calculation, implying that the measured binding energies are independent this quantity. This is indeed true and one of the good things of photoelectron spectroscopy.

The Monochromatised X-ray Source

Monochromatisation of X-ray radiation dramatically decreases the line width in the energetic spectrum by allowing only a small (\approx monochromatic) fraction of the total light to reach the sample. This strongly enhances the resolution of photoelectron spectra and eliminates satellite peaks stemming from the substructure of the participating shells.⁸ Monochromatisation is achieved by performing Bragg diffraction at a crystal surface, obeying to *Bragg's Law*:

$$n\lambda = 2d \sin \Theta, \quad (2.9)$$

where Θ is the Bragg angle, d the spacing of the crystal planes, n the order of reflection and λ the X-ray wavelength. Fig. 2.14 illustrates the geometric relations between sample, crystal and anode. To reach high X-ray intensities a small spot on the anode has to be well focused on the sample. The bent crystal surface touches the circumference of a large circle, called *Rowland circle*, on which sample and anode have to be positioned to satisfy the Bragg Law. The radius of the Rowland circle is half the curvature radius of the crystal. A micro-focus e-gun is used to produce a very small spot on the anode. The actual setup realized in the ESCALab 210

⁸The typically used K_α line origins from $L(s_{1/2}, p_{1/2}, p_{3/2})$ to $K(s_{1/2})$ shell electron transitions.

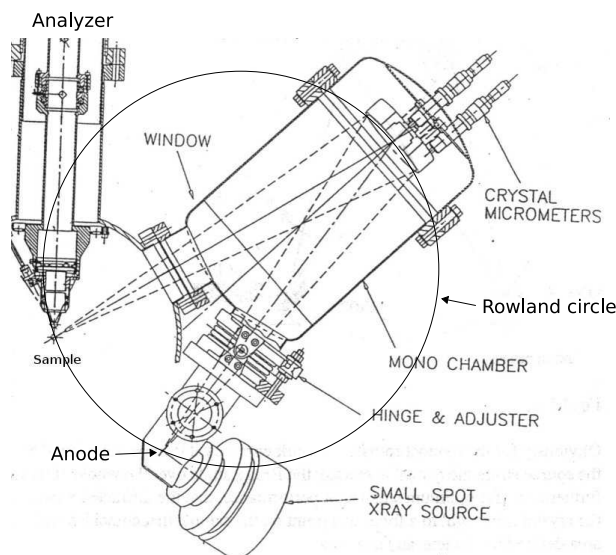


Figure 2.15: Monochromator schematics of ESCALab 210: The drawing shows the lightpath in the monochromator. The machine is equipped with two monochromatizing crystals which can be adjusted by micrometer screws.

machine is shown in Fig. 2.15. The monochromator consists of two crystals in order to increase photon intensity. The variety of adjustable parameters (sample position, anode position and tilt, crystal height and dispersive/non-dispersive tilt) makes alignment of the whole system a time consuming and tedious task, as not only the Bragg Law has to be obeyed, but also the resulting X-ray spot on the sample has to be positioned exactly under the analyzer for optimum performance.

2.2.4 Experimental Parameters Used in This Work

MXPS spectra were acquired using monochromatized Al K_{α} X-ray radiation ($h\nu = 1486.6$ eV).⁹ The analyzer was set to Constant Analyzer Energy (CAE) with a Pass Energy of 20 eV. This value was chosen as a compromise between good resolution (for determination of Fermi edge) and count rate. The typical energy resolution was 0.5 eV. For UPS spectra the He I emission line ($h\nu = 21.2$ eV) was used to excite the photoelectrons. The analyzer was operated in Constant Retardation Ratio (CRR) with CRR=4. The base pressure in the measurement chamber was always in the order of 8×10^{-10} mbar.

It should be pointed out that the experiments presented in section 3.1.1 were performed using a different machine (Leybold EA 11) than discussed above. However, the general principles described earlier also hold true for this case. The experimental parameters can be found in the corresponding subsection of 3.1.1.

⁹Non-monochromatized radiation (Mg K_{α} , $h\nu = 1253.6$ eV) was used for the study on chemically synthesized gold particles presented in 3.1.1.

Chapter 3

Results

3.1 Thiol-Passivated Nanoparticles

3.1.1 X-ray Radiation Damage of Thiol-Passivated Gold Particles

This work has been published in 'M. Büttner, T. Belsler, and P. Oelhafen, *Stability of Thiol-Passivated Gold Particles at Elevated Temperatures Studied by X-ray Photoelectron Spectroscopy*, J. Phys. Chem. B 109 (2005) 5464-5467'.

Introduction

Thiol-passivated nanoparticles (Fig. 3.1) and their ability to self-assemble are widely used in nanoscience. Although there are techniques to remove the organic shell from the particles and to obtain naked clusters (see A.3.1), for various reasons it may be preferable to study particles still protected by the organic molecules. If one is primarily interested in the physical properties of the metal core, it is of great importance to have knowledge about the influence of the surrounding molecules. Their high ratio of surface atoms makes small clusters increasingly sensitive to the environment. For future applications the protecting shell has to be reasonably stable in order to reliably prevent particle aggregation.

The aim of this study was to investigate the thermal stability of thiol-passivated gold nanoparticles with different thiol-chain lengths. For the first time, a complete range of thiol lengths starting from 3 (C3) up to 8 (C8), and 16 (C16) carbon atoms has been investigated. Theoretical works based on calculations using density-functional-theory (DFT) mainly focus on

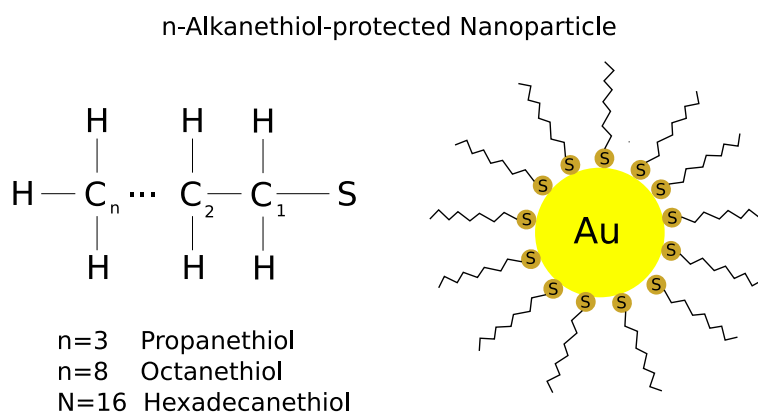


Figure 3.1: Alkanethiol-passivated Gold Particle: *Left:* Chemical structure of n-alkanethiols. *Right:* Sketch of passivated gold particle. Thiol molecules attach to the gold surface via their sulfur headgroup.

short-chain thiols (typically 3-4 carbon atoms) due to the large amount of calculation time necessary when treating longer chains. On the contrary, experimental results are obtained mostly from thiol chain-lengths of 8 and more carbon atoms. Colloids with mean particle diameters ranging from 1.6 nm to 4.9 nm have been synthesized and thiol-passivated by a wet chemical route. The sulfur-to-gold ratio as a function of the temperature was monitored by X-ray Photoelectron Spectroscopy. TEM micrographs illustrate the particle self-assembly on a carbon coated TEM grid.

The results presented here show that X-ray radiation may cause damage to the passivating shell and that the nature of this damage depends on the thiol molecule length. The inter-chain interaction affects the threshold temperature for thiol desorption and influences particle self-assembly.

Experimental Details

The particles have been synthesized following a modified chemical route described by Murray et al.[27], see A.3. The powder consisting of thiol-passivated gold clusters was dissolved in toluene with a concentration of less than 0.5 mg/mL. For each synthesized colloid, TEM imaging was carried out in order to measure the particle size. For the TEM sample preparation, the gold colloid solution was drop-deposited onto a carbon coated copper grid and then transferred into the TEM after the solvent was completely evaporated. Micrographs were taken in a FEI/Philips Morgagni 268D TEM with a Digicam Megaview II camera. As the particles were not size-selected, a size dispersion of about $\pm 20\%$ was unavoidable in each sample due to the synthesis method. Clusters of different mean diameters with thiol chain lengths from 3 to 8, and 16 carbon atoms, respectively, were used for the experiments. We included two samples with the same thiol (C8) shell, but different mean diameter (1.6 nm and 3.1 nm), in order to study the influence of particle size on the experimental results.

XPS core level measurements took place in UHV conditions. Mg K_{α} non-monochromatized X-Rays with a main photon energy of 1253.6 eV were used as light source for this series of measurements, and the excited photoelectrons were analyzed at a pass energy of 30 eV. The typical energy resolution (FWHM) of this setup was about 0.9 eV.

Typically 5-10 μL of colloidal solution was drop deposited on a HOPG sample and transferred into the measurement chamber. For sample heating the desired temperature maintained for 5 min. After cooling down, the sample was measured at room temperature. The Au 4f and S 2p core level lines were decomposed with a Doniach-Sunjic line shape using the Levenberg-Marquardt fitting algorithm. From these decompositions the sulfur-to-gold ratio was calculated.

Results and Discussion

The evaluation of the sulfur core-level line (S 2p) revealed a distinct difference in spectra features related to the length of the passivating thiol chain. Fig. 3.2 shows two typical examples of S 2p spectra, which are representative for the whole ensemble of samples. While in the case of C3, the spectrum consists of a single spin doublet (Doublet A) with a S $2p_{3/2}$ binding energy of 162.4 eV (associated to sulfur-gold bonding[61]), in the case of C16 the spectrum is composed of two doublets (A and B), with a S $2p_{3/2}$ binding energy of 163.5 eV for doublet B. The relative intensities between doublet A and doublet B were not fixed, but evolved during the experiments in favor of doublet B. Based on the existence or nonexistence of doublet B in the corresponding decomposed S 2p spectrum, the samples were into two groups: short thiols with no doublet B (C3, C4, and C5) and long thiols with doublet B (C6-C8, and C16). According to the literature, doublet B can be attributed to a sulfur species that appears with increasing X-ray radiation

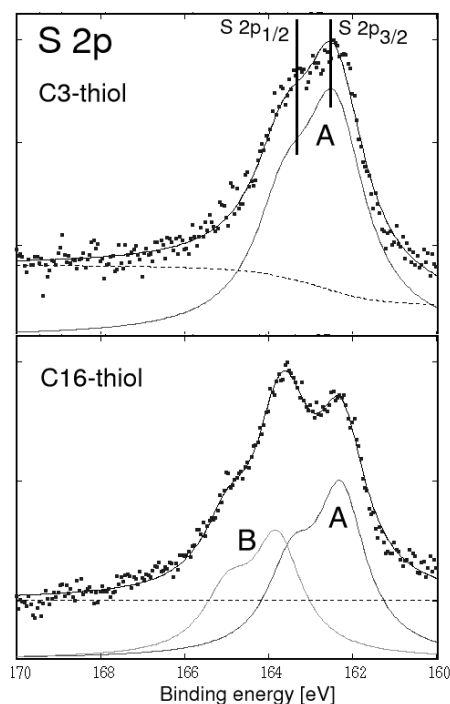


Figure 3.2: Typical decompositions of the S 2p core-level spectrum for short thiols (represented by C3) and long thiol (C16). Doublet A is associated with a S-Au bond, while doublet B indicates a X-ray radiation-induced sulfur species, i.e., progressive thiol shell damage. In contrast to long thiols (C6-C8, and C16), short thiols (C3, C4, and C5) showed no radiation-induced doublet B.

time, indicative of damage to the thiol shell,[62, 63] although there is still discussion about the nature of this species, e.g. disulfide or dialkyl sulfide. In order to verify this, selected samples (C3, C4, C8, C16) were irradiated at room temperature with X-ray radiation for 17 hours and XPS measurements were taken every 4 hours to monitor changes in the S 2p spectra. The relative intensity of doublet B to doublet A increased gradually as a function of radiation time: From 0.1 to 0.8 for C8, and from 0.2 to 1.2 for C16. Samples C3 and C4 did not evolve a doublet B. The shell damage induced by the X-ray radiation will be accounted for in the discussion of the following experimental results. As S-C bond scission is unlikely to occur due to its high binding energy, it is reasonable to use sulfur as a monitor for the degradation of the thiol shell.

To monitor the decomposition of the shell the sulfur-to-gold (S/Au) ratio was calculated from XPS data. Fig. 3.3 shows S/Au ratio as a function of the annealing temperature. As previously mentioned, the curves are displayed in separate graphs, based on the existence of doublet B. The upper part (a) consists of samples with short thiols of 5 or fewer carbon atoms. The prominent feature is a strong decrease of the S/Au ratio in a region between 90 °C and 140 °C. This behavior marks the beginning of a temperature-induced desorption of sulfur. The lower part (b) shows samples with long thiols of 6 or more carbon atoms. Unlike the case of shorter thiol chains, the samples show much smaller variations in the S/Au ratio up to 160 °C, except for sample C7. Going to higher temperatures, a strong decrease can be observed, which is associated with sulfur desorption. This was also confirmed by additional thermogravimetric and differential calorimetry measurements performed on a octanethiol (C8) sample (not shown). These measurements were performed by Thomas Belser (Group of Prof. Pfaltz, Institute of Organic Chemistry, Basel). It is worth mentioning that both C8 samples show a similar behavior.

As doublet A is characteristic for gold-bound sulfur its S/Au ratio was separately calculated

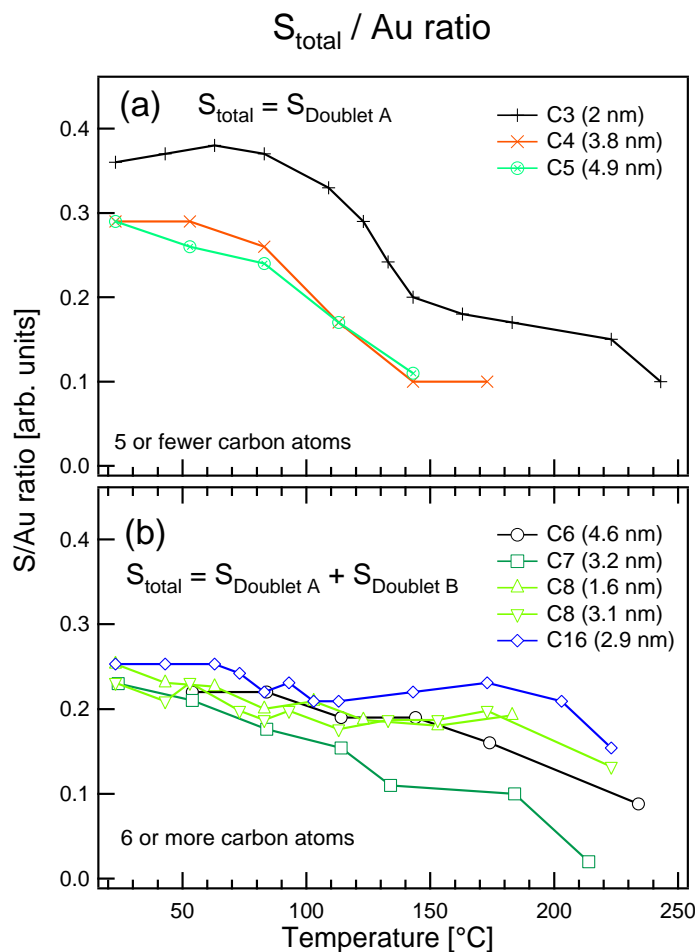


Figure 3.3: The S/Au ratio as determined by XPS as a function of the temperature. Passivating shells with short thiols (a) show desorption between 90-140 °C, shells with longer thiols (b) desorb above 160 °C.

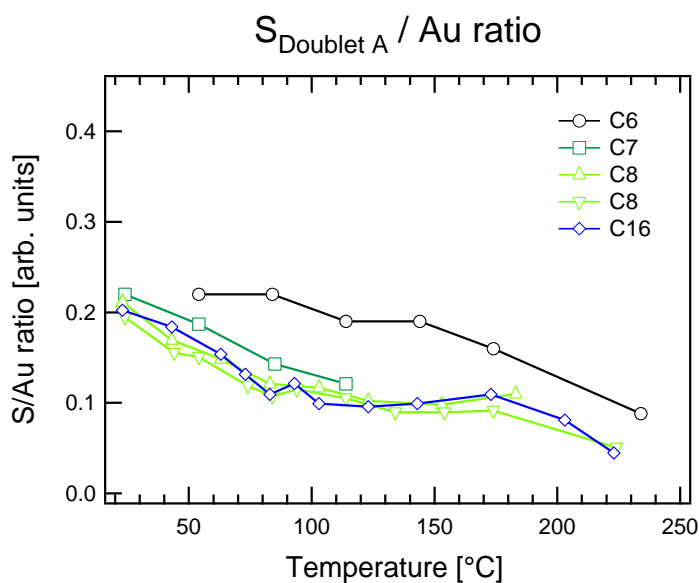


Figure 3.4: The S/Au ratio for doublet A (S-Au bond) indicates progressive thiol shell damage between room temperature and 160 °C. It is caused by continuous X-ray radiation and is not temperature-related. Short thiols are omitted, as they did not exhibit radiation-induced doublet B.

from the S 2p spectra to give a qualitative estimation of thiol chains that are still attached to the gold core. Fig. 3.4 illustrates the development of the S/Au ratio for doublet A. Data points for C3, C4 and C5 are omitted, as they are identical to Fig. 3.3(a). Due to low signal-to-noise ratio of the S 2p spectrum, a decomposition of the two doublets cannot be given above 120 °C. A progressive decrease of the S/Au ratio with increasing temperature can be observed. Taking into account the previously addressed effect of X-ray radiation on the S 2p spectra (shell damage), this decrease can be interpreted as S-Au bond breaking induced by X-ray radiation. As was demonstrated in Fig. 3.3(b) for most of the samples the S/Au ratio (S_{total}) varied little up to 150 °C. This means that despite the thiol shell damage, most of the molecules remain on the sample in this temperature range. Again, data for the two C8 samples correlates well.

In conclusion, the data show that short-thiol shells show no degradation with X-ray radiation, but desorb between 90 °C and 140 °C. On the other hand, long-thiol shells are stable up to temperatures of 160 °C, but show S-Au bond breaking due to X-ray radiation damage. The mean particle diameter of the examined samples did not significantly affect the results, as was confirmed by the two C8 samples. According to theoretical calculations, the S-Au binding strength should not be affected by variation of the thiol chains length (for $C > 2$).^[64] However, our results show different reaction (in terms of radiation-induced damage) to X-ray radiation for short and long thiol chains.

The changes in desorption temperature reflect the stabilizing forces between the thiol molecules, which increase with longer chain lengths.^[65, 66] Additionally, it has been reported that thiols of less than 5 carbon atoms produce colloids that tend to degrade over several weeks, whereas colloids with longer chains can be kept under ambient conditions for months without showing any sign of degradation.^[29]

There may be a possibility that some detached thiol molecules do not desorb from the sample, but remain directly stuck on the HOPG surface. Such process then had to be taken into account for the preceding interpretation. This was checked experimentally with a pristine HOPG sample in a vacuum chamber exposed to thiol vapor. For this experiment an air-cleaved HOPG substrate was exposed to a hexadecanethiol (C16) atmosphere of 1×10^{-6} mbar for one hour. The thiol was introduced in the chamber through a leak valve. Afterwards, the substrate was checked with XPS, and no traces of sulfur could be detected, which limits the possibility that a considerable fraction of thiol chains may have attached to the HOPG surface after S-Au bond breaking. Therefore, it can be assumed that the thiol shell is still located around the gold core even under increasing X-ray radiation damage.

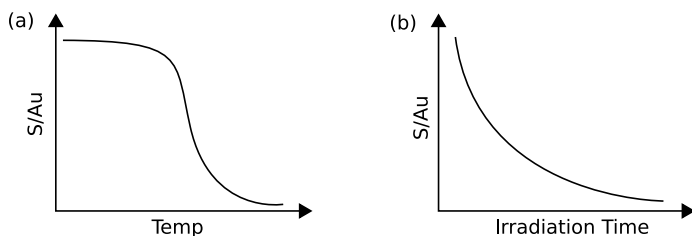


Figure 3.5: Two mechanisms leading to S/Au decrease: (a) Temperature-induced desorption of thiol molecules. (b) X-ray-radiation-induced Au-S bond breaking.

The two different mechanisms that were observed in this study are schematically shown in Fig. 3.5. If temperature-induced desorption is the dominating process, the S/Au (S_{total}) ratio decrease resembles Fig. 3.5a, the desorption temperature threshold indicated by a sudden drop. X-ray radiation-induced thiol shell damage is a irradiation time dependent process and affects the S/Au ($S_{DoubletA}$) ratio as depicted in Fig. 3.5b. During the latter process the S_{total}/Au ratio changes much slower.

To check if changes in the organic shell also affect the gold-core, the binding energy of the Au 4f_{7/2} has been evaluated as a function of the temperature. Some results are shown in Fig. 3.6 together with the corresponding S/Au ratios for doublet A (indicative of S-Au bond). In

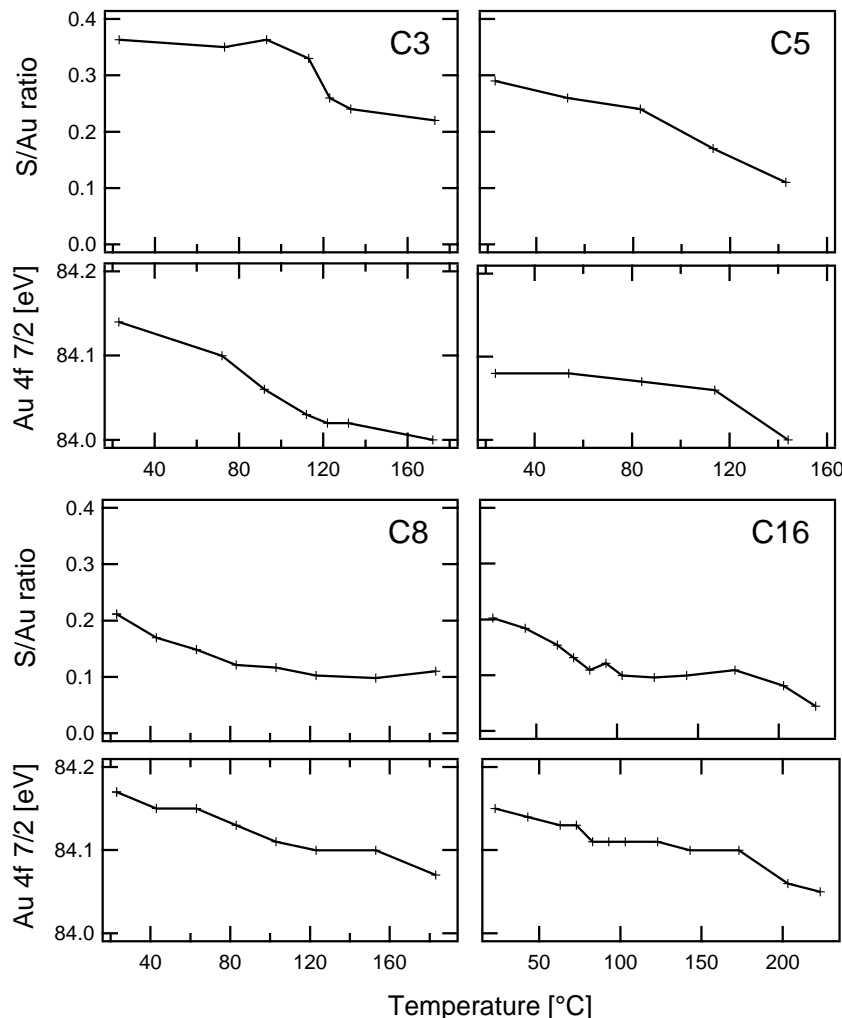


Figure 3.6: Comparison of the $S_{DoubletA}/Au$ ratio and the Au 4f binding energy as a function of the temperature. The S/Au ratio is a measure for gold-bound thiol and shows fairly good correlation with changes in Au 4f binding energy.

all cases the Au 4f binding energy for the as-prepared samples is higher than for a bulk gold reference (84.0 eV). There is a fairly good correlation between S/Au ratio and corresponding Au 4f binding energy for all of the four samples investigated. On the one hand, the photoemission final-state effect might increase the apparent core-level BE (see 2.2.2). This effect diminishes with increasing particle size, thus particle growth leads to a negative BE shift. Damage of the protecting organic shell by either temperature-induced desorption or x-ray induced Au-S bond breaking may allow particle aggregation. On the other hand, initial-state changes could also be responsible for core-level peak shifts. It was reported recently that the binding of chlorine atoms to Au₅₅ clusters induces a metal-insulator transition by 'removing' valence band electrons from the gold cluster valence electron pool. It is therefore recommended also to consider possible thiol/sulfur-induced effects. Although the sulfur's electronegativity is lower than for chlorine, theoretical and experimental studies found the Au-S bond to be quite strong and to have impact on the cluster's geometric configuration.[67] Investigations with XANES (X-ray Absorption Near Edge Structure) revealed a higher intensity of the so-called *white-line* (electronic dipole transition 2p → 5d) of thiol passivated gold nanoparticles with respect to bulk gold, suggesting an increased number of 5d-holes due to Au-S interaction.

The S/Au ratio (S_{total}) as a function of the thiol length is shown in Fig. 3.7. The data points

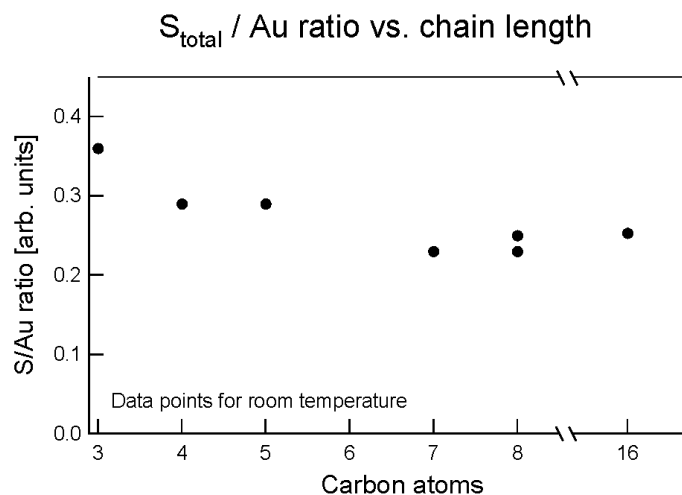


Figure 3.7: The S/Au ratio as a function of the thiol length. The increase for short chains may indicate a higher thiol density on the gold surface.

were taken from Fig. 3.3 at room temperature. An increased S/Au ratio can be observed for the shortest thiol chains. A possible explanation for this would be that the thiol chain density on the gold cluster surface is dependent on the chain length, e.g., through different spacial orientation. This means a higher thiol density with shorter thiol length. An effect of the particle size can be neglected, as the data for the two C8 samples match well. This result stands in contrast to earlier studies of thiol monolayers on flat gold substrates, where an increase of thiol packing density with increasing chain length was observed.[68] Influence of the different thiol-chain lengths (namely variation of the S/Au ratio because of different sampling depths for the photoelectrons) can be ruled out as this would lead to an increased S/Au ratio with longer thiols. This discrepancy cannot be cleared within the scope of this work and needs more investigation.

TEM micrographs were taken to illustrate the particle self-assembly. Fig. 3.8 shows micrographs for samples with the shortest (C3) and longest (C16) thiol chain. While the C3-thiol-passivated particles are randomly scattered, the C16-thiol-passivated particles form dense 2-dimensional islands. The main driving factor for the self-assembling mechanism has its origin in the interaction force between the hydrocarbon chains.[69] They play the prominent role in the crystallization process and can outweigh the van-der-Waals forces between the metal nanocores by two orders of magnitude.[32] One could speculate as follows (see also corresponding sketches in Fig. 3.8): the propanethiol molecule shell only interacts weakly with the shells of other nanoparticles, thus exhibiting only small tendency to crystallize into denser islands. The hexadecanethiol shells on the other hand give rise to a much stronger interaction force between the passivating shells, which leads to a strong crystallization force. As the colloids had to be drop-cast on a carbon-coated grid for TEM imaging and not on an HOPG substrate as before, further examination will be necessary to study the particle organization on HOPG.

Conclusion

We have studied the influence of the chain length upon the thermal stability of the passivating thiol shell of gold nanoparticles deposited on HOPG. The ratio of sulfur to gold obtained by XPS measurements was used to monitor the degradation of the thiol shell as a function of temperature. Our results showed that short thiols (C3, C4, and C5) begin to desorb from the sample between 90-140 °C, whereas for long thiols (C6-C8, and C16) this threshold is around

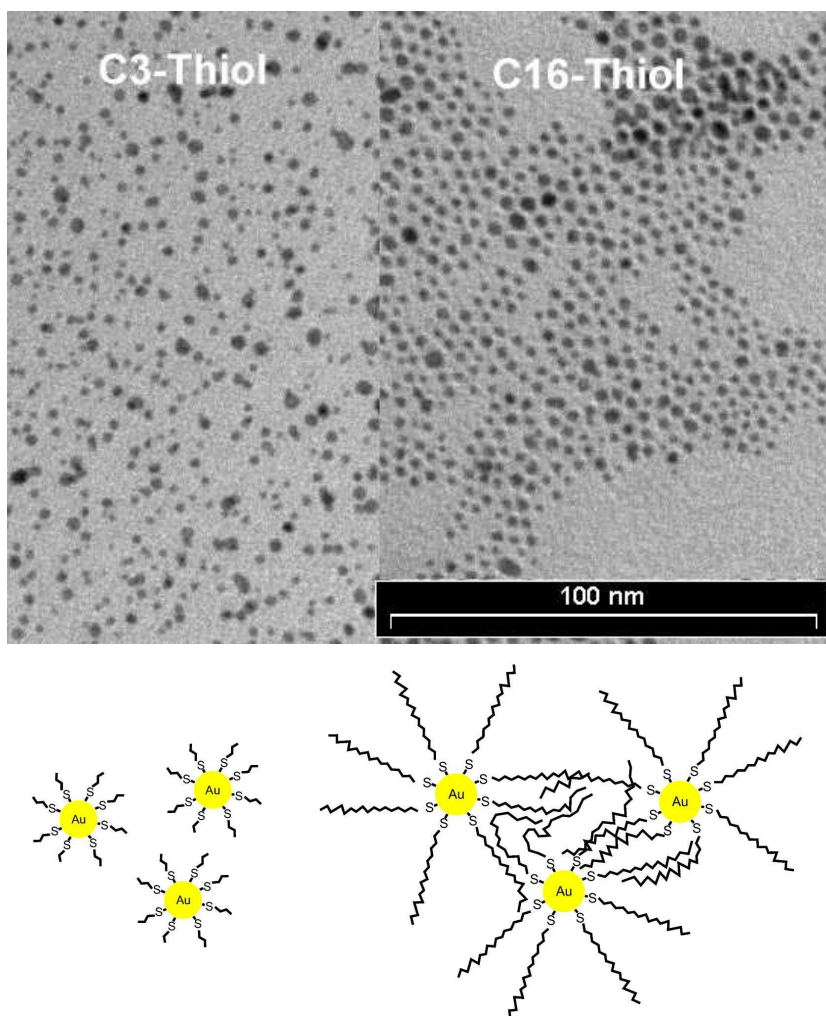


Figure 3.8: The two TEM images show the influence of the thiol shell upon the self-assembling properties. Left: propanethiol (C3), right: hexadecanethiol (C16). Interaction between particles is enhanced for C16 due to the longer thiol chain length, as illustrated underneath.

160 °C. The effect of progressive thiol shell damage (S-Au bond breaking) through continuous X-ray radiation was observed with long thiol molecules, but was absent with short thiols. Examination of the decomposed S 2p spectra led to the conclusion that the thiol molecules stay located around the gold core even under X-ray radiation damage. Comparing the S/Au ratio in terms of thiol chain length, an increased value for short thiols may indicate an higher thiol density on the gold core. The self-assembly of the colloids is affected by the thiol length, as shown with TEM images of C3 and C16 colloids. The particles are randomly scattered with a high inter-particle distance for C3. In contrast to this, the C16 colloid arranges in 2-dimensional islands. BE shifts in Au 4f core-level lines showed to be correlated with thiol shell decomposition.

3.2 Thiol-gold Interactions

3.2.1 Noble Metal Cluster Nucleation on Carbon Substrates

Based on experiments performed with chemically synthesized gold particles we decided to study the thiol-gold interaction in more detail under UHV conditions. Therefore, the preparation of nm-sized particles by metal evaporation was studied first. This work is currently submitted to Surface Science as 'M. Büttner and P. Oelhafen, *XPS study on the Evaporation of Gold Submonolayers on Carbon Surfaces*'.

Introduction

The BE shifts discussed in the last section gave motivation to study thiol-cluster interactions in more detail. Particularly, the nature of the sulfur-gold bond is still object to many experimental and theoretical investigations. In order to perform experiments exclusively under UHV conditions, clusters had to be grown *within* the vacuum system. Carbon substrates were chosen as particle support as cluster-substrate interaction is commonly believed to be weak on such surfaces and thereby allows to study mainly the properties of the particle itself. If thiol adsorption indeed affected the cluster's electronic structure, it would be more pronounced for smaller particles (higher fraction of surface atoms).

The nucleation and growth of metal particles on amorphous carbon is mainly governed by the density of surface defects, at which atoms are trapped. The atomic mobility is low on such substrates due to a highly disordered surface.[70, 71] A high defect density results in a high nucleation density with small diameter particles. In contrast, on highly oriented pyrolytic graphite (HOPG), the nucleation density is significantly smaller with much larger particle diameters. Hence, the particle size is influenced by the defect density, which on amorphous carbon films cannot be controlled easily. To study the nucleation on surfaces with different defect densities, pristine HOPG, amorphous carbon, and argon-ion-irradiated HOPG are used as substrates. The application of argon ion beams to create defects on pristine HOPG allows to control the defect density by variation of the irradiation time.[72, 73] The nucleation and growth of gold nanoparticles at room temperature was investigated as a function of the metal coverage and these results have been compared with data obtained from silver on identically prepared samples. Furthermore, cluster growth was examined as a function of the temperature by deposition on heated substrates.

Experimental Details

The preparation of the amorphous carbon and pristine HOPG samples was performed as described in 2.1.1. These two kinds of substrates represent surfaces with high and low defect density, respectively. A third type has been prepared, which is referred to as the *irradiated HOPG* sample: A HOPG substrate was irradiated for 1 minute with Ar⁺-ions (3 keV kinetic energy, incidence angle $\approx 45^\circ$) to create defects. The focused ion beam was scanned (X-Y directions) over the surface to yield a homogeneous irradiation. The averaged ion flux over the scanned area was $\sim 3 \times 10^{13}$ ions/(cm² s).

The deposition rate measured with the quartz crystal was fixed to 0.01 Å/s and drifts were reduced to a minimum (< 3%) to minimize influence on cluster nucleation. The quantity of evaporated metal is given in equivalent thickness of a uniform layer, as calculated from the quartz crystal measurement. It is very important for the discussion of the results to distinguish between the amount of evaporated material (equivalent thickness) and the actual coverage on the sample determined by MXPS quantification, as the sticking coefficient for metal on carbon

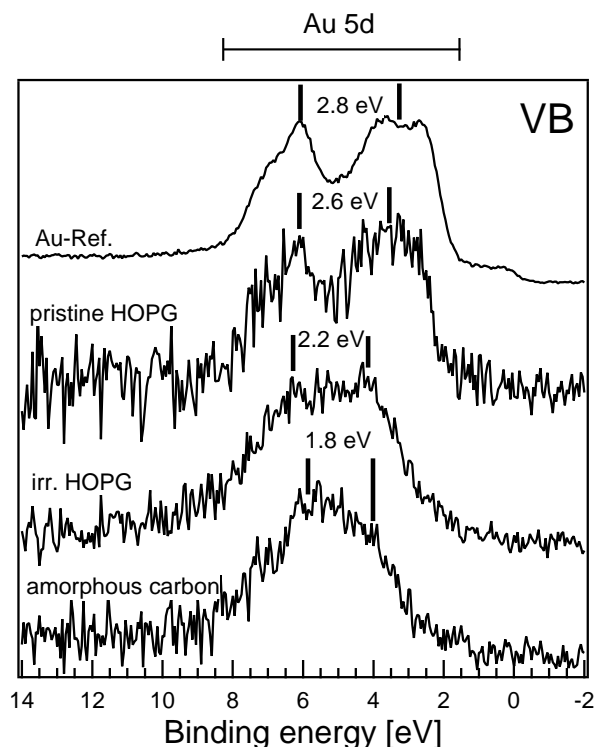


Figure 3.9: MXPS valence band spectra and Au 5d spin-orbit splitting for 0.1 Å Au on different carbon substrates. For the Au reference (clean Au foil), the mark at 3.25 eV has been placed in the middle of the broad peak. The contribution of the carbon substrate (featureless background) has been subtracted from the spectra.

substrates is usually smaller than for metal deposited on metal as in the case of the quartz microbalance.

In order to investigate the early stages of nanoparticle nucleation and growth gold was evaporated in consecutive steps, with intermediate transfers to perform MXPS measurements. The substrates were kept at room temperature. For comparison of the results the same series of experiments was performed with silver.

To study the influence of the temperature a fixed amount of gold (0.1 Å) was evaporated on different heated substrates (200 °C, 400 °C, 600 °C). Before they were transferred to the measurement chamber, heating was switched off to allow cooling to room temperature.

Both core-level and VB spectra were obtained using MXPS. The low photoionisation cross section for carbon compared to gold reduced substrate contributions in the VB region ($\frac{\sigma_{Au5d}}{\sigma_{C2p}} = 2600$ for Al K_{α}). Only then it was possible to observe considerable gold contributions in the spectra. UPS was inappropriate as the low gold concentration on the sample would not have been visible in the VB spectrum dominated by a large carbon signal.

Results and Discussion

Deposition at Room Temperature

The spin-orbit splitting energy ΔE of Au 5d electrons is affected by the mean coordination number the cluster atoms.[56] With decreasing coordination number the valence band narrows because of a reduction of the atomic orbital overlap. Since the mean coordination number is a function of the particle diameter, ΔE can be used to estimate the particle size. Fig. 3.9 shows MXPS VB spectra for 0.1 Å gold. The main contribution (2-8 eV) stems from Au 5d valence band electrons. As indicated in the graphs, the spectra show splitting energies from 2.6 eV

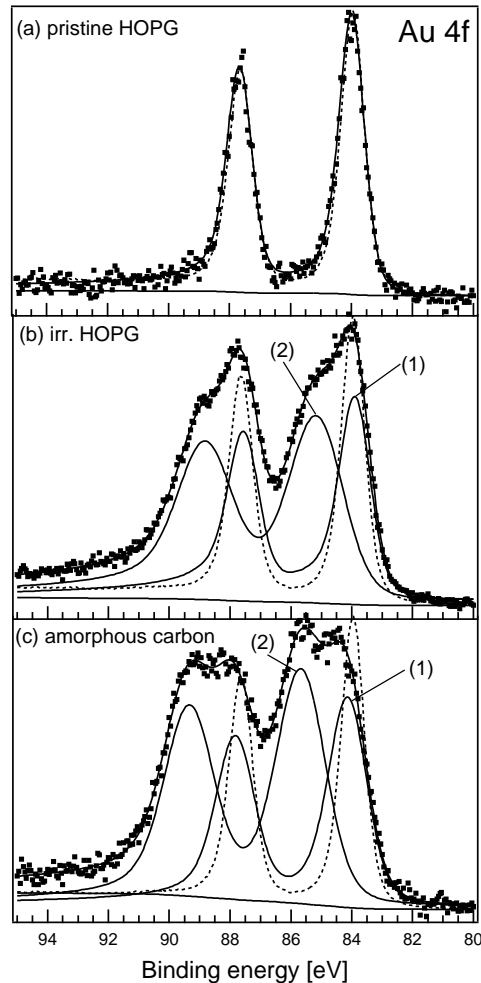


Figure 3.10: Au 4f core-level spectra for 0.1 Å Au onto (a) pristine HOPG, (b) argon-irradiated HOPG, and (c) amorphous carbon. The raw data (dots) is shown together with the decompositions (solid lines) and bulk gold reference spectrum (dashed lines). All spectra are normalized to equal height. See text for (1) and (2).

to 1.8 eV, which are smaller than the corresponding value for the gold reference. Due to the low gold coverage the spectra show a high level of noise, even after several hours of acquisition time.

The spectrum for pristine HOPG ($\Delta E=2.6$ eV) resembles strongly the gold reference. A significantly narrowed valence band on irradiated HOPG ($\Delta E = 2.2$ eV) and amorphous carbon ($\Delta E = 1.8$ eV) suggests the existence of comparatively small particles. For comparison, the 5d splitting for size-selected Au₅₅ is in the order of 1.9 eV.[74] This suggests particle sizes close or even below 55 gold atoms on amorphous carbon. $\Delta E=2.2$ eV (irr. HOPG) corresponds to particles with < 150 atoms.[56, 75]

Evaluation of gold core-level spectra gives more information on the electronic configuration. Au 4f core-level spectra for 0.1 Å (equivalent thickness) and the corresponding decompositions are presented in Fig. 3.10. The spectrum for deposition on pristine HOPG (Fig. 3.10(a)) exhibits features very similar to the gold reference, indicative to the existence of comparatively large particles. This agrees well with the interpretation of the corresponding VB spectrum. On substrates weakly interacting with deposited atoms, like pristine HOPG,[76] gold nucleation is characterized by diffusion-limited aggregation (DLA).[77, 78] Large clusters and a low nucleation density are expected on such substrates.

Gold deposited on irr. HOPG and amorphous carbon exhibits a different behavior, as can be seen in Fig. 3.10(b)+(c). In both cases the line shapes can be decomposed by two doublets, using Doniach-Sunjic profiles. One is located around the binding energy (BE) position for bulk (1), the other one is strongly shifted to higher BE (2). In contrast to pristine HOPG cluster growth is influenced by nucleation on defect sites. The diffusion constant is therefore reduced and a higher density of small particles can be found on the surface[79, 78, 72].

Both initial- and final-states could be the origin of the shifted doublet. Changes in the electronic configuration that are independent from the applied spectroscopic technique are called initial-state effects. These include shifts of electronic states due to different chemical states (e.g. oxidation, chemisorption) and quantum-size effects due to limited cluster dimensions (see 1.1.1). The photoemission final-state might also lead to shifted spectral features and it will be demonstrated in the following discussion that it is reasonable to assume this the dominating process. The initial-/final-state controversy is closely related to the existence of a bimodal particle size distribution. Initial-state effects cannot be completely ruled out, but have to remain speculative: Let us assume, the BE difference stems solely from initial-state changes, thus the mean cluster size is the same for (1) and (2). initial-state shifts in the order of 1 eV suggest chemical interaction. Positive shifts of 1.5 eV have been reported for plasma-oxidized gold clusters[80]. Such aggressive environments can surely be excluded in our case. Gold carbide formation was observed for ionized clusters in the gas phase[81], though being a very unstable species. If final-state effects are allowed to add to the shift, then doublet (2) has to origin from smaller particles compared to (1). Surface atoms become more important with reducing particle diameter and the corresponding surface core-level shift (-0.4 eV) has to be gradually compensated, as well. In summary, it is more likely that (2) stems from final-state effects and a bimodal size distribution, and the influence of the initial-state is rather minor.

As shown above Au 4f core-level shifts can be related to mean cluster sizes. Therefore, using the mean particle size estimations obtained from VB spectra, we identify doublet (1) with particles of < 55 (on amorphous carbon) and < 150 atoms (on irr. HOPG), respectively. Its broadened line shape compared to the reference is due to the particle size dispersion, for particles grown by evaporation usually characterized by a lognormal distribution.[82] One may argue, that the observed shifts for doublet (1) with respect to the gold reference are rather small for such particles. However, comparing available data from literature, binding energy shifts between 0.1-0.15 eV¹ and 0.3 eV² can be found, implying strong influence of the respective cluster and substrate preparation methods. Considering possible uncertainties in curve fitting and 5d-splitting determination, the cluster size assignments for (1) represent a reasonable. Crystalline orientation may also effect XPS VB spectra[87], but due to the large acceptance angle (cone of 12° half-angle) of the analyzer, such influence should be largely averaged out and is therefore neglectable. As for doublet (2), the strong BE shift > 1 eV with respect to (1) indicates the existence of gold atoms or clusters consisting of few atoms.[85] The FWHM (Full Width at Half Maximum) for doublet (2) is larger than for doublet (1), which can be explained by a higher sensitivity of Au 4f core-level shifts for size changes of very small particles.

In the case of defect-rich surfaces small clusters of few atoms grow at defect sites on the carbon substrate.³ Larger particles nucleate and grow on surface regions with higher atom mobility. This mechanism can explain the observed Au 4f core-level and valence band spectra

¹ligand-stabilized Au₅₅ on HOPG[74]; 1.6 nm Au cluster on diamond[83]; 1nm Au island on dithiol layer[84]

²Au₅₅ on SiO₂[85]; Au₃₃ on amorphous carbon[56];ligand-stabilized Au₅₅[86]

³Recently, core-level spectra of platinum clusters deposited on vacuum-cleaved HOPG have been investigated.[88] The authors observed a high binding energy component in the Pt core-level spectra on pristine HOPG, which they attribute to Pt atoms trapped at defects. This agrees well with the results presented in this work.

and indicates the existence of different adsorption energies on the carbon surface. It has indeed been shown in earlier silver scattering experiments on amorphous carbon, that two adsorption states with 1.8 eV and 1.3 eV trapping energy could be identified.[89] Although the actual values may be different in our experiments, it qualitatively supports our interpretation.

To further test our assumptions, we investigated the development of Au 4f core-level spectra as a function of the argon-ion irradiation time. Therefore, we prepared HOPG samples with increasing irradiation times, starting from pristine HOPG (0 s) to 90 s. As before 0.1 Å gold was evaporated on each substrate. It can be expected that the amount of gold actually *remaining* on the sample (determined by MXPS) depends on the irradiation time, thus, on the defect density.⁴ The raw data and corresponding decompositions of the two doublets are shown in Fig. 3.11(a). The intensity ratio (2)/(1) increases with irradiation time, confirming that the occurrence of (2) is directly related to the carbon surface defect density. The simultaneously raising gold concentration (Fig. 3.11(b)) is a good indication that the substrate's surface is not yet completely disordered at 60 s irradiation time, but can be expected to reach a saturation well above 90 s.

Alternatively, the number of displaced carbon surface atoms per impinging argon ion was estimated by using a computer code. This value helps to judge on the degree of surface disorder and may corroborate the above experimental results. Calculations have been performed using the freely available SRIM2003 computer code.[90] Fig. 3.12 shows the result for 3keV argon ions in graphite. The differential value for displacements ($\frac{\text{number}}{\text{ion} \cdot \text{Angstrom}}$) at or near the surface is 1.0 - 1.3, indicating that in average one carbon surface atom is displaced per incoming argon ion. Comparing with the total ion dose for 1 min irradiation ($3 \times 10^{13} \frac{1}{\text{cm}^2 \text{s}} \cdot 60 \text{s} = 1.8 \times 10^{15} \frac{1}{\text{cm}^2}$) with the graphite surface atom density ($\sim 4 \times 10^{15} \frac{1}{\text{cm}^2}$), this agrees well with results obtained from Fig. 3.11.

It is worth mentioning that although the two Au 4f doublets in Fig. 3.10(b)+(c) have comparable intensities and (2) originates from small clusters of few atoms, the corresponding valence band spectra in Fig. 3.9 do not show significant atomic-like features, i.e., well-separated narrow peaks. Although one may not expect to see free-cluster features [91, 92] in the case of supported particles, at least a distinct change in the valence band shape should be expected.

According to earlier works on fcc-metal deposition, differences in cluster nucleation and growth on amorphous carbon can be observed for Au and Ag.[93] We decided to perform experiments with silver in order to compare our results obtained for gold. Fig. 3.13 displays Au 4f and Ag 3d core-level spectra for particles on irradiated HOPG and amorphous carbon as a function of the equivalent thickness (0.1 Å to 1 Å). In the case of pristine HOPG (omitted in the graphs), no significant changes were observed for different coverages. In Fig. 3.13(a) the relative intensity of (2) diminishes quickly with increasing gold coverage, independent of the respective substrate. This behavior can be explained with proceeding cluster growth, as such process reduces the positive BE shift of (2), finally uniting (1) and (2).⁵

In the case of silver there is no evidence for a second doublet even for the lowest amount (0.1 Å). The doublet is asymmetrically broadened and shifted to higher binding energies for both substrates, which, is as in the case of gold, indicative for small particles and a non-zero size distribution. With increasing metal coverage (i.e., with increasing particle size) the binding energy shifts back towards the reference. The absence of a well-separated second doublet in all

⁴The extremely low sticking coefficient on pristine HOPG (0.05) is increased by surface defects.

⁵As mentioned before, a change in particle diameter of, e.g., 50 % induces stronger BE shifts for 1 nm than for 5 nm particles. This has the consequence, that core-level peaks originating from a bimodal cluster size distribution become more difficult to separate with increasing mean particle diameters. In other words, if (1) and (2) cannot be separated anymore, this does not necessarily imply the disappearance of a bimodal size distribution.

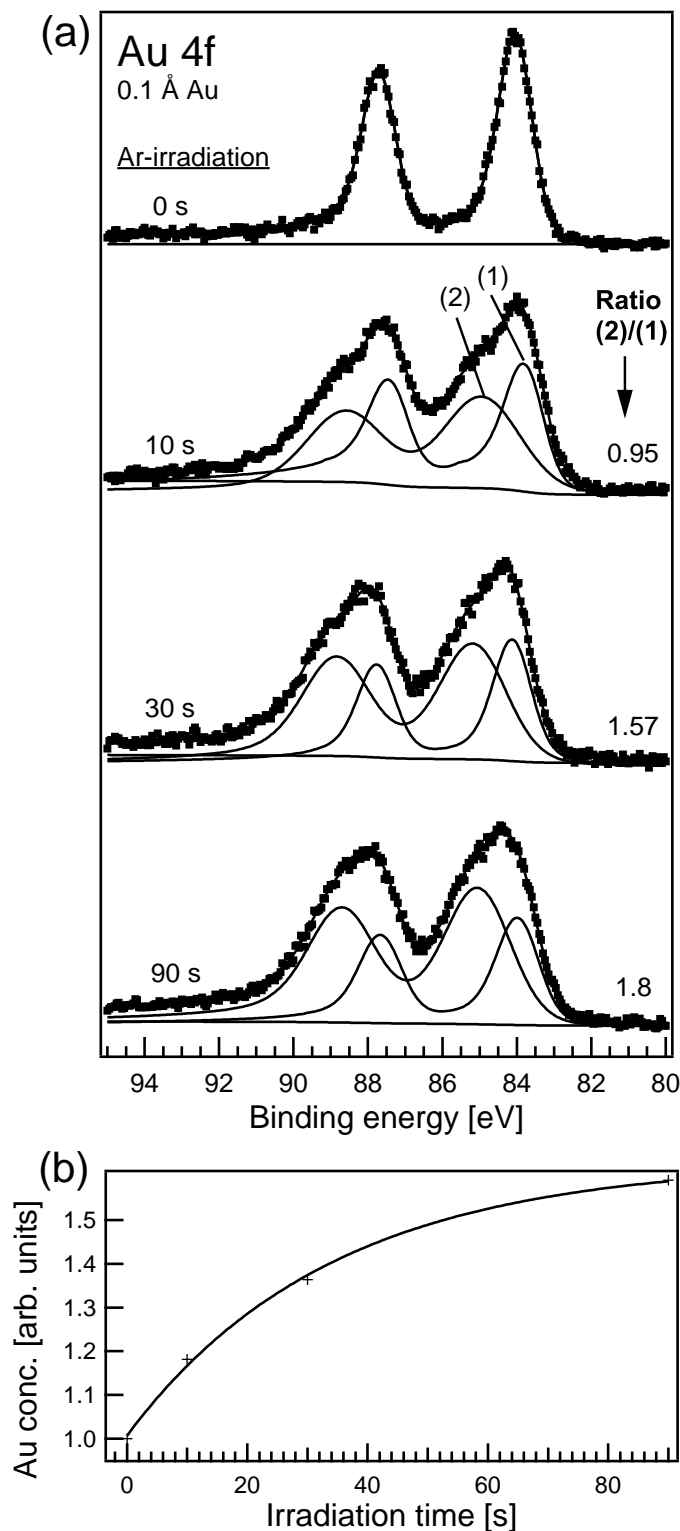


Figure 3.11: Variation of argon-ion irradiation time: (a) Au 4f spectra and corresponding decompositions. (b) Relative gold concentrations, calculated from C 1s (not shown) and Au 4f core-level lines (a). Data normalized to gold concentration of pristine HOPG (0 sec. irradiation). Solid line fitted to data using an exponential function.

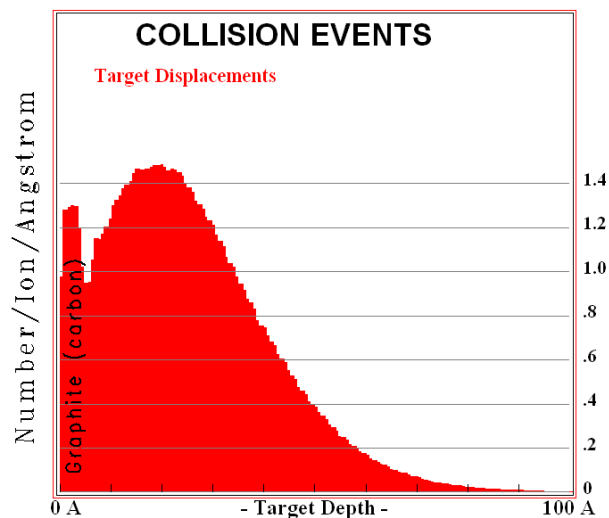


Figure 3.12: Results from SRIM2003 calculation (Ar-ions in graphite): The number of carbon atom displacements per incoming argon-ion is between 1 and 1.3 near the surface.

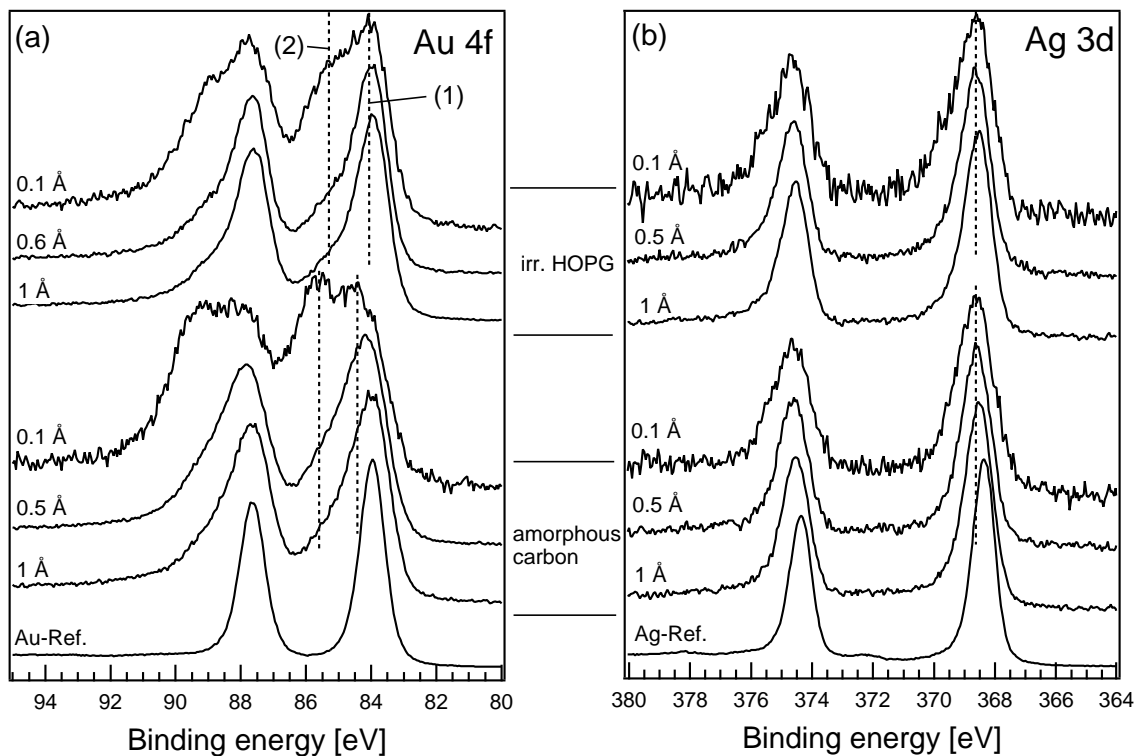


Figure 3.13: Evolution of the Au 4f and the Ag 3d core-level spectra as a function of the amount of evaporated metal on irradiated HOPG and amorphous carbon.

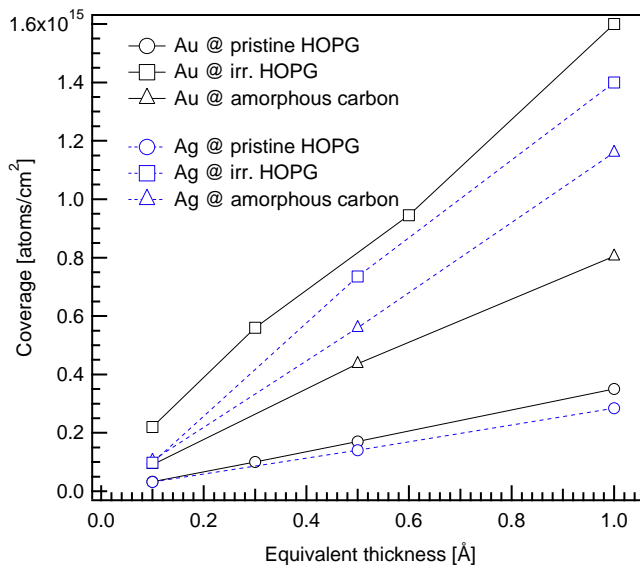


Figure 3.14: Gold and silver coverages calculated from MXPS spectra as a function of the evaporated equivalent thickness measured with a quartz crystal monitor.

presented spectra rules out the existence of a bimodal size distribution.⁶

As discussed earlier the presence of surface defects affects the sticking coefficient. Further information on nucleation and growth processes can be extracted from Fig. 3.14. The effective metal coverage (Au and Ag) is plotted as a function of the evaporated equivalent thickness. The coverage was calculated from MXPS core-level spectra, taking into account the inelastic mean free path of the substrate's core-level photoelectrons (C1s, 1200 eV kinetic energy), its density and the sample's angular orientation to the photoelectron analyzer.[95] For all samples investigated the coverage increases linearly with equivalent thickness, which is expected for cluster growth.

The linearity also confirms that the particle sizes are still beyond the threshold where it is necessary to consider mean electron escape depths for Au 4f electrons in MXPS. For particles with diameters in the range of several nanometers the innermost atoms would not be visible to MXPS. Such behavior would lead to a deviation from the linearity in Fig. 3.14. A similar effect should be expected, if direct impingement and capture of atoms on cluster surfaces played a considerable role in this process. The influence of surface defects becomes clear by comparing the coverage at a fixed equivalent thickness for different carbon substrates. The sticking coefficient on pristine HOPG is very low for gold and silver. Therefore, only a small fraction of the evaporated metal (equivalent thickness) remains on the substrate (coverage), the rest re-evaporates quickly from the surface. Thus, the lowest (effective) coverage can be found on pristine HOPG. This value is highly increased on irr. HOPG and amorphous carbon, where the nucleation probability is substantially larger due to defect-rich surfaces.

Deposition at Elevated Temperatures

In this part gold cluster nucleation and growth at higher substrate temperatures is investigated. Fig. 3.15 shows Au 4f core-level spectra (0.1 Å) on irr. HOPG and amorphous carbon as a

⁶In a recent publication[94] the growth of silver clusters on pristine and argon-ion-irradiated HOPG has been studied by means of STM and XPS. The presented Ag 3d spectra there are in good agreement with our results for silver.

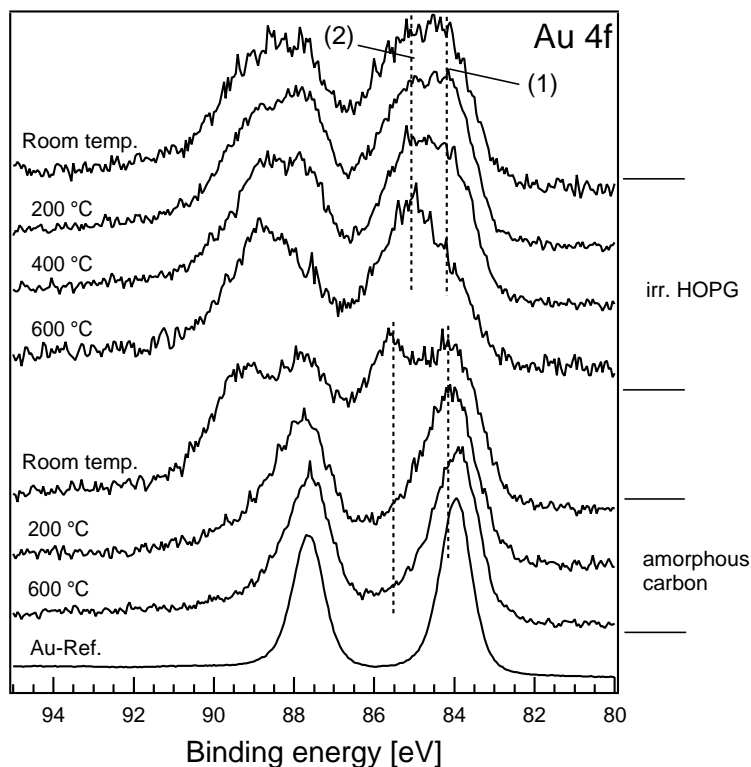


Figure 3.15: Evolution of Au 4f core level spectra for gold (0.1 Å deposited) on amorphous carbon and irradiated HOPG as a function of deposition temperature.

function of temperature (from room temperature to 600 °C).⁷

First, results for irradiated HOPG are discussed. The Au 4f doublet ratio progressively changes in favor of component (2) with increasing temperature. It dominates the spectrum at 600 °C. Following the interpretation for (2) presented earlier, this is an indication for a preferential growth of smaller particles at higher substrate temperatures. Since growth of larger particles takes place on surface regions with a high gold atom diffusion coefficient (i.e., weak atom-substrate interaction), increase of temperature may lead to quicker re-evaporation of impinging atoms. They remain on the surface, however, if they are captured by defects.

In the case of amorphous carbon, elevated temperatures cause the opposite effect. The two doublets, well-defined at room temperature, cannot be clearly identified at 200 °C. The spectrum is dominated by one doublet, which is located above the bulk binding energy (1). The broadened asymmetric shape may indicate still a small contribution from (2). Further temperature increase (600 °C) does not change the spectrum substantially, except a small shift towards the binding energy position for bulk gold.

The effective gold coverage as a function of the substrate temperature is shown in Fig. 3.16. The curve for irradiated HOPG begins to decrease above 200 °C and drops to 1/3 of the initial value for 600 °C. The changes are less drastic ($\approx 20\%$) for amorphous carbon. The comparison of the results for irradiated HOPG and amorphous carbon at elevated temperatures suggests significant differences in the trapping energies of the two substrates. We infer that for the defects created on HOPG by argon irradiation those energies are higher than for the intrinsic defects on our amorphous carbon. Nevertheless, the energy needed to escape from the carbon surface seems to be higher for amorphous carbon, as Figure 3.16 suggests.

⁷As mentioned before, each curve represents a freshly prepared sample. The reproducibility of the results was verified by comparing spectra of identically processed samples.

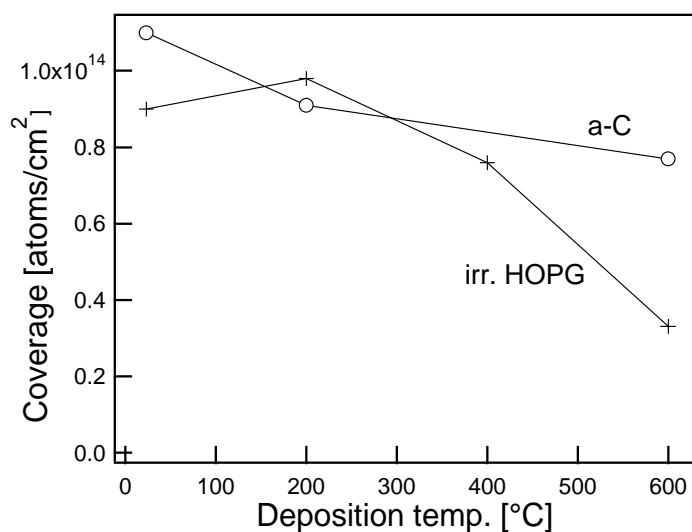


Figure 3.16: Gold coverage (for 0.1 Å equivalent thickness) as a function of the deposition temperature for irr. HOPG and amorphous carbon.

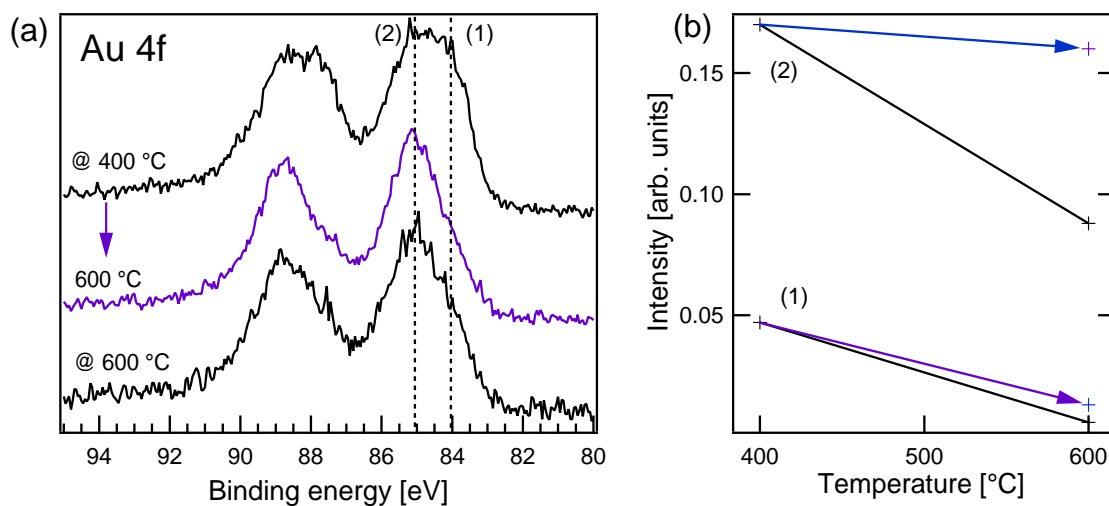


Figure 3.17: 0.1 Å gold on irradiated HOPG: (a) Au 4f core-level spectra for deposition at 400 °C, the same sample annealed to 600 °C afterwards and deposition at 600 °C. (b) Relative abundance of (1) and (2) calculated from (a) as a function of the temperature. Arrows indicate post-deposition annealing, solid line deposition at the corresponding temperature.

An interesting question was how the Au 4f spectra change after annealing the samples (*after deposition*) at a defined temperature and to compare with corresponding spectra of *depositions at that temperature*. The experiment was restricted to irradiated HOPG as substrate. Fig. 3.17a shows the results for irradiated HOPG. The top curve corresponds to 0.1 Å gold deposited at 400 °C substrate temperature (same data as in Fig. 3.15). This sample was afterwards annealed to 600 °C, yielding the spectrum displayed in the middle. Comparison with the spectrum obtained from a sample *deposited* at 600 °C (bottommost curve) reveals a surprising resemblance. Both spectra show doublet (2) as the dominating part, indication of clusters captured at surface defects. A difference arises when comparing the relative abundance (with respect to the carbon substrate) of (1) and (2) for the two temperatures, as plotted in Fig. 3.17b. At 600 °C the relative abundance of (2) exhibits a significant difference between the annealed sample and the deposited sample, being much lower for the latter one. Values for (1) do not differ that much. The experimental results shown in Fig. 3.17 give an estimation of the thermal stability of HOPG surface defects created by ion bombardment. We interpret the spectra as follows: Deposition at 600 °C strongly reduces the sticking probability and promoted preferential nucleation at defects, as mentioned in Sec. 3.2.1. Annealing from 400 °C to 600 °C increases the atomic mobility allowing already formed clusters (on not-irradiated substrate regions) to dissociate. Gold atoms move on the surface and are either captured by non-occupied defect sites or escape from the substrate. Therefore, it can be assumed that defects remain stable (or 'active') in the examined temperature range.

It should be pointed out that the carbon C 1s core-level spectra did not show changes upon gold deposition compared with the reference, i.e, the uncovered substrate. However, this does not necessarily imply absence of any interaction of the metal with the substrate. Due to the low coverage a possible carbon contribution from the surface layer is surmounted by the signal from the underlying substrate. Therefore, increasing the surface/bulk signal ratio by increasing the electron escape angle may be of help for future experiments. Further investigation has to be performed to study the influence of elevated temperatures on the nucleation process on amorphous carbon in more detail. In a recent publication[96], interactions of gold clusters with amorphous carbon surfaces has been investigated theoretically and experimentally. Small clusters (< 1 nm) were found to be pinned at small intrusions on the carbon surface. One could speculate, that such mechanism leads to the observed core-level spectra (two doublets) at room temperature. At elevated temperatures, however, morphological changes (e.g., graphitisation[97]) may cause these intrusions to disappear. That could explain the absence of doublet (2) for higher substrate temperatures.

Typical Scanning Electron Microscopy (SEM) images of deposited gold clusters are shown in Fig. 3.18. They demonstrate the influence of surface defects on gold nucleation. The same amount of gold (1 Å) was evaporated on the three substrates. As mentioned before, gold evaporation on pristine HOPG (a) leads to large irregular structures based on the high atomic mobility. Presence of surface defects yields a more uniform, round-shaped ensemble of particles. The low sticking coefficient is responsible for the lower amount of atoms actually remaining on the pristine HOPG substrates compared to the other ones investigated. Therefore, when comparing three samples with the *same* gold coverage, the difference in cluster size and shape between the a) on one side and b) and c) on the other side would be even more dramatic. Particle sizes in (c) (amorphous carbon) appear to be larger than in (b) (irradiated HOPG), which is conflicting with the size estimations drawn from Fig. 3.9. However, as the coverage in Fig. 3.18 is 10 times higher and the exact nucleation/growth process on the two carbon substrates is not yet fully understood, the images presented here shall illustrate qualitative differences promoted by surface defects.

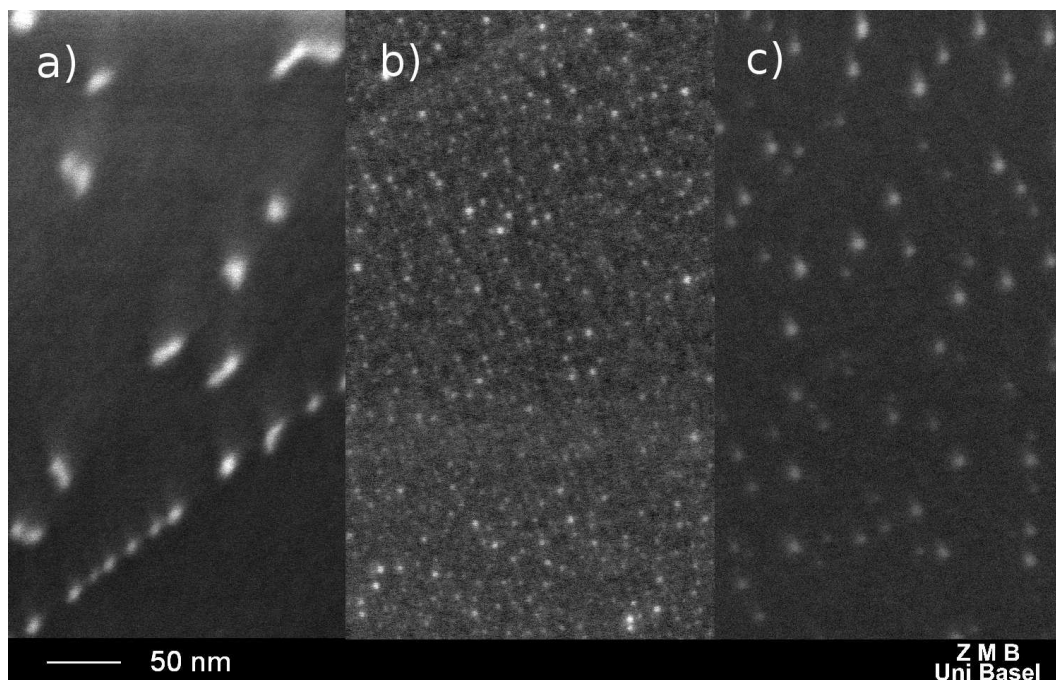


Figure 3.18: SEM images of evaporated gold (1 Å) on different carbon substrates: Pristine HOPG (a), argon-irradiated HOPG (b), and amorphous carbon (c).

Conclusion

The early stages of gold nucleation at defect sites have been studied on HOPG and amorphous carbon surfaces by means of X-ray Photoelectron Spectroscopy. Nucleation on amorphous carbon with its intrinsic defect density was compared with argon-irradiated HOPG substrates. Pristine HOPG samples were prepared as a reference system with weak metal-substrate interaction. For low gold coverage (0.1 Å equivalent thickness) Au 4f core-level spectra on defect-rich substrates surprisingly revealed a two doublet structure. With the aid of cluster size estimations obtained from MXPS valence band spectra, we interpret the BE shift (≈ 1 eV) between both doublets as indicative for a bimodal particle size distribution. The strongly shifted doublet is directly related to surface defects and stems from gold clusters of just a few atoms. The doublet located at lower BE can be assigned to clusters roughly between 55 and 150 atoms. Identical experiments performed with silver did not reproduce a similar core-level feature, suggesting distinct differences in atom-substrate interactions between Au and Ag. Gold deposition at higher temperatures revealed the possibility to preferentially growth small particles located at defect sites on argon-ion irradiated HOPG. These findings may prove useful to refine control of particle nucleation and growth, facilitating surface nanostructuring. SEM imaging was used to demonstrate the influence of surface defects on gold particle morphology.

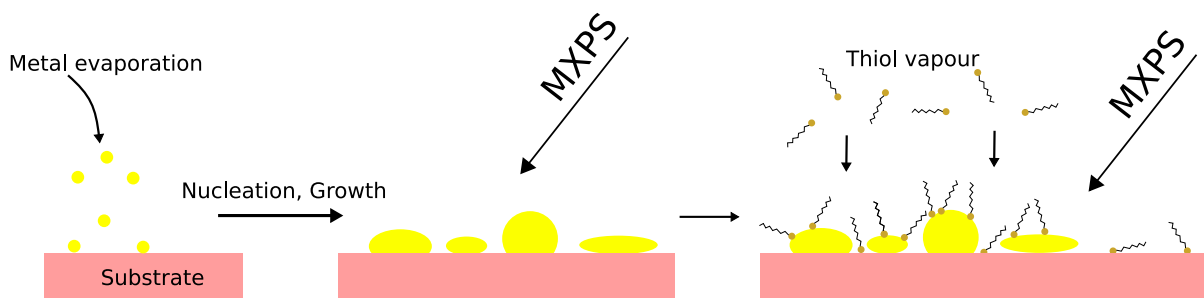


Figure 3.19: Cartoon illustrating the different steps of the thiol adsorption experiment.

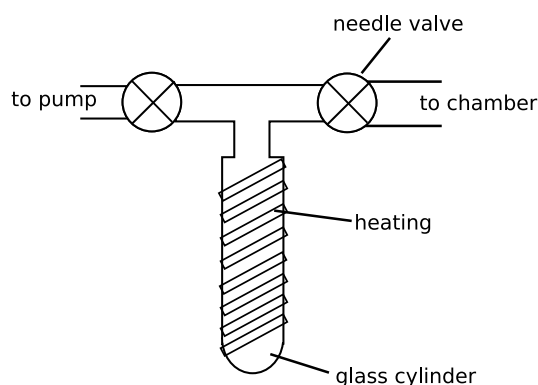


Figure 3.20: Setup for thiol adsorption experiment: The glass cylinder contains the thiol liquid can be heated resistively from outside. Before opening the needle valve, ambient gases are removed by a mechanical pump.

3.2.2 Thiol Adsorption on Noble Metal Clusters

Having studied gold and silver evaporation on the different carbon substrates and estimated the mean particle size the next step was to prepare clusters on a substrate and to adsorb thiol molecules. Most of the results presented here were published in 'M. Büttner, K. Kröger, I. Gerhards, D. Mathys, and P. Oelhafen, *Changes in the electronic structure of gold particles upon thiol adsorption as a function of the mean particle size*, *Thin Solid Films* 495 (2006) 180'.

Introduction

The gold-core/thiol-shell system is widely used in nanoscience research and thus, detailed knowledge about core/shell interactions is of high importance. In the case of a nanoparticle surrounded by a passivating shell, one may not be able to assign observed phenomena to either being intrinsic properties of the core or being due to the organic shell. Ways to overcome these restrictions would be either to remove the organic molecules after sample preparation or to adsorb the molecules on the previously naked particles. In this study thiol molecules were adsorbed on gold nanoparticles (see Fig. 3.19) and the changes of the clusters' electronic configuration studied as a function of the mean particle size. MXPS measurements were applied to examine the changes in Au 4f core-level and valence band spectra upon thiol adsorption.

Experimental Details

For the thiol adsorption experiments a glass cylinder with hexadecanethiol (HDT) was connected to the vacuum chamber via a needle valve (Fig. 3.20). The glass cylinder was attached to a mechanical pump to remove ambient gases. To increase the thiol vapor pressure the glass

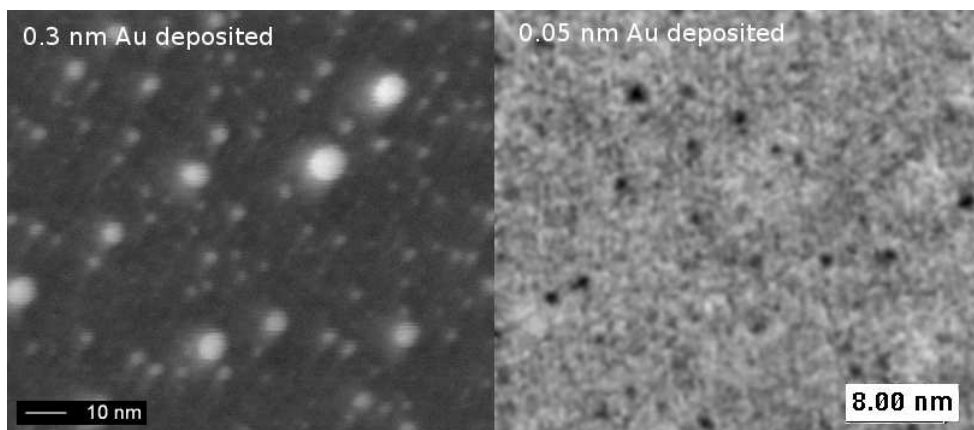


Figure 3.21: Typical SEM (left) and TEM (right) images of the discontinuous gold film.

containment has been resistively heated with a surrounding metal wire. The samples (kept at room temperature) were exposed to a thiol atmosphere of 1×10^{-6} mbar during 1 h.

In order to monitor possible changes in the electronic configuration of the gold particles, MXPS was performed before and after thiol adsorption. Core-level lines of gold (Au 4f), sulfur (S 2p) and carbon (C 1s) and valence band spectra have been measured with MXPS. The Au 4f_{7/2} reference for bulk gold was at 83.8 eV.

TEM and SEM images of the evaporated gold particles have been taken in order to determine the mean diameter. For TEM imaging, carbon coated TEM grids have been used as substrates on which a 4 nm carbon film has been deposited in the vacuum chamber in order to provide the same carbon surface for all samples used in the experiments.

Results and Discussion

Fig. 3.21 shows typical SEM and TEM images of the gold particles. The particle diameter determination provides a calibration curve, shown in Fig. 3.22, to estimate the mean particle size from the evaporated Au thickness as determined with the quartz crystal monitor. Samples with different Au thicknesses have been prepared which are marked on the top border and to which we will refer as sample (a)-(f), with mean particle diameters obtained from this graph. Sample (c) and (f) are identically prepared, but (f) has been stored in ambient air for one week before thiol adsorption.

Fig. 3.23 shows Au 4f core-level spectra before and after thiol adsorption with decreasing mean particle diameter from bottom to top (samples (a)-(e)). Samples (c)-(e) exhibit increasingly broadened spectral features. This stems from the non-zero particle size distribution as discussed in 3.2.1. Comparison with the corresponding spectra *after* thiol adsorption shows two important effects: Firstly, the peaks appear much more narrow, the strong shoulder on the high BE side is diminished. Secondly, the spectra exhibit positive binding energy shifts upon thiol adsorption. Sample (f) does not show any change in line shape or BE. Experiments performed on gold foil did not yield changes of spectral features, as well.

One could expect that thiol-gold interaction leads to Au atom species that experience two different chemical environments: Core atoms (Au surrounded by Au) and atoms on the surface (Au-S bond). This should contribute to a further spectral broadening, which is clearly not observed. The narrow core-level peaks suggest that the sulfur-cluster interaction affects the cluster as a whole. Very recently a work was published that might give an explanation of this observation.[99] The authors studied surface plasmon resonance (SPR) of thiol-capped gold nanoparticles and developed a model for SPR damping due to thiol-cluster interaction

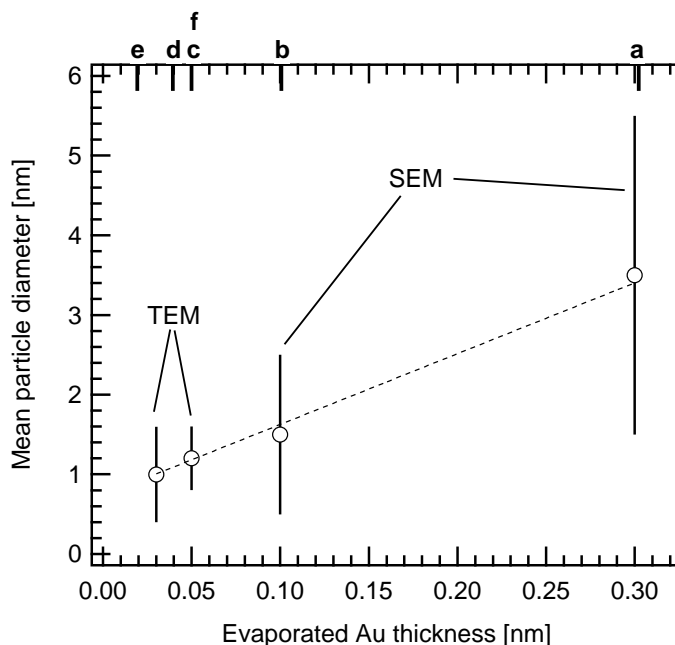


Figure 3.22: Particle size as a function of evaporated gold thickness, calculated from TEM and SEM images. Standard deviation for the mean particle size is indicated by the bars. The dashed line serves as a guide to the eye. (a)-(f) indicate the different prepared samples.

(chemical interface damping). They conclude that such interaction affects the cluster atoms within a distance of 0.7 nm from the surface. For spherical clusters smaller than 1.4 nm (diameter) all atoms are affected. If clusters are rather flat (high aspect ratio) this holds true even for larger diameters. Therefore, the positive binding energy shifts reflect the new chemical environment (initial-state) caused by the creation of S-Au bonds. The shift is size-dependent and is larger for small particles.

The peak narrowing induced by thiol molecules deserves a closer look. To illustrate this phenomenon Fig. 3.24 presents Au 4f core-level spectra for 0.1 Å on amorphous carbon (a-C). The *as-deposited* spectrum (top) is decomposed by doublets (1) and (2) corresponding to two mean cluster sizes as discussed in 3.2.1. After exposure to thiol vapor the relative intensity of the two curves significantly changed. Evaluating the binding energy positions of (1) and (2) on both substrates it becomes clear that (1) shifts to higher binding energy, whereas (2) roughly retains its position after adsorption. Theoretical and experimental studies on thiol passivated gold clusters revealed a unusual high particle mobility on graphite surfaces promoted by interactions between the surface and the passivating shell.[69, 65] The calculations show that thiol molecules act as a ‘lubricant’ between the cluster and the support. With this background one could speculate that exposure to the thiol atmosphere may allow the smallest clusters (trapped at defect sites) to move and being captured by larger particles.

The sample exposed to ambient air (sample (f)) does not show any change of its Au 4f core-level spectra. This means that the cluster’s surface has been completely passivated and thus thiol molecules cannot bind to it. Therefore, one has either to keep the samples under vacuum conditions throughout the different preparation steps or to apply a cleaning procedure, e.g. plasma etching. For further discussion of the core-level shifts it is recommended examine the corresponding VB spectra.

Fig. 3.25 shows VB spectra measured before and after thiol adsorption.⁸ As in the case

⁸Due to the featureless carbon VB spectrum (in MXPS) no background subtraction was necessary.

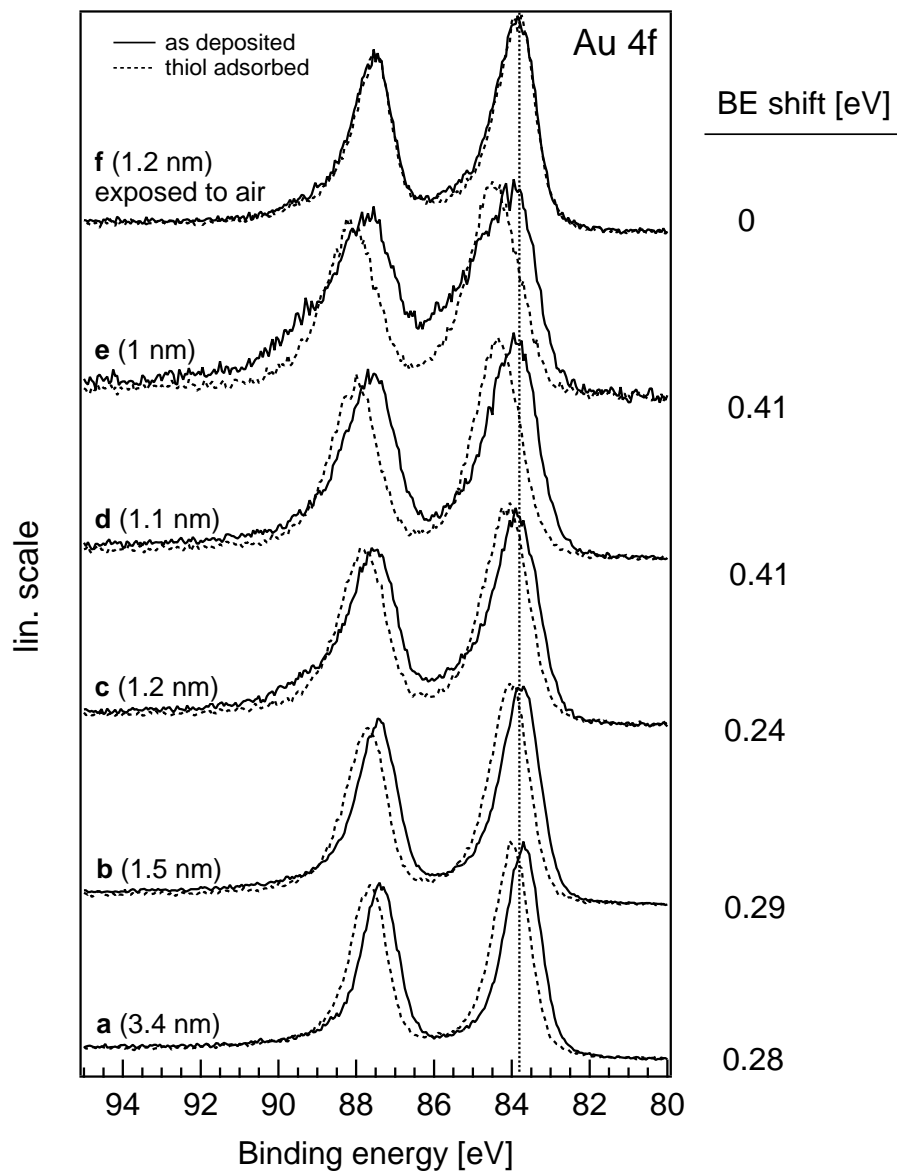


Figure 3.23: Au 4f core-level spectra before (solid lines) and after (dashed lines) thiol adsorption for the different samples, with mean particle diameter in parentheses. Au reference at 83.8 eV (vertical dashed line). Thiol-induced binding energy shifts shown on the right side.

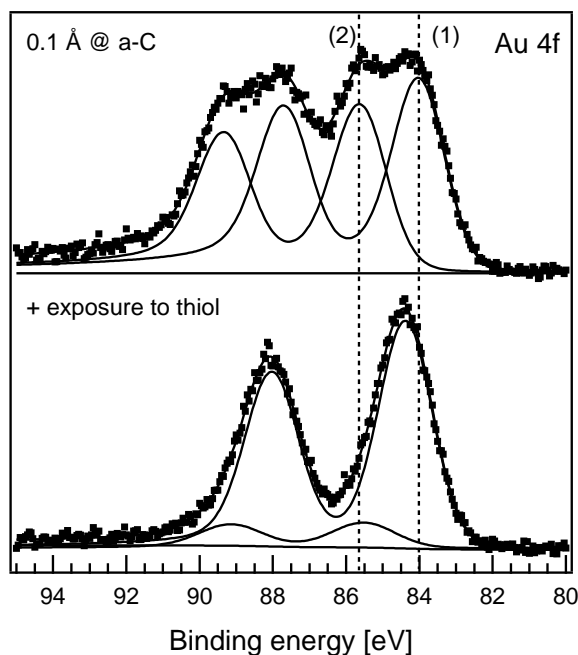


Figure 3.24: Gold evaporated on amorphous carbon: Exposure to thiol atmosphere strongly reduces intensity of (2) and shifts (1) towards higher binding energies.

of the Au 4f core-levels the corresponding VB spectra exhibit positive BE shifts. In order to facilitate comparison of the line shapes, the spectra have been superposed in the graphs, as indicated in Fig. 3.25a.⁹ The results are shown in Fig. 3.25b, together with the corresponding binding energy shifts. Arrows indicate regions with increase or decrease of signal intensity, i.e., valence electron density.

The main feature (8 eV to 2 eV) shows the density of states of the Au 5d electrons. Above this region mainly 6s and 6p electrons are located, partly hybridized with 5d orbitals.[75, 100] For sample (a) the most significant change can be found between 2 eV and 4 eV binding energy (II) and shows a strong decrease of electron density after thiol adsorption. A comparatively small increase in electron density can be observed around 1.25 eV (I). With decreasing particle size the area of region (II) is reduced, whereas region (I) slowly increases. Additionally, the valence band exhibits a lowered electron density between 6 eV and 8 eV (III), which intensifies with smaller particle size (samples (b)-(e)). The changes in (I) and (II) can be interpreted as re-hybridization of 5d orbitals to form molecular orbitals (MO) with the sulfur, as from Density Functional Theory (DFT) calculation the Au-S MO are expected to be found between 1 eV - 2 eV above the 5d VB orbitals. Mostly Au 5d and S 3p orbitals take part in this bond.[101] The air-exposed sample (sample (f)) does not show such changes in the valence band.

Having discussed the impact of thiol adsorption on the VB spectra, the examination now focused on BE shifts. Both Au 4f core-level and the VB shifts are shown for comparison in Fig. 3.26 as a function of the particle size. As can be seen, the thiol-induced BE shifts increase with decreasing particle size. For experiments on a Au foil no detectable shifts in either Au 4f core-levels or VB spectra were observed. This can be understood in terms of an increasing number of surface atoms compared to the total number of atoms in a cluster. Theoretical DFT calculations combined with Mullikan population analysis yield a net electron charge of 0.31 per sulfur atom for adsorbed thiol.[102] Combined with the increased surface atom/bulk atom

⁹The *thiol adsorbed* spectrum has been moved to lower binding energy to align the Au 5d_{3/2} peaks of both curves (*as deposited* and *thiol adsorbed*).

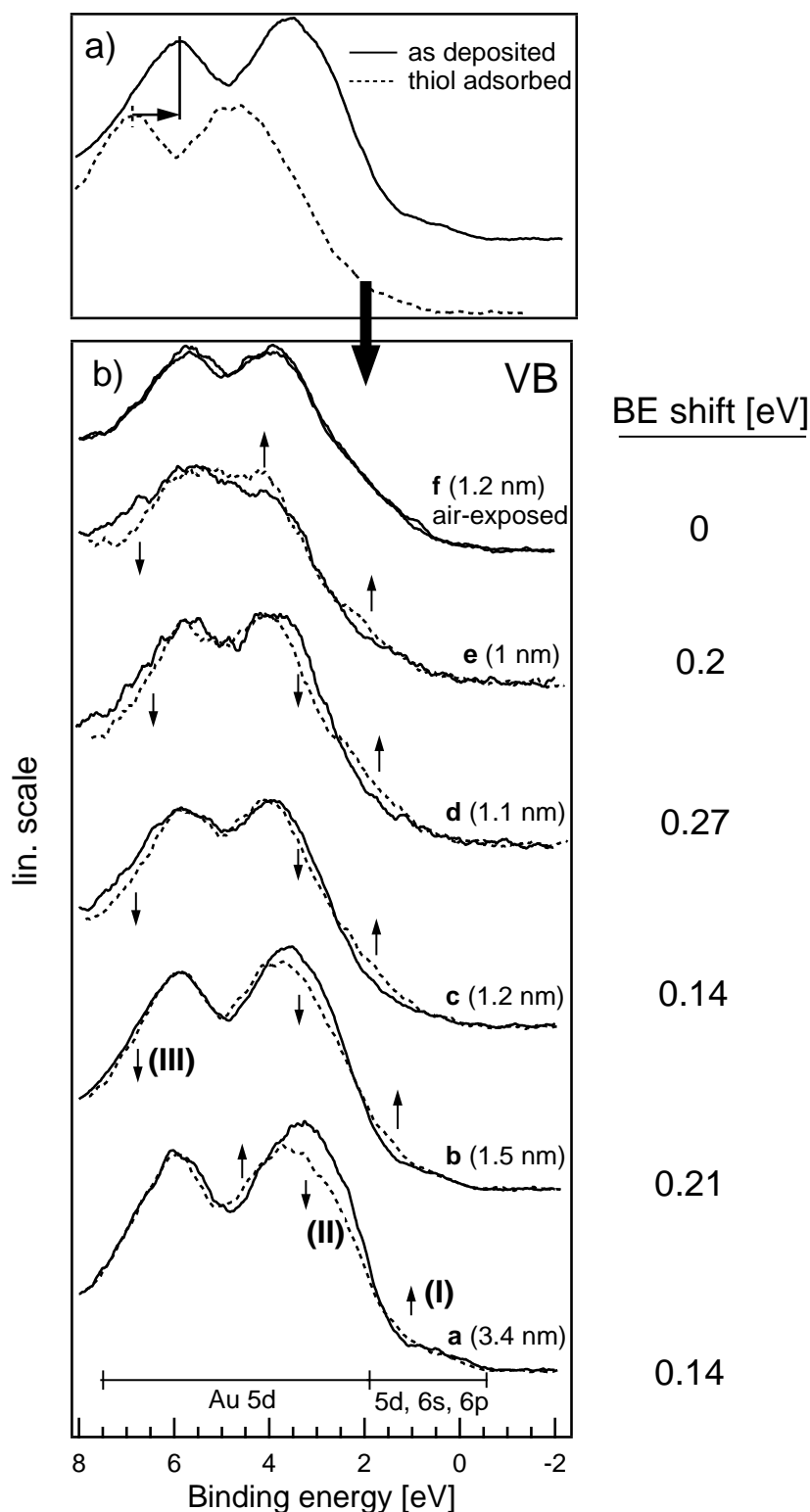


Figure 3.25: Smoothed valence band spectra of the examined samples: (a) For ease of line shape comparison, each dashed curve has been manually shifted in the graph to align the Au $5d_{3/2}$ peaks (vertical solid and dashed line). (b) Arrows indicate regions where thiol adsorption leads to increase or decrease of intensity. See text for (I), (II), and (III).

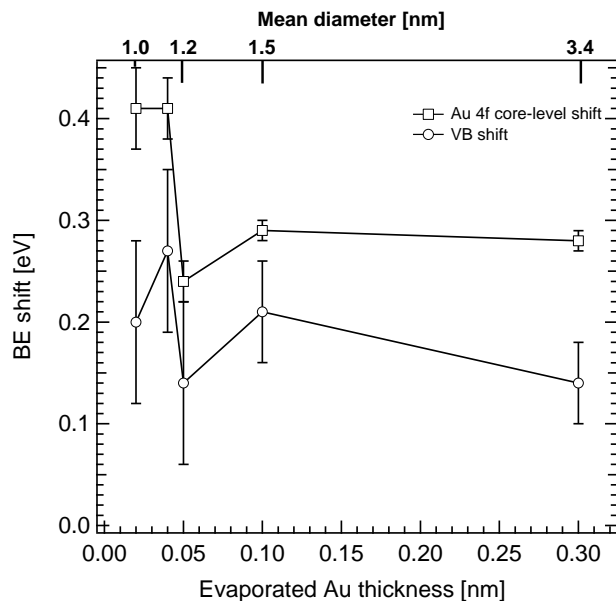


Figure 3.26: Comparison of Au 4f and VB binding energies

ratio this means, that the smaller the particles become, the more VB electrons relative to the total atom count are localized by thiol molecules.¹⁰ Therefore, the relaxation and the charge screening properties of the gold cluster are influenced, which affects the measured binding energy.

The possible change of the dielectric constant around the gold core due to the organic molecules can be ruled out as another influencing factor, because a raised ϵ would lead to a higher capacitance of the cluster which in turn would reduce the Coulomb interaction between cluster and photoelectron. The effect would be a negative binding energy shift, which is not observed.

Another possibility is the existence of cluster lattice distortions induced by thiol adsorption.[67] One may speculate, that the changes in Au-Au interatomic distances could alter the electron orbital overlap and thus change the electron binding energies. Such interpretation would also be supported by the valence band spectra in Fig.3.25. As shown, thiol adsorption leads to a valence band narrowing, which would also be expected in the case of reduced orbital overlap. The thiol-induced binding energy shifts of the valence band follow the core-level shifts, but with smaller values. For mean diameters < 1.5 nm jumps can be observed in the binding energy shift. A satisfying explanation of this feature cannot be given yet.

The evaluation of the S 2p core-level spectra (not shown) yielded a S 2p_{3/2} binding energy of 162.7 eV, which is somewhat between the value for S-Au bonds (162.4 eV) and thiol species not bonded to gold (163.5 eV).[98] This can be explained by the fact that a fraction of thiol molecules also adsorb directly onto amorphous carbon. This was checked by exposing the uncovered carbon substrate to the thiol atmosphere. Detailed investigations still have to be carried out to quantitatively estimate this fraction.¹¹ To confirm that the previously observed changes are due to sulfur-gold interactions and not due to the influence of contaminants and residual gases in the vacuum chamber we substituted hexadecanethiol by hexadecane and carried out the adsorption experiment. As expected, hexadecane had no effect on Au core-level and valence

¹⁰Given that the thiol molecule surface density on the gold cluster does not vary much

¹¹The calculations of the S/Au ratios from the peak intensities and the photoionization cross sections lead to values between 0.23 and 0.37, depending on the evaporated gold quantity. Due to thiol molecules adsorbed on carbon, the S/Au ratio for thiols on gold is overestimated.

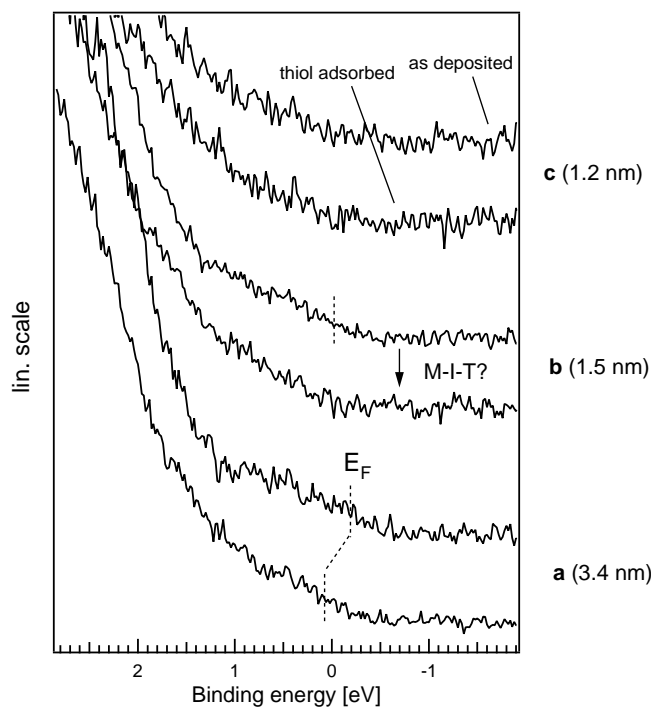


Figure 3.27: Valence band near the Fermi edge region of samples (a),(b), and (c) before and after thiol adsorption. Possible thiol-induced metal-insulator-transition (M-I-T) for sample (b).

band spectra.

The existence of a Fermi edge is a reliable indication of metallic character. Chemical interaction with the cluster's environment may lead to a disappearance of this feature. It has been shown that the interaction of chlorine atoms with Au_{55} clusters (6 Cl atoms per cluster) can induce a metal-insulator-transition.[74] One might expect a similar behavior for thiol with its sulfur headgroup. Due to the lower electronegativity of sulfur compared to chlorine, this effect is possibly weaker. Therefore, the Fermi edge was examined in terms of changes due to S-Au interaction. Fig. 3.27 displays the Fermi energy region for samples (a)-(c). For sample (a) both curves (before and after thiol exposure) show a Fermi edge, whereas for sample (c), the corresponding spectra do not exhibit such feature. This suggests a metal-insulator-transition caused by the finite-particle size (Quantum Size Effect). Sample (b) is somewhat in between. The *as-deposited* spectrum shows a Fermi edge feature, which is not observable for the *thiol adsorbed* spectrum. This observation can be interpreted as a thiol-induced metal-insulator-transition due to localization of electrons. However, the data do not unambiguously prove this assumption because of high statistical noise. Further experiments should be performed to clarify this question. To improve future results the statistics should be enhanced¹² and the particle size dispersion reduced by depositing size-selected clusters, for example.

Conclusion

The results presented here show that the interaction of the thiol sulfur headgroup with the cluster surface leads to a positive binding energy shift in the Au 4f core-level. No line width broadening could be observed, which indicates that the thiol-gold interaction affects the whole particle and not only the surface, where the actual Au-S bond is located. In fact, one can observe

¹²A first approach would be to heavily increase the number of scans and to limit the measured energy range to the necessary minimum.

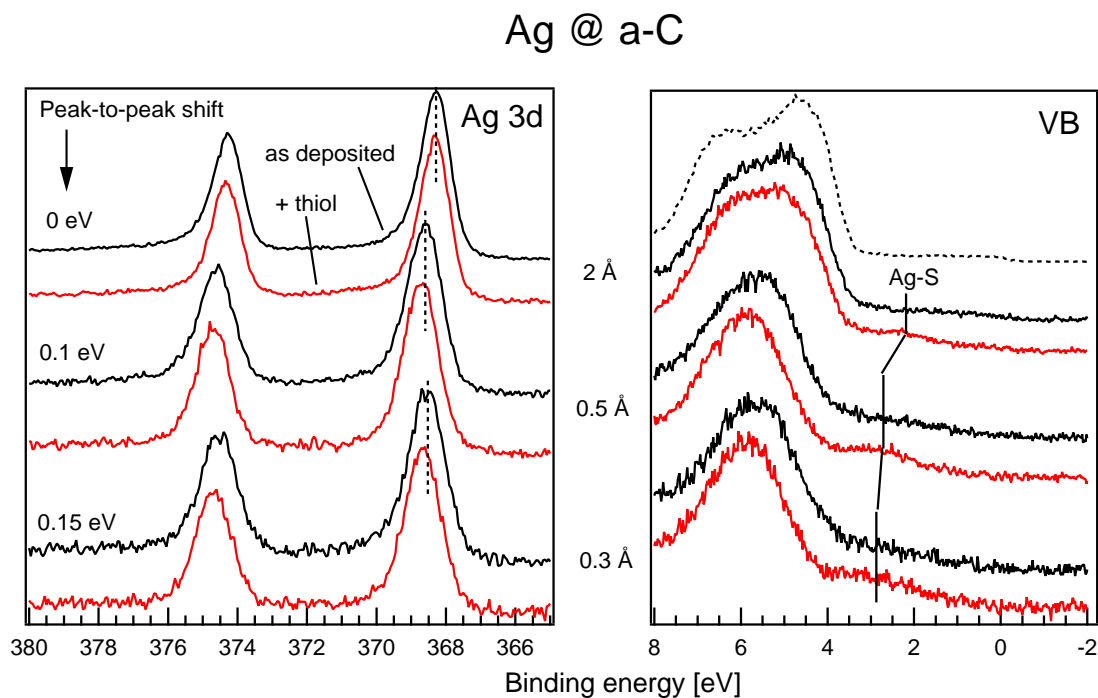


Figure 3.28: Thiol adsorption on silver supported on amorphous carbon as a function of the evaporated amount: *Left:* Ag 3d core-level show a positive binding energy shift, however, smaller than in the case of gold. *Right:* The valence band exhibits a new feature (Ag-S) due to the creation of sulfur-silver bonds.

rather a narrowing of the line width for smaller particles. The positive binding energy shifts depend on the cluster size and increases with decreasing diameter. A maximum shift of 0.41 eV could be measured for the smallest particles (~ 1 nm). The valence band spectra exhibited positive binding energy shifts similar to the Au 4f core-levels, but smaller in absolute values. Changes in the valence band shape were interpreted as re-hybridization of Au 5d electrons due to the creation of Au-S bonds. Furthermore, we observed the disappearance of the Fermi edge upon thiol adsorption, which we attribute to a sulfur-induced metal-insulator-transition of the gold cluster. The experiments show that thiol adsorption on gold clusters induces phenomenologically similar changes in the electronic properties as it is known from finite-size effects in naked, i.e. uncovered, gold particles. For experiments with metal-core/organic-shell particles this has the consequence that it may be difficult to determine, if a measured feature is an intrinsic property of the metal-core or due to core/shell interactions. On the other hand, our findings also show the feasibility to tune certain properties of deposited gold particles by thiol adsorption. This is especially relevant for molecular electronics applications. Sulfur-gold bonds are widely used to attach molecules to electrical leads in order to investigate electronic transport through the molecules. Therefore, the resistivity of such contact has strong impact on the experimental results and the detailed knowledge of its electronic properties is crucial.

3.2.3 Ongoing Work / Outlook

Thiol-Adsorption Experiments on Silver

In an earlier investigation of metal cluster nucleation and growth on carbon substrates (sec. 3.2.1) differences in core-level spectra between gold and silver have been observed. To gain a better understanding of this phenomenon the thiol adsorption experiments have been repeated

on silver. Fig. 3.28 displays Ag 3d core-level and VB spectra for three different metal coverages. The peak-to-peak values given in the left graph correspond to changes of peak positions before (top curves for each coverage) and after thiol adsorption (bottom curves), thus being thiol-induced. In agreement with gold/thiol results the shift increases with decreasing coverage (cluster diameter). However, the absolute value (0.15 eV for 0.3 Å) is much lower compared to gold.

In the right graph of Fig. 3.28 the corresponding MXPS VB spectra before and after thiol adsorption are shown. They are dominated by Ag 4d valence band electrons. The band width for the as-deposited samples is significantly reduced compared to the Ag reference (dashed curve) due to the finite size of the particles. Exposure to the thiol atmosphere results in a further slightly narrowed band and a small positive BE shift. This effect is most prominent for the lowest metal coverage (bottom). Spectra measured after thiol exposure exhibit a new feature (solid lines), which can be identified as sulfur-derived valence band states. In connection with the valence band narrowing and the positive BE shifts observed in the spectra, this is a good indication for sulfide formation.[103]

One could speculate that the small thiol-induced core-level shifts (with respect to gold) could be explained by higher distance between the Ag 4d valence band electrons and the S-derived states and thus implying weaker interaction upon thiol adsorption. As 4d orbitals are more localized than 5s, configurational changes have a higher impact on initial-states of lower-lying core-levels. Theoretical DFT calculations (for thiolated [Ag/Au]₁₃ clusters) yield S-states located above the 4d band for Ag and amongst 5d states for Au, respectively. Unfortunately the Fermi edge cannot be identified easily due to the low intensity of Ag states near E_f . It would be interesting to check for possible metal-insulator transitions as in the case of gold.

Experiments with Propanethiol

To check for thiol chain length dependencies of the results experiments were performed with propanethiol.¹³ As propanethiol is much more volatile than hexadecanethiol no additional heating of the glass tube was necessary. All other parameter were chosen as before. The results obtained were similar to hexadecanethiol, i.e., a positive core-level and VB shift after thiol adsorption: 0.32 eV and 0.22 eV, respectively, for 0.1 nm gold and 0.16 eV and 0.12 eV, respectively, for 0.3 nm. Therefore, we can expect that the intermediate lengths behave in the same way concerning the influence on the cluster. However, the geometric orientation and the molecule density on the cluster surface can be expected to vary due to steric effects of the chains. It may also provide a possibility to reduce the desorption time, as partial pressures higher than 1×10^{-6} mbar can be reached more easily with shorter chains. Propanethiol, however, is not a good candidate, as it is highly volatile and quickly poisons the ambient air with a strong stench, making it difficult to handle. Furthermore, it dissolves in mechanical pump oil and spoils it.

¹³corresponding to a thiol chain with 3 carbon atoms

3.3 C₆₀ on Carbon Substrates

3.3.1 Adsorption / Desorption Studies

The study was extended to fullerene molecules on carbon substrates in order to examine the possibility of attaching C₆₀ cages to surface defect sites. This is especially interesting as fullerenes are often used as scaffolds for functionalized molecules and a controlled deposition of these systems may open possibilities for new applications.

Introduction

To build and study nanoscale devices based on fullerenes one has to be able to arrange these molecules on suitable surfaces. Fullerenes deposited on carbon are regarded as only weakly interacting with the substrate. They physisorb on HOPG planes by van-der-Waals forces. There is evidence that carbon atoms may act as linkers between fullerene cages, thus, forming polymerized structures.[104] However, little is known about interactions with carbon surface defects.

In this work, results from UV-Photoelectron Spectroscopy (UPS) studies of C₆₀ molecules deposited on Highly Oriented Pyrolytic Graphite (HOPG) are presented. The influence of artificially created defects (by argon-ion irradiation) on fullerene-substrate interactions was investigated and temperature-induced C₆₀-desorption was examined on these disturbed HOPG surfaces.

The results show the fullerene-defect interaction is quite strong, leading to significant shifts and broadening of valence band features. These phenomena can be interpreted in terms of chemisorption at defect sites. Results obtained at room temperature are supported by temperature-induced desorption studies.

Experimental Details

The freshly-cleaved (in air) HOPG samples were inserted into the vacuum system (base pressure $< 1 \times 10^{-8}$ mbar) and annealed 1 h at ≈ 500 °C to remove contaminations from the surface. For the amorphous carbon sample a carbon layer (12 nm thickness) was magnetron-sputtered onto a silicon substrate from a graphite target. The HOPG substrate was irradiated with argon ions (3 kV kinetic energy) before fullerene deposition. The average ion flux was $5 \times 10^{11} \frac{1}{cm^2s}$, adding up to a total dose of $3 \times 10^{13} \frac{1}{cm^2}$ for 1 min irradiation.

Throughout the experiments, the fullerene deposition rate was kept constant (0.01 nm/s) with deviations less than 5%. This value corresponds to the deposition rate *on the carbon substrate*.¹⁴ During evaporation the samples were kept at room temperature. The samples were exposed to the fullerene beam for 1 min, resulting in a nominal deposited thickness of 0.6 nm.

Valence band spectra (He I, $h\nu = 21.2$ eV) have been acquired to identify the deposited fullerenes and to monitor desorption with increasing temperature. The sample holder allowed to heat the sample *in-situ* during measurement. A thermocouple touching the sample's surface was used to measure the temperature.

Results and Discussion

Fig. 3.29 shows valence band (He I) spectra of fullerenes on pristine and argon-irradiated HOPG and on amorphous carbon (a-C). The spectra are dominated by features stemming

¹⁴It was calculated by measuring the step profile of a thick fullerene film and dividing the thickness by the frequency shift of the quartz crystal monitor.

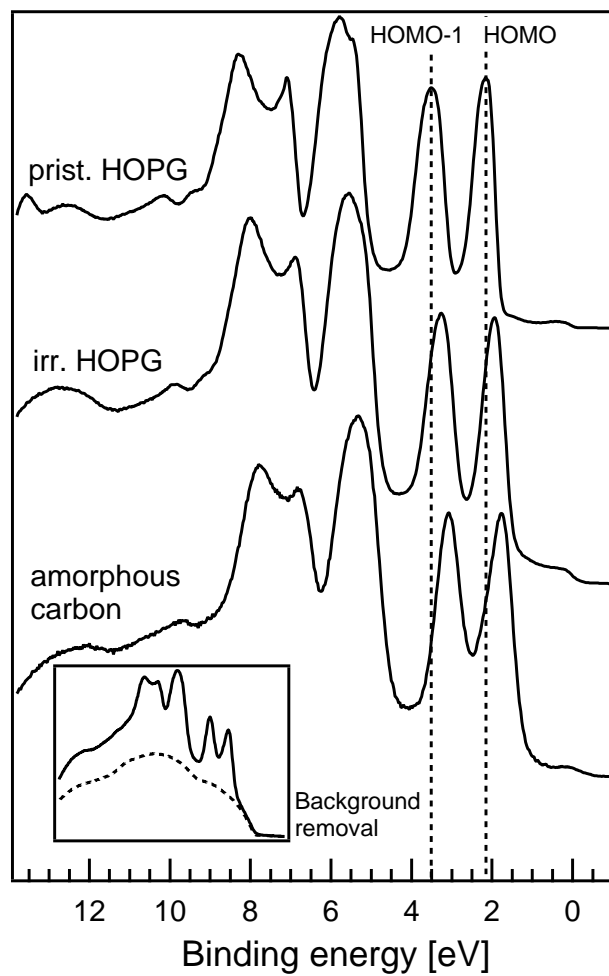


Figure 3.29: Valence band spectra of 0.6 nm C_{60} on carbon substrates. The negative BE shift and the broadening of spectra features for irradiated HOPG and amorphous carbon indicates strong fullerene-substrate interaction. Vertical dashed lines indicate HOMO (2.16 eV) and HOMO-1 (3.5 eV) positions on pristine HOPG. Inset: The dashed line shows the background spectrum of the amorphous carbon substrate, which was subtracted from the corresponding graph.

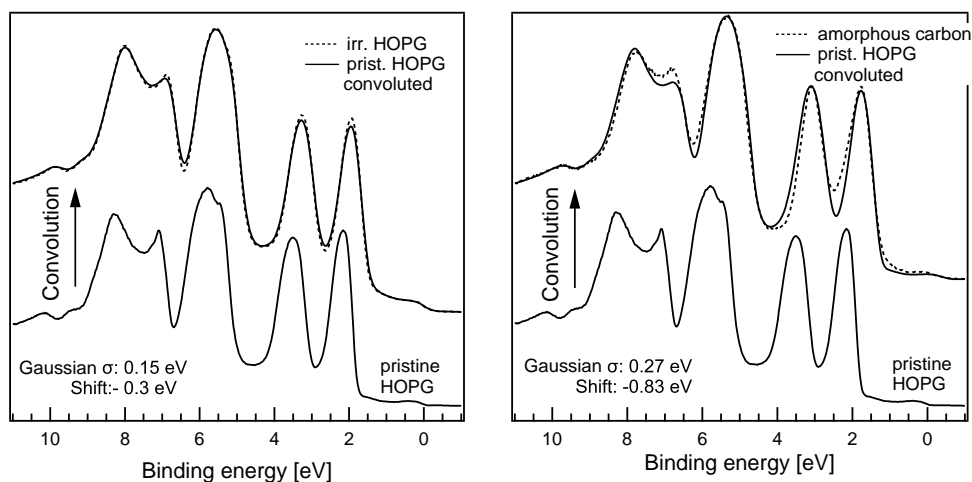


Figure 3.30: Simulation of fullerene VB spectra on defect-rich carbon surfaces: The reference spectrum (C_{60} on pristine HOPG) was convoluted with a Gaussian function and shifted to lower BE. Correlation with the corresponding experimental data is surprisingly good on irr. HOPG and still acceptable on a-C. The free parameters σ and Shift found by manual fitting.

from fullerene molecular orbitals.[105, 38, 106] The top curve (deposition on pristine HOPG) displays a typical C_{60} spectrum with a HOMO (Highest Occupied Molecular Orbital) lying at 2.16 eV. For argon-irradiated HOPG, a shift of the fullerene spectrum towards lower binding energies (BE) can be clearly observed. This effect is even stronger for fullerene deposition on a-C (bottommost curve). In this case the high substrate signal has been subtracted from the raw data (see inset). When comparing the valley between the HOMO and the HOMO-1 one observes a distinct reduction in depth for the a-C sample. These results (negative BE shift, reduced valley depth) are comparable to findings obtained from experiments on fullerene polymerization[106] and ion-induced fullerene cage damage.[107] It is unlikely that the fullerene cages break when in contact with the carbon surface. However, a strong C_{60} -substrate coupling must be responsible for the substantial spectral changes, maybe inducing cage distortion. Thus, we interpret our spectra as due to chemisorption of fullerenes at carbon surface defects resulting in distorted molecule structures. Depending on the nature of the defect its impact on the spectra (i.e., the negative shifts) may vary. A possible explanation for the distinct broadening of spectral features on irradiated HOPG and a-C would be loss of degeneracy in the molecular orbitals (MO)¹⁵ due to hybridization[108] or a distribution (in terms of coupling strength) of defect sites. This phenomenon should be most pronounced on the highly unordered a-C surface. This agrees well with the a-C spectrum in Fig. 3.29, as it exhibits the strongest shift and the largest broadening.

To test the above interpretation VB spectra for C_{60} on irr. HOPG and amorphous carbon were simulated by convoluting the spectrum on pristine HOPG with a Gaussian function and applying a negative BE shift. This is demonstrated in Fig. 3.30 with manually optimized values for σ and shift. The fullerene VB spectrum on irradiated HOPG (left) can be almost perfectly reproduced with a FWHM of 0.35 eV (2.35σ) and -0.3 eV shift. This is due to the resemblance of the two substrates. The spectrum for the a-C sample (right) cannot be fitted as well as the former, but the simulated curve still represents a fairly good approximation of the real data, using a Gaussian with FWHM 0.63 eV and a -0.83 eV shift. Spectral broadening by a Gaussian distribution (plus negative shift) is obviously not sufficient to model fullerene interaction with

¹⁵For example, the HOMO of C_{60} is a fivefold-degenerated MO with h_u symmetry.

the highly disordered a-C surface. A source of error could be the background removal applied to the a-C spectrum.

To study the stability of the chemisorbed species temperature-induced C_{60} desorption experiments were performed, accompanied by UPS measurements. A series of He I VB spectra was acquired as a function of the substrate temperature. The exceptional molecule-like C_{60} spectrum was used as a ‘fullerene fingerprint’ to monitor desorption behavior. Fig. 3.31 shows results for fullerenes (0.6 ML) on the different carbon substrates. The top graph ((a) pristine HOPG) shows complete desorption at a sharp threshold temperature (~ 203 °C). This is in good agreement with earlier works, however, the actual temperature is lower (40-60 °C) than reported in literature.[49, 109] This may be attributed to a systematic error in the temperature measurement (e.g., heat losses due thermocouple contact). Nevertheless, the complete removal is characteristic for physisorbed (by van-der-Waals forces), undamaged C_{60} . [110] The situation changes for deposition on irradiated HOPG (b): In agreement with (a) a sharp decrease of the fullerene fingerprint intensity can be observed, positioned at the temperature for physisorbed molecules (203 °C). However, the C_{60} signal does not completely disappear. It still dominates the spectrum above 203 °C, though slowly fading out above 360 °C. Fig. 3.31c demonstrates the results for a-C. The drop around 200 °C, observed on both HOPG samples, does not appear in the graph. The fullerene fingerprint intensity decreases slightly with increasing temperature. It is an interesting fact that the VB spectra exhibit a positive BE shift between 23 °C and 43 °C. It could be successfully reproduced in another identical experiment. Charging effects which may cause such shifts can be ruled out as the UV-source was already operating several minutes before starting the desorption experiment and during this time the VB spectrum in Fig. 3.29 (bottommost curve) was measured. In an earlier desorption experiment (no exact temperature measurement, but otherwise identical parameters) this shift was observed as well. The shift can rather be interpreted as due to structural changes of the carbon surface. One could speculate that the distribution of adsorption energies changes and therefore directly influences the measured VB spectra

To directly compare the three desorption experiments, the intensities of the fullerene fingerprints have been plotten as a function of the temperature, as shown in Fig. 3.31d. The temperature range expected for physisorbed C_{60} (as observed on pristine HOPG) is indicated by the rectangle. The curve corresponding to irradiated HOPG shows a sharp drop in intensity (to 60% of the original value), located within the marked region. This indicates removal of physisorbed fullerene species, in agreement with the prisitine HOPG sample. For higher temperatures there is a continuing, but slow, further decrease. The observation of two different desorption regimes can be readily explained by the degree of HOPG surface disorder. Comparing the total argon ion flux applied during sample preparation ($3 \times 10^{13} \frac{1}{cm^2}$) with the number of surface atoms for HOPG ($4 \times 10^{15} \frac{1}{cm^2}$) it is reasonable to assume a surface only partly damaged by ion impact. Hence, some fraction of fullerenes adsorb on pristine surfaces (physisorption) and some fraction chemisorbs at defect sites.

He I VB spectra taken at the end of the desorption experiments are presented in Fig. 3.32. Comparison with clean substrates (dashed lines) confirm the complete fullerene removal for the pristine HOPG sample (the substrate’s spectral features clearly visible) and spectra still dominated by fullerene features for irr. HOPG and a-C. The latter ones are heavily broadened compared to the corresponding as-prepared spectra. Heating up the irradiated HOPG above 500 °C (spectrum not shown) did not remove the remaining fullerene molecules, only a slight smoothing of the fullerene features were observable.

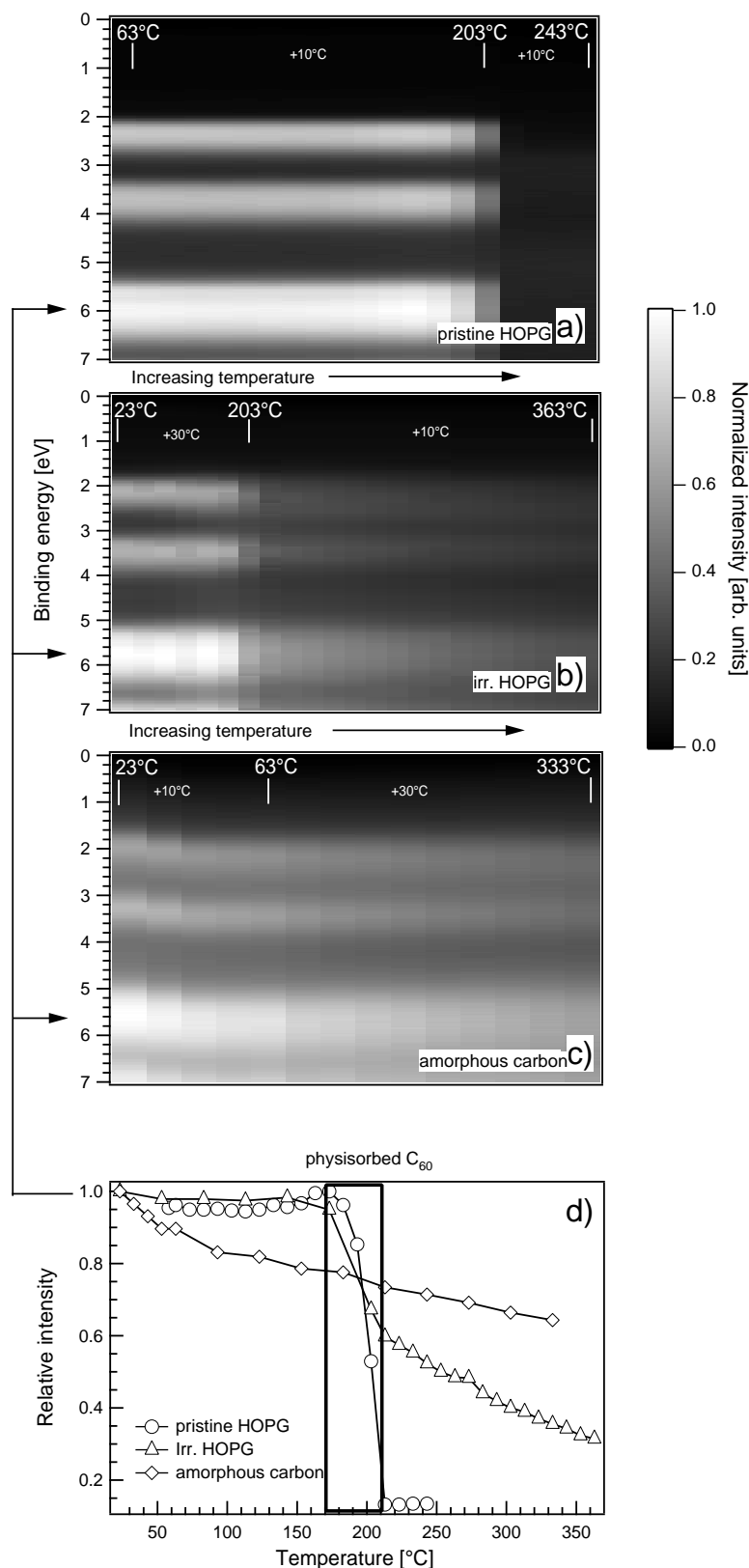


Figure 3.31: (a)-(c): Fullerene desorption graphs as a function of the sample temperature for 0.6 ML on pristine HOPG, argon-ion irradiated HOPG and amorphous carbon. Bright features are characteristic VB 'fingerprints' for C₆₀ molecules. Small numbers indicate temperature steps between measurements. (d): Relative C₆₀ intensities as a function of the temperature. Data points taken at the positions of the strongest fullerene peak (arrows). Temperature range for physisorption is indicated by a rectangle.

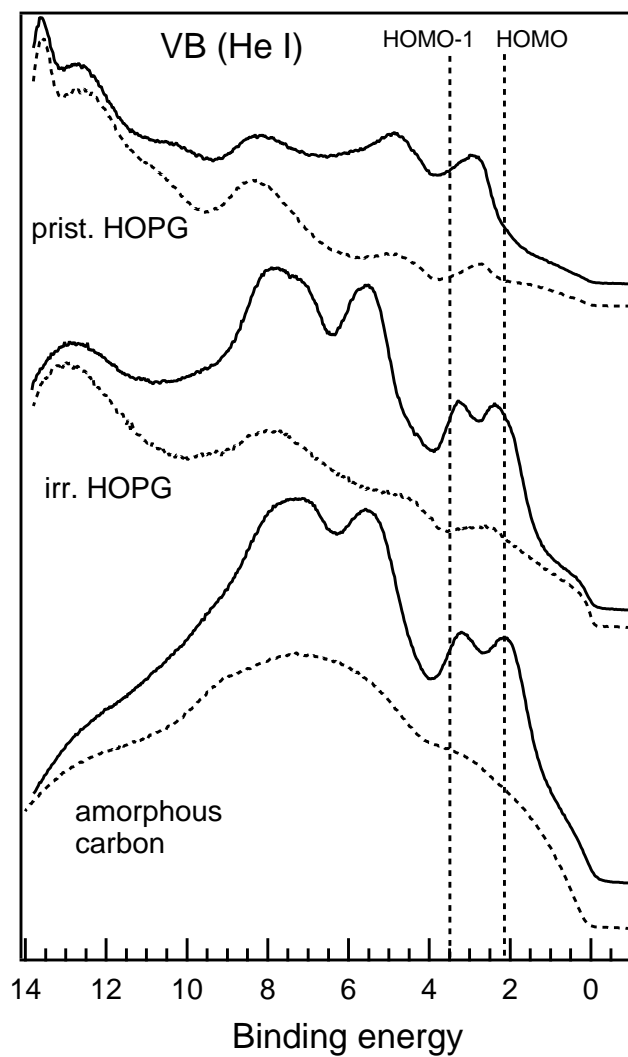


Figure 3.32: VB spectra taken after fullerene desorption: Complete desorption from pristine HOPG, VB spectrum exhibits typical HOPG features. Incomplete desorption on irr. HOPG and amorphous carbon, (modified) fullerene spectral features still visible. The dashed curves correspond to VB spectra of the original substrates

Conclusions

We investigated temperature-induced desorption of C_{60} molecule submonolayers deposited on pristine HOPG, argon-ion irradiated (3 keV) HOPG and amorphous carbon. By means of UV-Photoelectron Spectroscopy (He I) we monitored C_{60} VB features as a function of the sample temperature. As expected, complete fullerene desorption (in a narrow temperature range around 200 °C) could be achieved on pristine HOPG, indicated by the appearance of a characteristic HOPG VB spectrum. The threshold temperature was in agreement (within systematical errors) with literature. On argon-ion irradiated HOPG two different desorption behaviors were identified: a sharp drop in spectral intensity in the same temperature range as on pristine HOPG and a following slow decrease for higher temperature. On amorphous carbon only a slow decrease of intensity can be observed. In both cases desorption was not complete, VB spectra clearly showed C_{60} features even for 360 °C temperature. We interpret such retarded desorption as due to stronger chemisorption at surface defect sites. For irradiated HOPG a certain surface fraction remains undamaged, reflected by two kinds of desorption behavior. On amorphous carbon, however, the surface is completely disordered with a vast variety of adsorption sites. The results for irradiated HOPG is remarkable as it provides a way of controlled surface nanostructuring. One could imagine an ordered arrangement of defect sites created by Focused Ion Beam on HOPG. Sublimation of fullerenes on the heated substrate (right above the desorption threshold on pristine HOPG) should promote chemisorption preferentially on defects, thus, decorating them with C_{60} molecules.

3.3.2 Comments on Deposition Methods

It is known that fullerene cages can be damaged or even destroyed by electron irradiation. The geometrical design of the e-beam evaporator used in this study principally enables electrons being accelerated to the crucible to hit evaporated fullerene molecules. The deposition of damaged molecules would have large impact on the results obtained earlier. Although this was a rather unlikely scenario¹⁶ a study was performed to compare fullerene films deposited with an e-beam evaporator and a button heater sublimation source (described in 2.1.1) and thus, to substantiate the above experimental results.

In a first experiment fullerenes were deposited on pristine HOPG: a freshly cleaved HOPG substrate was introduced into the vacuum system and annealed for 1 hour at 500 °C. Fullerenes (≈ 0.6 ML) were deposited with the e-beam source and a valence band spectrum was measured. The HOPG was cleaned afterwards by desorbing the C_{60} . The successful complete removal was confirmed by UPS. Next, fullerenes were deposited on the cooled substrate using the sublimation source. Fig. 3.33 shows the superposition of the two fullerene (top) and HOPG (bottom) spectra. It is quite remarkable how the two spectra fit to each other, indicating that perfectly healthy fullerene molecules have been deposited in both cases.

In the next experiment fullerenes were deposited on irradiated HOPG. The results for He I UPS spectra are shown in Fig. 3.34 a for different C_{60} thicknesses. VB spectra of identical fullerene coverages deposited from the Omicron and from the sublimation source are superposed and normalized with respect the HOMO peak intensity. The correlation between each two curves quite well for 0.6 nm thickness and nearly perfect for higher coverages. With increasing film thickness the spectra slightly shift to higher binding energy. This is due a change in chemical environment that is experienced by the molecules: For low coverages most of the C_{60} are in contact with the defect-rich HOPG surface. For higher coverages fullerenes are deposited

¹⁶It was shown above that fullerenes deposited on pristine HOPG completely desorbed from the surface, which is a good indication of unharmed molecules.

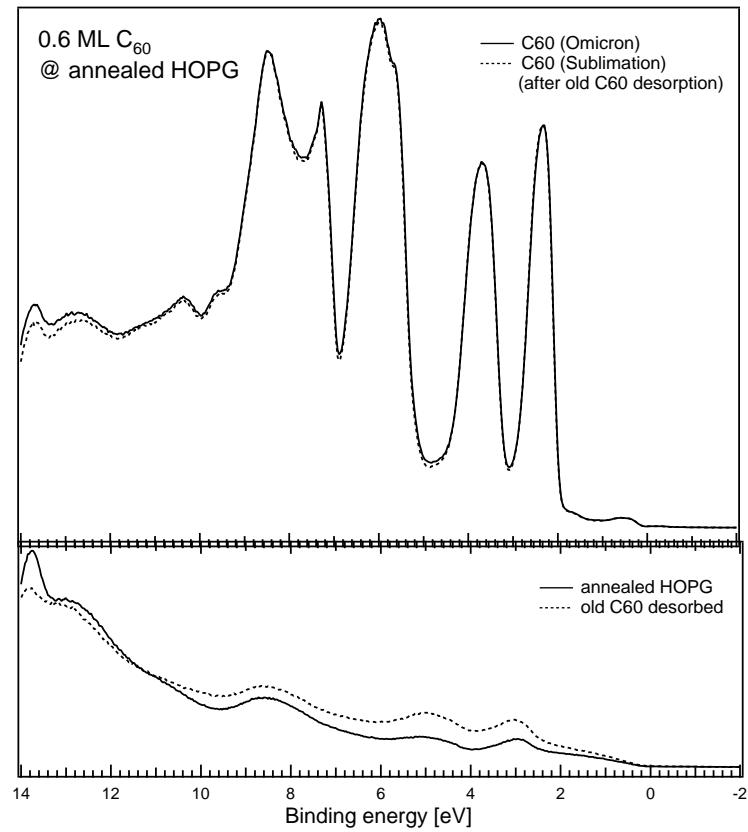


Figure 3.33: Comparison of C_{60} VB spectra for the Omikron and the sublimation source. The fullerene spectra have been normalized to equal height.

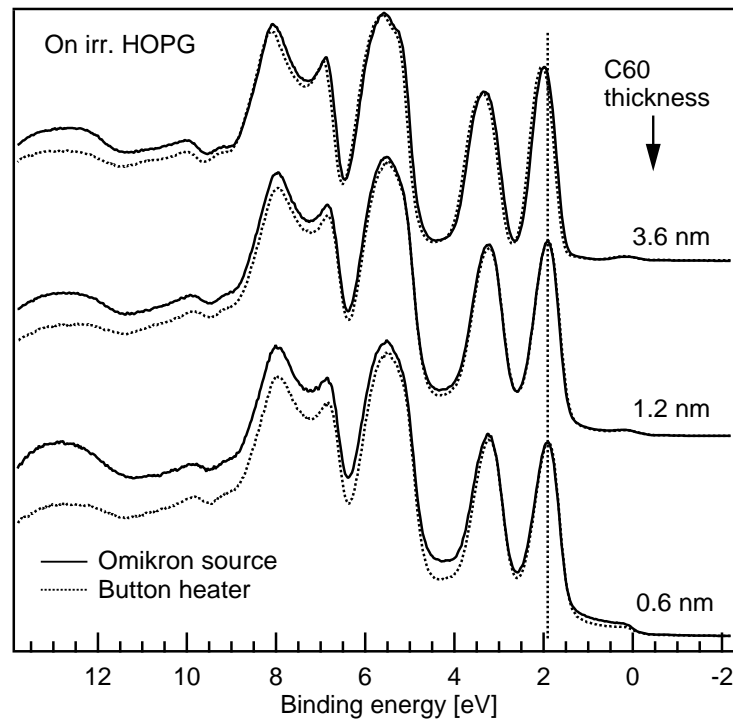


Figure 3.34: Comparison of VB spectra for fullerene deposited with e-beam and sublimation source, respectively, as a function of the thickness.

on fullerenes.

As expected, these findings confirm that the choice of the deposition method had no influence on the experimental results presented in 3.3.1.

3.4 Summary of Main Results

Photoelectron spectroscopy (MXPS) studies on chemically synthesized thiol-passivated gold nanoparticles revealed a thiol-chain length dependence on the thermal desorption behavior of the passivating shell, on particle self-assembly properties and on X-ray induced thiol-gold bond breaking. Observed changes in the Au 4f core-level binding energies motivated to study thiol-gold interaction in more detail. Adsorption of thiol molecules on gold clusters should yield insight to the nature of the still not fully understood Au-S bond. To avoid exposure to ambient atmosphere cluster deposition and thiol adsorption had to be performed *in vacuo*. Therefore, the growth of clusters on defect-rich carbon surfaces by means of metal evaporation was studied at first.

Investigation of the early stages of cluster nucleation and growth showed a considerable interaction of deposited gold clusters with carbon defects, heavily shifted (≈ 1 eV) second feature in the Au 4f core-level spectra. This was attributed to the existence of a bimodal cluster size distribution. It was found that deposition of heated substrates (400-600 °C) represent a possibility to preferentially grow nanoparticles on defect-sites.

Having studied nanoparticle growth gold cluster samples were prepared to be exposed to a thiol atmosphere. MXPS spectra were taken before and after exposure to monitor changes in the clusters' electronic configuration. It could be shown that thiol adsorption induces positive binding energy shift in gold core-level and valence band spectra. This was interpreted as due to electron charge localization by Au-S bonds. Changes in the shape of MXPS valence band spectra where attributed to re-hybridization of Au 5d electrons (creation of Au-S bonds) and a close examination of the Fermi edge region hinted to a thiol-induced metal-to-insulator transition. These results are of high interest concerning the electrical properties of metal-organic contacts.

Motivated by the results obtained from cluster deposition on defect-rich carbon surfaces the work was extended to buckminsterfullerene molecules. The interaction of C₆₀ with defects and the thermal stability was investigated by means of UV Photoemission Spectroscopy (UPS). It was demonstrated that fullerenes chemisorb at defects indicated by a higher desorption temperature as on pristine HOPG. This was reflected by significantly shifted and broadened VB features. The higher desorption temperature for C₆₀ attached to defects than for species adsorbed on undamaged HOPG might allow in combination with Focused Ion Beam techniques to prepare fullerene-decorated nanostructures.

In conclusion, the different experiments and results presented here have shown that artificially created defects on carbon (esp. HOPG) substrates might be promising way of surface nanostructuring. The choice of carbon is interesting with regard to applications where biocompatibility¹⁷ of the substrates is demanded.

¹⁷This means materials that are not expected to be harmful or toxic to biological samples, e.g., cells or tissue

Appendix A

Supplementary Information

A.1 Photoelectron Spectroscopy in the Historical Context

This section shall give a short historical overview about the early beginnings and the evolution of (X-ray) Photoemission Spectroscopy.¹ Fig. A.1 illustrates the setup Heinrich Hertz used for his experiments in 1887.[112] He used a driving arc (d) to trigger a secondary arc (f), both attached to induction coils (c,d) supplied by a battery (b) He observed that despite a shielding material (p) put between the two arcs, the secondary arc could be triggered by the driving arc. He concluded that ultraviolet radiation emitted from the driving arc was the origin of the observed sparks as the second arc. His findings caught the attention of Wilhelm Hallwachs, who improved Hertz' experiments by replacing the arc for a continuous UV light source. He found evidence that electrons (photoelectrons) are emitted from an irradiated metal plate.[113]. Between 1900 and 1902 Philipp Lenard published his works on photoelectrons in a retarding potential.[114, 115] His observations summarize the most significant characteristics of the so-called *photoeffect*:

- The photoelectron velocity is not dependent on the intensity of irradiation
- The rate of emitted electrons is proportional to the light intensity
- The electron velocity depends on the frequency of the light

In 1905 Lenard received the Noble Prize for his studies on cathode rays. The explanation of his findings, however, proved to be a difficult task at that time. It was Albert Einstein's interest in the nature of light radiation that illuminated the problem and led to the famous publication in Einstein's 'annus mirabilis' 1905: *Über einen die Erzeugung und Verwandlung des Lichtes betreffenden heuristischen Gesichtspunkt*. [116] As the acceptance of a quantum of light was such a radical thought it was not until 1921 that his work was finally honored by the award of the Nobel Prize.

In the following years the photoeffect was more extensively studied and laboratory equipment developed and improved. On the theoretical side quantum theory was refined and added a huge amount to explain the photoelectrical effect. The modern era of Photoemission Spectroscopy began in the 1950s with the important experimental works of Steinhardt and Serfass,[117] who proposed XPS as a useful tool for elemental quantification and already used an electrostatic analyzer for their measurements. At this time Kai Siegbahn and his group at the

¹A very good review especially focussing on the first half of the 20th century can be found in Ref. [111].

H. Hertz experiment, 1887

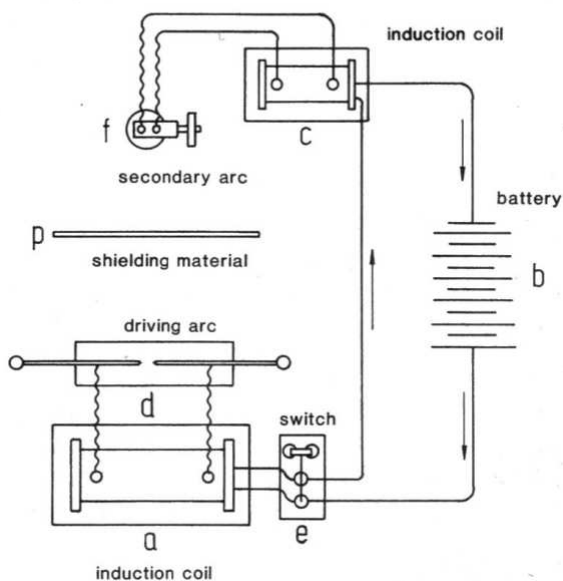


Figure A.1: Experimental setup used by Heinrich Hertz for the discovery of the photoelectric effect.[53]

University of Uppsala in Sweden were also working on X-ray photoemission. They developed a very high-resolution spectrometer and obtained excellent spectra from various solids (e.g., first high-resolution XPS spectra of MgO.[118]) and gases during the years. Their data served as standard references for many years.[119, 120, 121] Probably the most important discovery of Siegbahn, however, was the sensitivity of photoemission for the chemical environment of the emitting atom, leading to the well-known *chemical shift* of core-level spectra.[122] Combined with the elemental sensitivity these features outlined the new analytical method that Siegbahn named “electron spectroscopy for chemical analysis” (ESCA). Kai Siegbahn received the Nobel Prize in 1981, jointly with Nicolaas Bloembergen and Arthur Schawlow for their achievements in laser and electron spectroscopy.

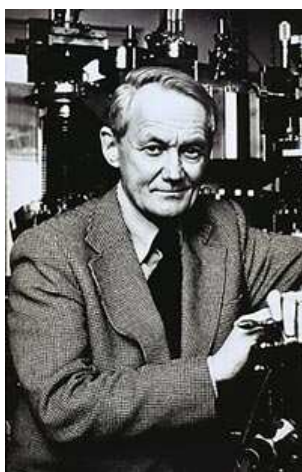


Figure A.2: Kai Manne Börje Siegbahn (*1918)

A.2 Evaporation of Metals on Surfaces

One of the simplest methods to grow metal particles on substrate surfaces is the evaporation of bulk material and initiation of cluster growth through condensation from the metal vapor phase. This allows to prepare particles *in-vacuo* without the need of exposing the samples to atmosphere. Another advantage is the use of a evaporation source (e.g. thermal or e-beam evaporator) which is usually easy to handle and small in size. Although this method has been used

already in the earliest studies of thin films / clusters on surfaces, it bears the disadvantage of poor control over nucleation and growth of particles. As cluster growth is highly sensitive to individual properties of the substrate and the evaporated material, the choice of suitable ‘partners’ is crucial. Adatom-substrate interactions strongly influence adsorption and diffusion mechanisms and thus have impact on submonolayer / particle growth. Possible surface processes are depicted in Fig. A.3 together with characteristic energies E_x . Depending on the actual system under investigation, some of the presented mechanism may preponderate and therefore governing the film nucleation and growth. On the other hand, when dealing with computational simulations, simplifications have to be applied to render the underlying equations manageable and to account for calculatory limits.

For the following discussion the book *Introduction to Surface and Thin Film Processes* by Venables [123] was used as secondary literature.

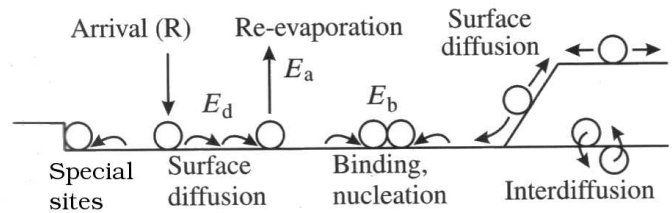


Figure A.3: Thin film growth by evaporation: Surface processes and characteristic energies.[123]

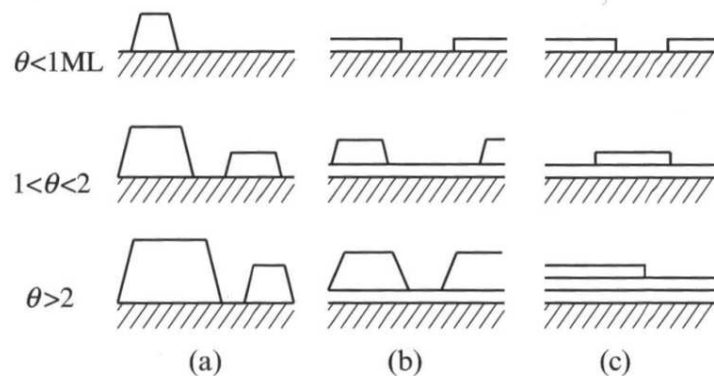


Figure A.4: The three growth modes of epitaxial film growth: (a) Volmer-Weber, (b) Stranski-Krastanov, (c) Frank-van der Merwe[123]

A.2.1 Classical Treatment of Thin Film Growth Processes

The process of thin film growth can be divided into three different growth modes. They are illustrated in Fig. A.4 and were systematically described in 1958 by Bauer.[124]

Volmer-Weber (a) Film growth proceeds by forming of islands on the substrate. This is due to a higher cohesive energy among the deposit that with the substrate.

Stranski-Krastanov (b) This somehow intermediate growth mode incorporates layer-by-layer growth, which switches over to island growth at later time

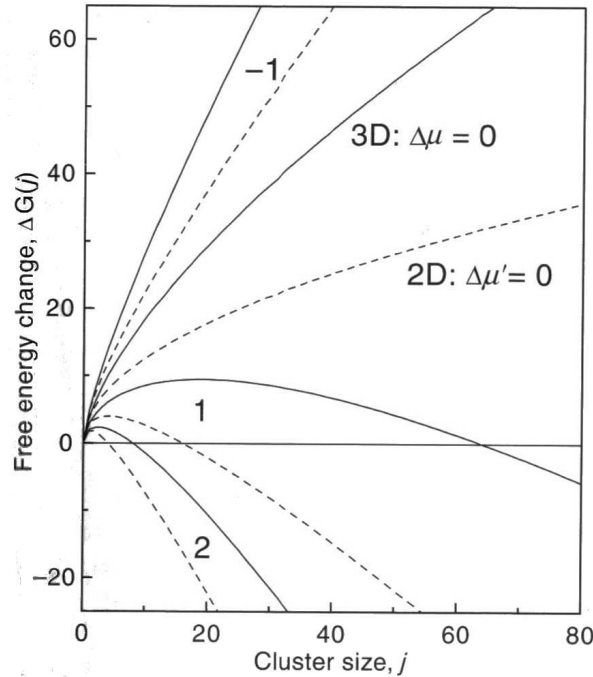


Figure A.5: Nucleation free energy (in arbitrary units) as a function of the 2D/3D cluster size: The curve maximum defines the critical size under which clusters are not stable. The position (or existence) of a maximum is dependent on the cluster's chemical potential $\Delta\mu$.

Frank-van der Merwe (c) This mode is also called *layer-by-layer* growth, because the film builds up by successive coverage of (more or less) complete monolayers. In this case, the deposited atoms are more strongly bound to the substrate than to each other.

The different growth modes can also be understood in terms of chemical potential of the deposit with respect to the bulk material value. In the case of *Volmer-Weber*, even for less than one monolayer (ML) the potential exceeds the bulk value. This means, to minimize the energy, the deposit tends to minimize the contact area with the substrate, leading to island growth. For *layer-by-layer* growth, the chemical potential only slowly approaches the bulk value with increasing number of layers. Therefore, there is no need to minimize the contact area. A nucleation barrier exists for *Stranski-Krastanov* growth, at which the chemical potential exceeds the bulk value only after a few deposited monolayers.

Proceeding with the classical thermodynamic treatment of thin film growth, the term *critical cluster size* shall be introduced in the following. In the case of isolated cluster growth (Volmer-Weber) one can calculate a free energy difference $\Delta G(j)$,² taking into account the surface free energy X and the chemical potential $\Delta\mu$.³ One then finds

$$\Delta G(j) = -j\Delta\mu + j^{2/3}X.$$

A plot of $\Delta G(j)$ as a function of the cluster size j is shown in Fig. A.5 for different $\Delta\mu$ and for 2D/3D clusters. A positive slope at a chosen position (cluster size) on the curves indicates that augmenting the number of atoms results in a higher free energy, and thus will be avoided by the system. The curves for $\Delta\mu > 1$ show a maximum after which the slope turn negative. Hence, there exists a cluster size i , determined by the position of the maximum, under which the particles are not stable and tend to dissolve fast. i is usually called the *critical cluster size*.

² $\Delta G(j) = 0$ for clusters containing no atoms ($j=0$) and for the bulk material in equilibrium with the vapor

³with respect to the bulk value

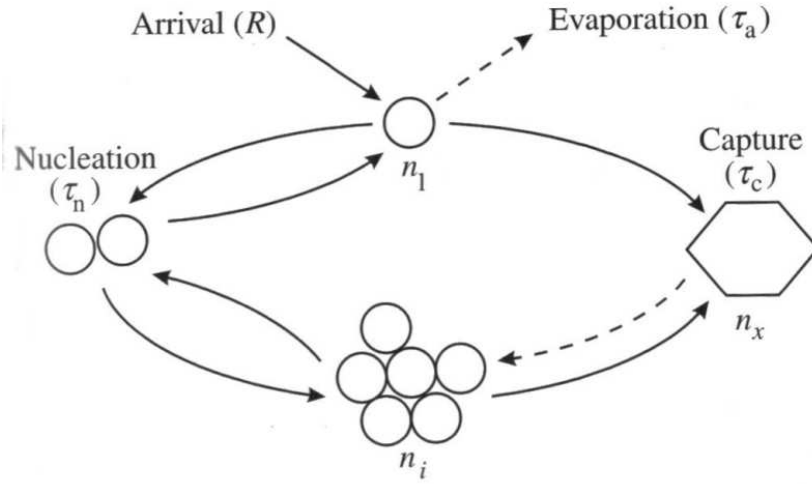


Figure A.6: Surface processes on the atomic level

If we take a look at the situation on the atomic level (Fig. A.6), several processes occur that have influence on film growth and in general only a few of them can be taken into consideration for quantitative calculations. If only monomers are mobile on the surface the rate equations describing the time derivative of the surface density n_j of j -clusters⁴ have the form

$$\frac{dn_1}{dt} = R - \frac{n_1}{\tau_a} - 2U_1 - \sum U_j$$

and

$$\frac{dn_j}{dt} = U_{j-1} - U_j$$

for larger clusters ($j \geq 2$). U_j is the adatom capture rate for a j -cluster. The *critical cluster size* (i) is simply defined as follows: All clusters $> i$ are stable, i.e., adatoms are captured (in average) before the particle decays. The stable cluster density n_x is described by the coresponding rate equation

$$\frac{dn_x}{dt} = \sum_{j \geq i} (U_j - U_{j+1}) = U_i.$$

Without giving the details, one can find the *Walton relation*

$$n_j = (n_1)^j \sum_m C(m) \exp\left(\frac{E_j(m)}{kT}\right)$$

giving the equilibrium constant for a j -cluster in local equilibrium. (m) denotes the m th configuration of the cluster. $C(m)$ is a statistical weight for a particular size and E_j is the binding energy difference between j and $j - 1$ cluster. In the next step, the rate equations can be simplified to

$$\frac{dn_1}{dt} = R - \frac{n_1}{\tau_a} - (2U_1 + \sum_{j < i} U_j) - \sigma_x D n_1 n_x$$

and

$$\frac{dn_x}{dt} = \sigma_i D n_1 n_i - U_{cl}.$$

with the so-called capture number σ

⁴This means clusters consisting of j atoms.

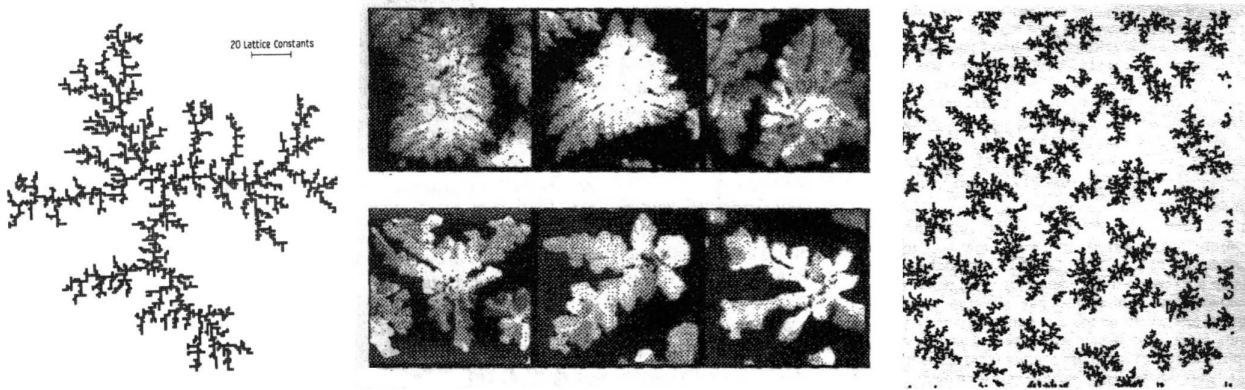


Figure A.7: Comparison of theoretical model and experimental data. *Left:* Aggregation of particles obtained from simulation with DLA algorithm. *Middle:* SEM image of Au submonolayer evaporated on HOPG. *Right:* Simulated structure of mobile clusters on a surface.[126, 127, 128]

A.2.2 Computational Simulations

As adatom-substrate interactions and diffusion processes take both part in the dynamic process of particle nucleation and growth and are difficult to deal with, mathematical methods and algorithms have been developed over the years. Using statistical computer codes (e.g. Monte Carlo methods) and simplifying the sequence of deposition, diffusion and aggregation to a few rules, the growth and morphology of deposited submonolayers can be simulated for simple systems.

A very successful approach is called *Diffusion-limited Aggregation* (DLA), which was developed by Witten and Sanders. [125, 126] DLA can be applied in many fields of science where aggregation of small particles takes place (e.g crystal growth, coagulation of aerosols, precipitation from a supersaturated matrix). The factor that is limiting the speed of the ‘reaction’ is the diffusion material towards the ‘reaction spot’. For the 2D case the model consists of particles moving over a lattice. The rules governing particle aggregation are as follows:

- A seed particle is placed at the origin of the lattice
- A second particle is placed somewhere on the grid and performs a random walk (i.e., diffusion)
- The moving particle stops as soon as it arrives at a lattice site adjacent to a occupied one

This procedure has to be applied to many particles with randomly chosen starting points on the lattice. The resulting structure is remarkably complex despite the simple rules (Fig. A.7 left).

The interaction of noble metals with Highly Oriented Pyrolytic Graphite (HOPG) surfaces is mainly limited to weak van-der-Waals forces, resulting in a high diffusion coefficient. For these systems cluster growth (at room temperature) can be well described by the above mentioned DLA model. With increasing metal coverage highly ramified structures emerge.[127, 129] There is a strong resemblance between the experimental and simulated structure (compare left and middle image in Fig. A.7) despite the simple DLA model.

Similar structures are obtained if metal *clusters* are deposited, which indicates that under certain conditions clusters may exhibit a comparable high surface mobility.[128, 130] This is explained by a lattice mismatch between cluster and graphite surface resulting in a smaller diffusion activation energy. Computer codes called *Kinetic Monte Carlo Simulations* can successfully be applied to model submonolayer growth by cluster deposition, leading to similar

ramified structures as in the case of atomic deposition (Fig.A.7). See Ref. [128] for a review of this topic.

Diffusion-limited processes are very sensitive to the substrate temperature, as $D = D_0 \exp \frac{-E_d}{kT}$. For example, the cluster density is expected to decrease dramatically when going to higher temperatures. This fact can be used to determine the nature of nucleation, i.e. homogeneous (absence of surface defects) or heterogeneous nucleation (presence of surface defects). Most substrates exhibit some kind of surface defects, which influence the nucleation process and lead to deviations from DLA. Even well-prepared HOPG can not be regarded as completely defect-free, as there are at least step edges that may serve as nucleation sites. For low defect densities⁵ the effect is small, but for a high defect density surface diffusion and nucleation is seriously affected. Nucleation takes place mainly at defect sites and the density of cluster seeds is governed by the defect density.[131]

⁵An exact value cannot be given. The terms ‘high’ and ‘low’ defect density has to be understood with regard to the particle nucleation density on the *defect-free* substrate.

A.3 Towards Thiol-Passivated Nanoparticles

Introduction

The chemical synthesis of nanoparticles has developed fast over the years and a lot of work is currently done to optimize existing methods to find new approaches. What makes the different chemical routes so appealing is the fact that they provide macroscopic amounts of material, which is desired for large scale applications. Synthesized particles can be coated by a variety of molecules (with functional groups to gain some sort of chemical selectivity). In the following section some of the most common chemical methods will be presented to give the reader an introduction into the topic (with focus on gold nanoparticles, though).

A simple and very often used preparation method is called *Citrate Reduction* and was introduced by Turkevitch in 1951.[132] Starting with an aqueous solution of a metal salt (e.g. HAuCl_4 , AgNO_3 , H_2PdCl_4 , H_2PtCl_6) adding sodium citrate ($\text{Na}_3\text{C}_6\text{H}_5\text{O}_7$) to the solution leads to reduction of Au^{III} species to form colloidal particles of diameters > 16 nm. By changing the ratio of the reducing/stabilizing agent, the mean diameter can be controlled.[133] The preparation method is simple but the obtained particles are prevented against aggregation only by an electric double layer surrounding each particle. High purity of the solution is therefore a requirement for successful particle synthesis.⁶ Further control over particle sizes has become available with the *seed-growth method*. [134, 135] Starting with a small colloid (e.g 18 nm, a size easily obtainable with the citrate reduction method) in solution, one adds additional gold salt together with hydroxylammonium chloride as reducing agent. The colloidal particles act as seeds for further growth. This method has the advantage of increasing the mean particle size without significantly enlarging the size distribution.

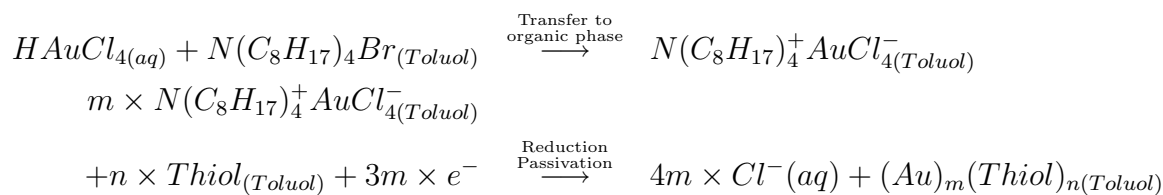
Pioneering work in the field of nanoparticle preparation has been done by Schmid and coworkers.[136, 137, 138, 139] They developed a chemical route to synthesize phosphine-passivated clusters.[140] Their gold cluster compound $[\text{Au}_{55}(\text{PPh}_3)_{12}\text{Cl}_6]$ exhibited a uniquely narrow size distribution (1.4 ± 0.4 nm) and has proven to be well suited and therefore extensively employed for studies on quantum-dot materials. With the same method, passivated Rh, Ru, and Pt clusters can be obtained as well. A cluster consisting of 55 atoms belongs to the species of *Closed Shell Particles*, indicating completely filled layer of dense-packed atoms around a central atom and should not be confused with electronic shells around nuclei. The smallest cluster is one atom surrounded by 12 neighbors (first closed shell), thus, 13 atoms. The number Z of atoms in the n th closed shell can be calculated from $Z = 10n^2 + 2$. [141] Therefore, $n = 2$ for $13 + 42 = 55$ atoms.

The Brust-Shiffrin Method

The passivation of gold nanoparticles with alkanethiols was first reported by Mulvaney and Giersing[142] and became popular after a facile synthesis method was published in 1994 by Brust et al.[28] It allowed for the first time to produce nanoparticles with controllable size and small size distribution, *and* which were very stable against temperature and ambient conditions. They could be dissolved in organic solvents several times without traces of aggregation. In a few words, the Brust-Shiffrin method is a two-phase procedure, during which dissolved AuCl^- is transferred from an aqueous to an organic phase by means of tetraoctylammonium bromide as the phase-transfer agent. Gold is reduced to Au^0 by NaBH_4 , and nanoparticles are formed. Alkanethiols form a protecting monolayer around the growing gold cores, thus preventing further growth. The obtained colloidal particles are often called *monolayer-protected clusters* (MPC).

⁶Impurities might interfere with the double layer and lead to particle aggregation.

The two steps can be written as follows:



The Brust-Shiffrin method became increasingly popular and has been optimized and varied to extent the variety of nanoparticles by many researchers. For example, Murray et al. succeeded in exchanging a fraction of the thiol ligands (*place exchange*) with various functionalized molecules.[143] The monolayer-protected particles used in this work have been synthesized following the chemical procedure of Murray, based on the Brust method.[27] It will be shortly described in the following (for details, see Ref. [98]):

A solution (in toluene) of tetraoctylammonium bromide was added to aqueous $HAuCl_4 \cdot xH_2O$. $AuCl_4^-$ ions were transferred into the organic phase. The organic phase was separated and thiols (according to the desired chain length) were added. The solution was cooled to $0^\circ C$ and $NaBH_4$ (reducing agent) slowly added. Gold clusters formed, as witnessed by the color change of the solution from red to black. Toluene was exchanged with ethanol and after complete precipitation, the colloids were collected in a filtration frit and dried. Purity of the colloid powder was determined by the absence of resonance due to free alkanethiol in the 1H -NMR spectrum($CDCl_3$), in particular the α - CH_2 resonance at 2.5 ppm.

Although some particle features can be measured when they are still dispersed in the solvent (e.g., optical spectra), in many cases it is necessary to prepare them on some kind of substrate. There are several methods commonly used in sample preparation of which some exploit the particles' ability to self-assemble into dense and often ordered structures.[67, 32] Shell-shell interactions play the governing role in such mechanisms, thus the process of self-organization can be influence (within limits) by choice of passivating molecule. The inter-particle distance d , for example, can be controlled by the length of the thiol molecule. The number of atoms in a thiol's carbohydrate chain can be easily varied. It has been found that the molecules of adjacent particles interdigitate (see. Fig. A.8), thus yielding a inter-particle distance of less than twice the chain length, indeed rather being close to one.[66] The dependence of the inter-particle gap on the thiol length has been investigated in a recent publication.[144] The gap distance could be varied between 1.4 and 2.4 nm for thiol chains with 6 and 14 carbon atoms, respectively. The increase in gap distance was found to be 1.2 Å per carbon atom.

A.3.1 Sample Preparation Techniques

The Langmuir-Blodgett Method

The basic idea behind this technique is to spread nanoparticles on the surface of a liquid (liquid-gas interface), followed by a reduction of the surface area in order to densify them. This is done by applying a controlled force to a movable barrier, thus reducing the available surface area. The optimal barrier position in order to obtain a dense monolayer can be determined by monitoring the surface pressure, which is proportional to the force applied to the barrier. Fig. A.9 qualitatively shows how the structure of the particle layer can be influence by moving the barrier. The transition from one 'phase' to the other is reflected by a distinct change in surface pressure. The prepared monolayer can be transferred to onto a substrate by slowly moving the sample through the layer and thus collecting the molecules in the sample.

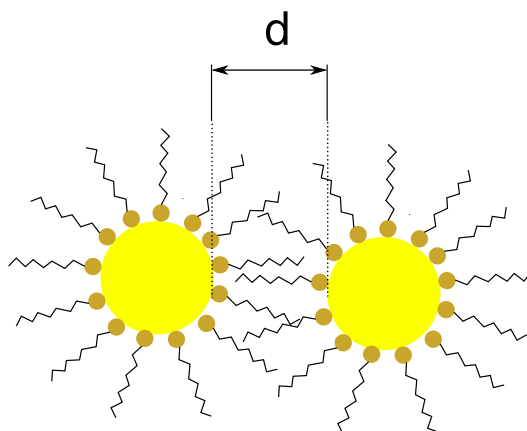


Figure A.8: Control of inter-particle distance: When thiol-passivated particles are arranged in a dense film, the organic chains interdigitate. Inter-particle distance d is roughly the length of one thiol chain.

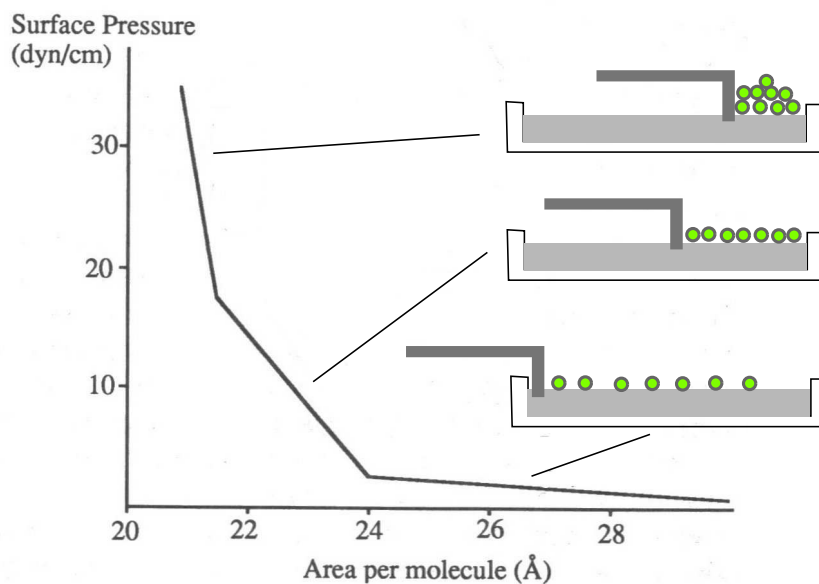


Figure A.9: Langmuir-Blodgett method: By reducing the area available to the particles dense monolayers or multilayers can be achieved. (Partly taken from [145])

Spin Coating

For spin coating preparation a drop of dissolved nanoparticles is put on top of a fast-spinning substrate.⁷ The drop expands all over the substrate and leaves behind the dispersed particles after the solvent has evaporated. This is a very fast process where the dissolved particles do not have much time to arrange orderly, lead to randomly distributed particles.

Dip Coating

This is a commonly used method to prepare self-assembled monolayers on substrates. It is especially suited for colloidal nanoparticles as they do not need to have a spacial orientation to form organized monolayers. Similar to the LB-method the sample is slowly taken moved out of the liquid, however, the monolayer forms at the meniscus through capillary forces of the evaporation solvent. The retracting speed and the particle concentration can be varied to optimize film growth.

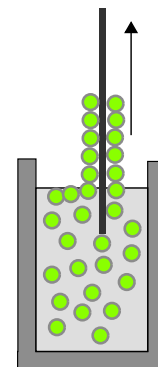


Figure A.10:
Dip coating

Drop Deposition

This method also exploits the self-assemble mechanism of colloidal particles. To prepare a sample it is sufficient to deposit a small drop of dissolved colloids onto the substrate and to let the solvent evaporate. It could be shown that it is possible to influence the colloid layer morphology by leaving the so-prepared sample in solvent-saturated atmosphere. Depending on the exposure time 1-3 dimensional arrangements can be achieved.[32]

Plasma Etching

After having prepared a well-ordered structure it may be desirable to get rid of the organic components surrounding the clusters in order to apply analytical methods on naked clusters. A procedure which has already successfully performed is the exposure to a plasma (e.g., hydrogen, oxygen) environment. This is called plasma etching and allows to completely remove organic molecules from the sample. As the etching process is done in a vacuum chamber naked particles can be prepared and measured in an in-vacuo experiment. The exact parameters for this technique have to be adjusted according to individual needs. It has been shown that etching the organic shell does not influence the ordered structure obtained by means of particle self-assembly.[83]

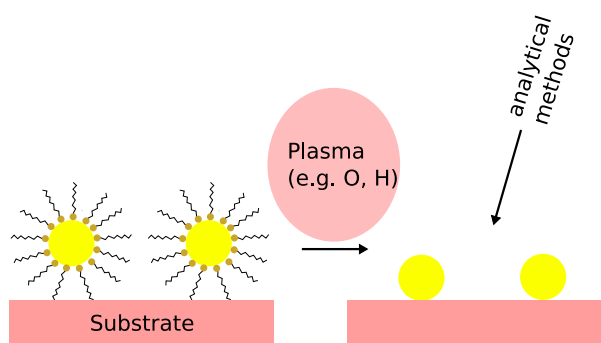


Figure A.11: Plasma etching procedure: The passivated particles are exposed to a plasma in order to burn away the organic components.

⁷The drop should be placed at the center of rotation

A.4 A Pedestrian's Guide to Band Structure Calculations

A.4.1 Density Functional Theory

Introduction

One of the most widely used theoretical approaches to band structure calculations is the so-called *Density Functional Theory* (DFT). This short overview should give the reader an idea about the basic principles behind this method. DFT calculations are widely used in solid state physics when it comes to band structure calculations and are therefore a useful mathematical tool for nanoscience, where scientifically interesting changes in electronic properties are expected. As the exact calculation of band structures in solids requires to solve many-body equations, simplifications have to be applied in order to apply feasible mathematical methods. These include

- the *free-electron approximation*, reducing the electron-ion interaction to a simple 'background' potential and thus neglecting the discreteness of the ions
- the *independent-electron approximation*, neglecting the electron-electron interactions
- self-consistent field approximations, which are recurring algorithms to treat electron-electron and electron-ion interactions with mean field potential values
- the quasi-particle formalism for interaction electrons, called *Landau's Fermi Liquid description*.

Starting with self-consistent approximations field approximations, solid state band theory has proven to be a very useful tool in the field of physics of metals and semiconductors. The further development can be summarized as follows[147]:

- Thomas-Fermi-Dirac theory
- Slater's X_α method and local density ($\rho^{1/3}$) approximation
- Slater's augmented plane wave method
- Hohenberg-Kohn-Sham density functional theory (*)
- Pseudopotential methods
- Tight-binding theories
- The Korringa-Kohn-Rostocker Green's functions method
- Linear band structure methods
- Iterative diagonalization or Car-Parrinello method (*)
- Embedded atom method and effective medium theories
- Linear scaling or order-N methods

The two methods marked with (*) will be described in the following sections as they are the basis of many band structure calculations and are themselves elegant methods of solving the Hamiltonian. The mathematical deductions will loosely follow Ref. [148] and [147].

DFT

When treating very simple systems like the hydrogen atom, electron orbitals energies can be calculated in a exact analytical manner starting with the cooresponding Hamiltonian:

$$[-\nabla^2 + V(r)]\psi_n = E_n\psi_n$$

with $V(r) = -\frac{2}{r}$.

Complications arise when going to high-Z elements, as the increased number of electrons and their interaction with each other and the nucleus makes it impossible to find the appropriate $V(r)$ and to solve the Hamiltonian analytically. This is where DFT comes into play, as it tries to find a suitable $V(fr)$ by varying the electron charge density function $\varrho(r)$. Hohenberg and Kohn have could show, that there is a correspondence between the charge density function $\rho(r)$ and an external potential V_{ext} imposed by the ion nuclei on the electrons. This means, for a fixed V_{ext} the *total energy functional* has a minimum (E_0) for a certain ρ_0 and this ρ_0 describes the electronic density of the ground state. In a more mathematical manner:

$$E_0[\varrho_0] = \min E[\varrho]$$

The square brackets are used in order to indicate that ρ itself is a function and not a variable. In analogy to the standard derivatives, this condition can be written

$$\frac{\delta}{\delta\varrho} E[\varrho] = 0$$

The total energy functional can be written in the following form:

$$E[\varrho] = T_0 + \underbrace{\frac{e^2}{2} \int \int \frac{\varrho(\vec{r})\varrho(\vec{r}')}{|\vec{r} - \vec{r}'|} d\vec{r} d\vec{r}'}_{E_H} + \underbrace{\int \varrho(\vec{r})V_{ext}(\vec{r}) d\vec{r}}_{E_{ext}} + E_{xc}[\varrho] \quad (\text{A.1})$$

where T_0 is the kinetic energy of a system of non-interacting electrons with the same density as the real system, E_H is the electron-electron Coulomb (or Hartree) energy, E_{ext} is the electron-ion Coulomb energy, and E_{xc} is the energy due to electron exchange and correlation effects and also contains the difference between T_0 and the real kinetic energy of the electrons. As we are regarding non-interacting electrons, the electron density can be expressed by independent single-particle orbitals φ_i

$$\varrho(\vec{r}) = \sum_{i=1}^N |\varphi_i(\vec{r})|^2.$$

The φ_i are known as *Kohn-Sham orbitals*.

To find the minimum of $E[\varrho] \equiv E[\varphi_i]$ one has to apply the variational principle and obtains the Euler equation

$$\frac{\delta}{\delta\varphi^*} \left[E[\varphi_i] - \sum_{k,l=1}^N \lambda_{kl} \left(\int \varphi_k^*(\vec{r})\varphi_l(\vec{r}) d\vec{r} - \delta_{kl} \right) \right] = 0, \quad (\text{A.2})$$

where the integral defines the constraint of orthogonality for wavefunctions φ_i .

It is worth mentioning that the Lagrange multipliers λ_{kl} describe in fact the chemical potential of the system. After performing the functional derivatives, one obtains the Kohn-Sham equation

$$H^{KS}\varphi_i(\vec{r}) = \lambda_i\varphi_i(\vec{r})$$

with

$$H^{KS} = -\frac{\hbar^2}{2m_e}\nabla^2 + e^2 \underbrace{\int \frac{\sum_{k=1}^N |\varphi_k(\vec{r}')|^2}{|\vec{r} - \vec{r}'|} d\vec{r}'}_{v_H(\vec{r})} + V_{ext} + \underbrace{\frac{\delta E_{xc}}{\delta \rho}}_{v_{xc}(\vec{r})}, \quad (\text{A.3})$$

the so-called Kohn-Sham Hamiltonian.

Once the φ_i have been found, it is possible to calculate the total energy E_0 :

$$E_0[\rho_0] = \sum_{j=1}^N \int \varphi_j^*(\vec{r}) \frac{-\hbar^2}{2m_e} \nabla^2 \varphi_j(\vec{r}) d\vec{r} + \frac{1}{2} \int v_H(\vec{r}) \rho_0(\vec{r}) d\vec{r} + \int V_{ext}(\vec{r}) \rho_0 d\vec{r} + E_{xc}[\rho_0]. \quad (\text{A.4})$$

By comparing (A.4) with the ground state expectation value of (A.3) an alternative expression for the total energy can be found:

$$E_0[\rho_0] = \sum_{j=1}^N \lambda_j + E_{xc}[\rho_0] - \int \rho_0 \left[\frac{1}{2} v_H(\vec{r}) + v_{xc}(\vec{r}) \right] d\vec{r}.$$

This term is used in practice in computational schemes. However, the exact form of E_{xc} is usually not known, as this would implicate, that the solution for the whole many-body problem is found. Therefore, appropriate approximations have to be introduced, of which the *Local Density Approximation* (LDA) is one of the most used ones. LDA is based on the assumption, that the exchange-correlation (XC) energy is mainly influenced by the *local* electron density and therefore long-range interactions can be neglected. This allows to substitute the XC energy of the inhomogeneous electron density of the real system by a XC energy $\varepsilon_{xc}^{hom}[\rho]$ of a homogeneous infinite electron gas with the local density $\rho(\vec{r})$. This leads to

$$E_{xc}^{LDA} \simeq \int \rho(\vec{r}) \varepsilon_{xc}[\rho(\vec{r})] d\vec{r}.$$

The exchange-correlation potential $v_{xc}(\vec{r})$ becomes

$$v_{xc}(\vec{r}) = \frac{\delta}{\delta \rho(\vec{r})} E_{xc}[\rho] = \varepsilon_{xc}^{hom}(\rho(\vec{r})) + \rho(\vec{r}) \frac{\partial \varepsilon_{xc}^{hom}}{\partial \rho}.$$

The XC energy of a homogeneous electron gas can be calculated by means of many-body perturbation theory and Monte Carlo methods and.

A.4.2 Car-Parrinello Molecular Dynamics (CP MD)

Introduction

As it was shown in the last section, DFT is a powerful tool for obtaining electron orbitals by ab-initio calculations. However, the atomic nuclei were supposed to be fixed and their Coulomb potential only appears as V_{ext} in DFT calculations. Classical molecular dynamics gave the possibility to compute various thermodynamic quantities and finite temperature properties by dealing with ion trajectories taking into account inter-atomic potentials and explicit quantum mechanical descriptions of electronic orbitals. In 1985 Car and Parrinello proposed a technique to combine DFT with molecular dynamics which allows to calculate atomic ion geometries *and* electronic states from first principles. One important benefit of this new scheme is, that no diagonalization of the KS-Hamiltonian has to be performed to find the φ_i wavefunctions. Instead, a dynamic algorithm is employed to minimize the total energy functional. For a system with fixed atomic ions, the results obtained from CP MD are the same as the ones from standard DFT, reflecting that CP MD introduces a different kind of computational scheme, but still having its roots in DFT. The basic concepts of this method shall be shortly described as they are widely applied (among many other fields) in cluster science.

Applying Molecular Dynamics Methods to DFT

The classical Lagrangian has to be redefined to be applicable to Kohn-Sham wavefunctions. The new Lagrangian L_{CP} has the form

$$L_{CP} = T_{ions} + T_{fake} - (U - \sigma) \quad (\text{A.5})$$

The term

$$T_{ions} = \frac{1}{2} \sum_{n=1}^{N_{at}} M_n \dot{\vec{R}}_n^2$$

describes the classical kinetic energy of the ions and

$$T_{fake} = \tilde{\mu} \sum_{i \in occ} \int \dot{\varphi}_i^* \dot{\varphi}_i$$

is called the *fake kinetic energy*. This term has nothing to do with the real kinetic energy of the electronic system, but was introduced to account for a time dependence of the Kohn-Sham orbitals $\varphi_i = \varphi_i(r; t)$. It will turn out later that this term plays an important role in the CP MD algorithm. In analogy to the real kinetic energy $\tilde{\mu}$ is called *fictitious mass*.

The last part in (A.5) looks more familiar when substituting

$$U = E^{DFT}[\{\varphi_i\}, \{\vec{R}_n\}],$$

which is the DFT electronic total energy functional as in (A.1) and

$$\sigma = \sum_{ij} \lambda_{ij} \int \varphi_j^* \varphi_i - \delta_{ij},$$

which is the constraint for orthogonality of the wavefunctions. It is now easy to see that the term $(U - \sigma)$ corresponds to (A.2) (except the functional derivative) in the DFT scheme. Calculation of the equations of motion from (A.5) yields:

$$\begin{aligned} \frac{\delta L}{\delta \varphi_i^*} &= \tilde{\mu} \dot{\varphi}_i \\ \Rightarrow \tilde{\mu} \ddot{\varphi}_i(r; t) &= -\frac{\delta}{\delta \varphi_i^*} E[\{\varphi_i\}; \{\vec{R}_n\}] + \sum_j \lambda_{ij} \varphi_j \end{aligned} \quad (\text{A.6})$$

$$\begin{aligned} \frac{\delta L}{\delta \dot{\vec{R}}_j^*} &= M_j \dot{\vec{R}}_j \\ \Rightarrow M_j \ddot{\vec{R}}_j &= -\frac{\partial}{\partial \vec{R}_n} E[\{\varphi_i\}; \{\vec{R}_n\}] \end{aligned} \quad (\text{A.7})$$

The results are two formally classical equations of motion which describe the time-dependence of the Kohn-Sham orbitals $\varphi_i(r; t)$ (A.6) and the motion of the atomic ions (A.7). Let us now consider the case of fixed ions: We only have to take care of equation (A.6), as for fixed ions $\ddot{\vec{R}}_i = \dot{\vec{R}}_i = 0$. Integration of (A.6) can be done numerically, using algorithms known from classical molecular dynamics. We now have a very elegant way to find the KS orbitals. In exact analogy to a mass in a gravitational potential the orbitals "move" in the potential defined by $(U - \sigma)$. Starting with a random set of orthogonal wavefunctions $\{\varphi_i^{random}(r; t_0)\}$, the φ_i are "dragged" towards the potential minimum. Different "damping" methods can be applied to prevent the wavefunctions of moving out of the minimum again.

This *simulated annealing* leads to $\{\varphi_i\}$ for which $(U - \sigma)$ is minimal and $\dot{\varphi}_i = \ddot{\varphi}_i = 0$. Thus, the Kohn-Sham equations are solved and $\varrho_0 = \sum_{i=1}^N |\varphi_i|^2$ can be calculated.

In the next step, ionic motion are taken into account, which mean, we have to additionally consider equation (A.7). One has to remind that (only) if the φ_i (which minimize $E[\{\varphi_i\}, \{\vec{R}_n\}]$) are found, (A.7) defines the forces $F_i(t)$ upon the ions:

$$M_i \ddot{\vec{R}}_i = - \frac{\partial}{\partial \vec{R}_n} E[\{\varphi_j\}; \{\vec{R}_n\}] \equiv F_i(t)$$

It appears that (A.6) and (A.7) are coupled and therefore cannot be solved easily. However, by choosing a very small value for $\tilde{\mu}$ (the "fictitious mass" of the KS-orbitals, which is an arbitrary value) compared to the real ionic mass, the system changes into heavy masses coupled to tiny masses. Classical mechanics show that there is poor energy transfer between these systems, which means, that despite the atomic motion, the electrons stay in their ground state⁸. This is indeed a different formulation of the well-known Born-Oppenheimer-Approximation. This allows to solve the KS-equations once and then perform the MD calculations for the ions.

⁸This is not exactly true, as there surely is a energy transfer, but on a very long time scale compared to the atomic motion

Bibliography

- [1] http://www.nano.gov/html/facts/the_scale_of_things.html.
- [2] R. Avni, D. Bouchier, G. Gautherin, K. Klabunde, H. Matsunami, M. Murakami, G. Nieman, C. Schwebel, A. Segmüller, M. Venugopalan, J. Webb, C. Weissmantel, *Thin films from Free Atoms and Particles*, Academic Press (1985).
- [3] <http://www.thebritishmuseum.ac.uk/science/lycurguscup/sr-lycugus-p1.html>.
- [4] D. J. Barber, I. C. Freestone, *Archeometry* 32 (1990) 33.
- [5] K. Nassau, *The Physics and Chemistry of Color*, John Wiley & Sons, Inc. (2001).
- [6] F. Antonii, *Panacea Aurea-Auro*, Bibliopolio Frobeniano: Hamburg (1618).
- [7] M. Mason, *Phys. Rev. B* 27 (1983) 748.
- [8] Y. Hu, T. J. Wagener, Y. Gao, H. M. Meyer III, J. H. Weaver, *Phys. Rev. B* 38 (1988) 3037.
- [9] R. Kubo, A. Kawabata, S. Kobayashi, *Annu. Rev. Mater. Sci.* 14 (1984) 49.
- [10] P. Buffat, J. P. Borrel, *Phys. Rev. A* 13 (1976) 2287.
- [11] T. P. Martin, Y. Naher, H. Schaber, U. Zimmermann, *J. Chem. Phys.* 100 (1994) 2322.
- [12] B. Wang, H. Wang, H. Li, C. Zeng, J. G. Hou, *Phys. Rev. B* 63 (2000) 35403.
- [13] T. Sato, H. Ahmed, D. Brown, B. Johnson, *J. Appl. Phys.* 82 (1997) 696.
- [14] V. Torma, T. Reuter, M. Schumann, G. Schmid, *Chem. Phys. Chem.* (2001) 546.
- [15] R. Barnett, C. Cleveland, H. Häkkinen, U. Landman, *Eur. Phys. J. D* 9 (1999) 95.
- [16] K.-H. Park, M. Shin, J. S. Ha, W. Soo Yun, Y.-J. Ko, *Appl. Phys. Lett.* 75 (1999) 139.
- [17] A. Shipway, E. Katz, I. Willner, *ChemPhysChem* 1 (2000) 18.
- [18] M. Alvarez, J. Khoury, T. Schaff, R. Whetten, *J. Phys. Chem. B* 101 (1997) 3706.
- [19] S. Linden, J. Kuhl, H. Giessen, *Phys. Rev. Lett.* 86 (2001) 4688.
- [20] G. Lamprecht, G. Schider, R. Lechner, H. Ditlbacher, F. Aussenegg, *Phys. Rev. Lett.* 84 (2000) 4721.
- [21] N. Felidj, J. Aubard, G. Levi, *Phys. Rev. B* 65 (2002) 75419.

- [22] S. Varganov, R. Olson, M. Gordon, *J. Chem. Phys.* 119 (2003) 2531.
- [23] A. Cho, *Science* 299 (2003) 1684.
- [24] G. Bauer, J. Hassmann, H. Walter, C. Mayer, T. Schalkhammer, *Nanotechnology* 14 (2003) 1289.
- [25] M.-H. Schaffner, J.-F. Jeanneret, F. Patthey, W.-D. Schneider, *J. Phys. D: Appl. Phys.* 31 (1998) 3177.
- [26] X. M. Lin, H. M. Jaeger, C. Sorensen, K. Klabunde, *J. Phys. Chem. B* 105 (2001) 3353.
- [27] M. Hostetler, J. Wingate, C.-J. Zhong, R. Murray, *Langmuir* 14 (1998) 17.
- [28] M. Brust, M. Walker, D. Bethell, D. Shiffrin, R. Whyman, *J. Chem. Soc. Chem. Commun.* (1994) 801.
- [29] M. Brust, C. Kiely, *Colloids Surfaces A* 202 (2002) 175.
- [30] J. P. Wilcoxon, J. E. Martin, F. Parsapour, B. Wiedenman, D. F. Kelley, *J. Chem. Phys.* 108 (1998) 9137.
- [31] D. Leff, P. Ohara, J. Heath, W. Gelbart, *J. Phys. Chem.* 99 (1995) 7036.
- [32] C. Gutierrez-Wing, P. Santiago, J. Ascencio, A. Camacho, M. Jose-Yamacan, *Appl. Phys. A* 71 (2000) 237.
- [33] H. Kroto, J. R. Heath, S. C. O'Brien, R. F. Curl, R. Smalley, *Nature* 318 (1985) 162.
- [34] R.C. Haddon, *Phil. Trans. R. Soc. Lond. A* 343 (1993) 53.
- [35] R. C. Haddon, *Acc. Chem. Res.* 21 (1988) 243.
- [36] R. Taylor, J. P. Hare, A. K. Abdul-Sada, H. W. Kroto, *J. Chem. Soc. Chem. Commun.* 20 (1990) 1423.
- [37] D. Dubois, K. M. Kadish, S. Flanagan, L. J. Wilson, *J. Am. Chem. Soc.* 113 (1991) 7773.
- [38] R. W. Lof, M. A. van Veenendaal, B. Koopmans, H. T. Jonkman, G. A. Sawatzky, *Phys. Rev. Lett.* 68 (1992) 3924.
- [39] M. S. Dresselhaus, G. Dresselhaus, P. C. Eklund, *Science of Fullerenes and Carbon Nanotubes*, Academic, San Diego (1996).
- [40] C. S. Yannoni, R. D. Johnson, G. Meijer, D. S. Bethune, J. R. Salem, *J. Phys. Chem.* 95 (1991) 9.
- [41] R. Tycko, R. H. Haddon, G. Dabbagh, S. H. Glarum, D. C. Douglass, A. M. Mujsce, *J. Phys. Chem.* 95 (1991) 518.
- [42] M. C. Hunt, A. Rajogopal, R. Caudano, P. Rudolf, *Surf. Sci.* 454-456 (2000) 267.
- [43] S. Bosi, T. Da Ros, G. Spalluto, M. Prato, *Eur. J. Med. Chem.* 38 (2003) 913.
- [44] J.-F. Nierengarten, *New. J. Chem.* 28 (2004) 1177.

- [45] P. C. Eklund, A. M. Rao, P. Zhou, Y. Wang, J. M. Holden, *Thin Solid Films* 257 (1995) 185.
- [46] M. R. C. Hunt, J. Schmidt, R. Palmer, *Phys. Rev. B* 60 (1999) 5927.
- [47] E. Alvarez-Zauco, H. Sobral, E. V. Basiuk, J. M. Saniger-Blesa, M. Villagran-Muniz, *Appl. Surf. Sci.* 248 (2005) 243.
- [48] T. R. Ohno, Y. Chen, S. E. Harvey, G. H. Kroll, J. H. Weaver, *Phys. Rev. B* 44 (1991) 13747.
- [49] G. K. Wertheim, D. N. E. Buchanan, *Phys. Rev. B* 50 (1994) 11070.
- [50] K.-D. Tsuei, J.-Y. Yuh, R.-Y. Chu, K.-L. Tsang, *Phys. Rev. B* 56 (1997) 15412.
- [51] A. F. Hebard, M. J. Rosseinsky, R. C. Haddon, D. W. Murphy, S. H. Glarum and T. T. M. Palstra, A. P. Ramirez, A. R. Kortan, *Nature* 350 (1991) 600.
- [52] K. Tanigaki, T. W. Ebbesen, S. Saito, J. Mizuki, J. S. Tsai, Y. Kubo, S. Kuroshima, *Nature* 352 (1991) 222.
- [53] Stefan Hüfner, *Photoelectron Spectroscopy*, Springer (2003).
- [54] J. Braun, *Rep. Prog. Phys.* 59 (1996) 1267.
- [55] M. Seidl, K.-H. Meiwes-Broer, M. Brack, *J. Chem. Phys.* 95 (1991) 1295.
- [56] S.B. DiCenzo, S.D. Berry, E.H. Hartford, *Phys. Rev. B* 38 (1988) 8465.
- [57] G. K. Wertheim, S. B. DiCenzo, D. N. E. Buchanan, *Phys. Rev. B* 33 (1986) 5384.
- [58] H. Hövel, B. Grimm, M. Pollmann, B. Reihl, *Phys. Rev. Lett.* 81 (1998) 4608.
- [59] H. Hövel, B. Grimm, M. Pollmann, B. Reihl, *Eur. Phys. J. D* 9 (1999) 595.
- [60] H. Hövel, I. Barke, H.-G. Boyen, P. Ziemann, M. G. Garnier, P. Oelhafen, *Phys. Rev. B* 70 (2004) 045424.
- [61] T. Ishida, N. Choi, W. Mizutani, *Langmuir* 15 (1999) 6799.
- [62] D. Zerulla, T. Chasse, *Langmuir* 15 (1999) 5285.
- [63] K. Heister, M. Zharnikov, M. Grunze, *Langmuir* 17 (2001) 8.
- [64] D. Krüger, H. Fuchs, R. Rousseau, D. Marx, M. Parrinello, *J. Chem. Phys.* 115 (2001) 4776.
- [65] R. Terrill, T. Postlethwaite, C. Chen, R. Murray, *J. Am. Chem. Soc.* 117 (1995) 12537.
- [66] A. Badia, S. Singh, L. Demers, L. Cuccia, R. Brown, R. B. Lennox, *Chem. Eur. J* 2 (1996) 359.
- [67] C. Gutierrez-Wing, J. Ascencio, M. Perez-Alvarez, M. Marin-Almaz, M. Jose-Yamacan, *J. Cluster Sci.* 9 (1998) 529.
- [68] M. Porter, T. Bright, D. Allara, C. Chidsey, *J. Am. Chem. Soc.* 109 (1987) 3559.

- [69] W. D. Luedtke, U. Landman, *J. Phys. Chem.* 100 (1996) 13323.
- [70] R. C. Baetzold, *J. Appl. Phys.* 47 (1976) 3799.
- [71] G.K. Wertheim, S.B. DiCenzo, S.E. Youngquist, *Phys. Rev. Lett.* 51 (1983) 2310.
- [72] D.-Q. Yang, E. Sacher, *Surf. Sci.* 516 (2002) 43.
- [73] B. An, S. Fukuyama, K. Yokogawa, *J. Appl. Phys.* 92 (2002) 2317.
- [74] H.-G. Boyen, G. Kästle, F. Weigl, P. Ziemann, G. Schmid, M. G. Garnier, P. Oelhafen, *Phys. Rev. Lett.* 87 (2001) 276401.
- [75] O. Häberlen, S.-C. Chung, N. Rösch, *J. Chem. Phys.* 106 (1997) 5189.
- [76] W. Egelhoff, G. Tibbetts, *Phys. Rev. B* 19 (1979) 5028.
- [77] P. Wynblatt, J.-J. Metois, J.-C. Heyraud, *J. Crystal Growth* 102 (1990) 618.
- [78] A. Howells, L. Hung, G. Chottiner, D. Scherson, *Solid State Ionics* 150 (2002) 53.
- [79] Y.-O. Ahn, M. Seidl, *J. Appl. Phys.* 77 (1995) 5558.
- [80] H.-G. Boyen, G. Kästle, F. Weigl, B. Koslowski, C. Dietrich, P. Ziemann, J. P. Spatz, S. Riethmüller, C. Hartmann, M. Möller, G. Schmid, M. G. Garnier, P. Oelhafen, *Science* 297 (2002) 1533.
- [81] J. K. Gibson, *J. Vac. Sci. Technol. A* 16 (1998) 653.
- [82] C. G. Granqvist, R. A. Buhrman, *J. Appl. Phys.* 47 (1976) 2200.
- [83] H.-G. Boyen, Th. Herzog, G. Kästle, F. Weigl, P. Ziemann, J. P. Spatz, M. Möller, R. Wahrenberg, M. G. Garnier, P. Oelhafen, *Phys. Rev. B* 65 (2002) 075412.
- [84] T. Ohgi, D. Fujita, *Phys. Rev. B* 66 (2002) 11540.
- [85] H.-G. Boyen, A. Ethirajan, G. Kästle, F. Weigl, P. Ziemann, G. Schmid, M. G. Garnier, M. Büttner, P. Oelhafen, *Phys. Rev. Lett.* 94 (2005) 016804.
- [86] C. N. Rao, G. Kulkarni, A. Govindaraj, P. Thomas, *Pure Appl. Chem.* 72 (2000) 21.
- [87] R. J. Baird, L. F. Wagner, C. S. Fadley, *Phys. Rev. Lett.* 37 (1976) 111.
- [88] K. Fauth, M. Heßler, D. Batchelor, G. Schütz, *Surf. Sci.* 529 (2003) 397.
- [89] R. Anton, R. Behling, M. Harsdorff, C. Kleinschmidt, *Thin Solid Films* 140 (1986) 291.
- [90] <http://www.srim.org/index.htm>.
- [91] K. J. Taylor, C. L. Petiette-Hall, O. Cheshnovsky, R. E. Smalley, *J. Chem. Phys.* 96 (1992) 3319.
- [92] H. Häkkinen, B. Yoon, U. Landman, *J. Chem. Phys. A* 107 (2003) 6168.
- [93] A. A. Schmidt, H. Eggers, K. Herwig, R. Anton, *Surf. Sci.* 349 (1996) 301.
- [94] Ignacio Lopez-Salido, Dong Chan Lim, Young Dok Kim, *Surf. Sci.* 588 (2005) 6.

- [95] A. F. Carley, M. W. Roberts, Proc. R. Soc. Lond. A 363 (1978) 403.
- [96] R. Werner, M. Wanner, G. Schneider, D. Gerthsen, Phys. Rev. B 72 (2005) 045426.
- [97] S. Schelz, T. Richmond, P. Kania, P. Oelhafen, H.-J. Güntherodt, Surf. Sci. 359 (1996) 227.
- [98] M. Büttner, T. Belser, P. Oelhafen, J. Phys. Chem. B 109 (2005) 5464.
- [99] M. A. Garcia, J. de la Venta, P. Crespo, J. Lopic, S. Penades, A. Fernandez, A. Hernando, Phys. Rev. B 72 (2005) 241403(R).
- [100] H. Schmidbaur, S. Cronje, B. Djordjevic, O. Schuster, Chem. Phys. 311 (2005) 151.
- [101] K. Nobusada, J. Phys. Chem. B 108 (2004) 11904.
- [102] J. A. Larsson, M. Nolan, J. C. Greer, J. Phys. Chem. B 106 (2002) 5931.
- [103] J. Hrbek, M. Kuhn, J. A. Rodriguez, Surf. Sci. 356 (1996) L423.
- [104] F. Tast, N. Malinowski, I. M. L. Billas, M. Heinebrodt, W. Branz, T. P. Martin, J. Chem. Phys. 107 (1997) 6980.
- [105] S. Saito, A. Oshiyama, Phys. Rev. B 44 (1991) 11532.
- [106] Ryuichiro Maruyama, J. Appl. Phys. 94 (2003) 6871.
- [107] P. Reinke, P. Oelhafen, J. Chem. Phys. 116 (2002) 9850.
- [108] P. Reinke, P. Oelhafen, S. Christiansen, Surf. Sci. 507-510 (2002) 630.
- [109] P. Reinke, H. Feldermann, P. Oelhafen, J. Chem. Phys. 119 (2003) 12547.
- [110] Hendrik Ulbricht, Gunnar Moos, Tobias Hertel, Phys. Rev. Lett. 90 (2003) 095501.
- [111] H. P. Bonzel, Ch. Kleint, Prog. Surf.Sci. 49 (1995) 107.
- [112] H. Hertz, Ann. Physik 31 (1887).
- [113] W. Hallwachs, *Handbuch der Radiologie*, Akadem. Verlagsges. Leipzig (1916).
- [114] P. Lenard, Ann. Phys. 2 (1900) 359.
- [115] P. Lenard, Ann. Phys. 8 (1902) 147.
- [116] Albert Einstein, Ann. Physik 17 (1905) 132.
- [117] Jr. R. G. Steinhardt, E. J. Serfass, Anal. Chem. 23 (1951) 1585.
- [118] C. Nordling, E. Sokolowski, K. Siegbahn, Phys. Rev. 105 (1957) 1676.
- [119] K. Siegbahn, Ark. Fys. 7 (1954) 86.
- [120] K. Siegbahn, C. Nordling, A. Fahlmann, R. Nordberg, K. Hamrin, J. Hedman, G. Johansson, T. Bergmark, S. E. Karlsson, I. Lindgren, B. Lindberg, *ESCA - Atomic, Molecular and Solid State Structures Studied by Means of Electron Spectroscopy*, Almqvist and Wiksells, Uppsala (1967).

- [121] K. Siegbahn, C. Nordling, G. Johansson, J. Hedman, O. F. Heden, K. Hamrin, N. Gelius, T. Bergmark, L. O. Werme, R. Manne, Y. Baer, *ESCA Applied to Free Molecules*, North-Holland, Amsterdam (1969).
- [122] K. Siegbahn, C. Nordling, E. Sokolowski, in *Proc. Rehovoth Conf. Nucl. Str.*, North-Holland, Amsterdam (1970) .
- [123] J. A. Venables, *Introduction to Surface and Thin Film Processes*, Cambridge University Press (2000).
- [124] E. Bauer, *Z. Kristallogr.* 110 (1958) 372.
- [125] T. A. Witten, L. M. Sander, *Phys. Rev. Lett.* 47 (1981) 1400.
- [126] T. A. Witten, L. M. Sander, *Phys. Rev. B* 27 (1983) 5686.
- [127] R. Nishitani, A. Kasuya, S. Kubota, Y. Nishina, *J. Vac. Sci. Technol. B* 9 (1991) 806.
- [128] P. Jensen, *Rev. Mod. Phys.* 71 (1999) 1695.
- [129] R. Anton, I. Schneiderreit, *Phys. Rev. B* 58 (1998) 13874.
- [130] N. Vandamme, E. Janssens, F. Vanhoutte, P. Lievens, C. Van Haesendonck, *J. Phys.: Condens. Matter* 15 (2003) S2983.
- [131] J. Carrey, J.-L. Maurice, F. Petroff, A. Vaures, *Phys. Rev. Lett.* 86 (2001) 4600.
- [132] J. Turkevitch, P. C. Stevenson, J. Hillier, *Discuss. Faraday Soc.* 11 (1951) 55.
- [133] G. Frens, *Nature: Phys. Sci.* 241 (1973) 20.
- [134] Zsigmondy, *Das kolloidale Gold*, Akademische Verlagsgesellschaft. Leipzig (1925).
- [135] C. Larpent, H. Patin, *J. Mol. Catal.* 44 (1988) 191.
- [136] G. Schmid, A. Lehnert, *Angew. Chem., Int. Ed. Engl.* 28 (1989) 780.
- [137] G. Schmid, A. Lehnert, U. Kreibitz, Z. Adamczyk, P. Belouschek, *Z. Naturforsch.* 45b (1990) 989.
- [138] G. Schmid, *Chem. Rev.* 92 (1992) 1709.
- [139] H. Zhang, G. Schmid, U. Hartmann, *Nano Lett.* 3 (2003) 305.
- [140] G. Schmid, R. Pfeil, R. Boese, F. Bandermann, S. Meyer, G. H. M. Calis, J. W. A. van der Velden, *Chem. Ber.* 114 (1981) 3634.
- [141] M.-C. Daniel, D. Astruc, *Chem. Rev.* 104 (2004) 293.
- [142] M. Giersing, P. Mulvaney, *Langmuir* 9 (1993) 3408.
- [143] M. Hostetler, A. C. Templeton, R. W. Murray, *Langmuir* 15 (1999) 3782.
- [144] J. E. Martin, J. Wilcoxon, J. Odinek, P. Provencio, *J. Phys. Chem. B* 104 (2000) 9475.
- [145] A. Ulman, *An Introduction to Ultrathin Organic Films*, Academic Press (1991).

- [146] A. S. Edelstein, R. C. Cammarata, editors, *Nanomaterials*, Institute of Physics (1998).
- [147] R. Haydock, G. Das, A. Mookerjee, R. Prasad, A. Arya, S. Banerjee, D. D. Sarma, N. Shanthi, T. Saha-Dasgupta, A. Finel, A. Mehta, *Electron Structure of Alloys, Surfaces and Clusters*, volume 4 of *Advances in condensed matter science*, Taylor & Francis (2003).
- [148] R.A. Broglia, G. Colo, G. Onida, H. E. Roman, *Solid State Physics of Finite Systems*, Advanced Texts in Physics, Springer (2004).

Acknowledgments / Danksagung

Die Durchführung einer Doktorarbeit, angefangen bei den ersten Planungen der Experimente, über die Realisation des experimentellen Aufbaus, der Ausführung der Experimente, bis hin zur schriftlichen Ausarbeitung der Ergebnisse, ist ohne Hilfe Anderer kaum zu denken. Ebenso in diesem Fall. Ich möchte daher an dieser Stelle folgenden Personen danken, die alle zum Entstehen dieser Arbeit ihren Teil dazu beigetragen haben:

- Herrn Professor Peter Oelhafen, der mich in seine Arbeitsgruppe aufgenommen und mir dadurch die Chance gegeben hat in einer angenehmen Arbeitsatmosphäre Forschung zu betreiben.
- Herrn Professor Christian Schönenberger für die Übernahme des Korreferats
- PD Dr. Hans-Gerd Boyen, der mir die Physik von Nanopartikeln nähergebracht und als externer Experte bei meiner Verteidigung teilgenommen hat.
- Roland Steiner für seinen Ideenreichtum bei der Lösung experimenteller Probleme und für seine Hilfe bei den diversen großen und kleinen Laborkatastrophen.
- Teresa de los Arcos für ihre Hilfe, die niedergeschriebenen Gedanken in meinen Manuskripten zu ordnen.
- den Mitarbeitern der E-Werkstatt, im einzelnen Michael Steinacher, Werner Erni und Bernd Heimann, für ihren Rat und ihre Unterstützung, wenn die Elektrik im Labor mal wieder streikte und im Besonderen während des Upgrades des ESCA3 Messprogramms und den dazu nötigen elektrischen Anpassungen.
- den Kollegen und Ehemaligen, die alle zum angenehmen Arbeitsklima in der ESCA-Gruppe beigetragen haben: Teresa de los Arcos, Jamila Boudaden, Michael Gunnar Garnier, Shui-Ching Ho, Dieter Kohler, Marc Ley, Iris Mack, Laurent Marot, Georges Reber, Andriy Romanyuk, Gregory de Temmerman, Ivan Videnovic
- Thomas Belser aus dem Institut für Organische Chemie für die gute Zusammenarbeit während der Experimente mit chemisch synthetisierten Goldpartikeln, die von ihm hergestellt wurden.
- Petra Reinke für hilfreiche Diskussionen bezüglich Fullerenen.
- Inga Hannstein für TEM-Messungen an meinen Goldcluster-Proben.
- weiteren Mitarbeitern der Uni Basel, die da wären: Cara Humphrey und Jonathan Medlock für Ihre sprachliche Hilfe bei der Ausarbeitung meines ersten Artikels, Tamara Fretz, Daniel Mathys und Marcel Düggelin vom Zentrum für Mikroskopie für die Anfertigung von TEM- und SEM-Aufnahmen.

- dem Schweizer Nationalfonds für die finanzielle Unterstützung meiner Arbeit.

Zum Schluß möchte ich meiner Familie, im Besonderen meiner Mutter, danken, die meine Arbeit stets unterstützt hat und mir in allen Situationen Rückhalt gegeben.

Danke Euch allen!

Curriculum Vitae

Persönliche Daten

Name: Michael Büttner
Eltern: Hans-Joachim und Wanda Büttner, geb. Lorenzi
geboren: 24.10.1974 in Göttingen, Deutschland
Nationalität: deutsch

Bildungsgang

6/1994 Abitur am Max-Planck-Gymnasium zu Göttingen

9/1994 - 11/1995 Ziviler Ersatzdienst im Universitätsklinikum Göttingen

11/1995 Beginn des Studiums der Physik im WS 95/96 an der Georg-August Universität Göttingen

11/99 - 5/2001 Diplomarbeit in der Gruppe Prof. Hofsäss, II. Physikalisches Institut, Universität Göttingen. Titel der Arbeit: 'Eigenschaften von fluoriertem diamantähnlichem amorphem Kohlenstoff, hergestellt durch massenseparierte Ionenstrahldeposition'

9/2001 - 1/2006 Doktorarbeit in Experimentalphysik in der Gruppe von Prof. Oelhafen, Institut für Physik, Universität Basel

An meiner Ausbildung waren neben weiteren die folgenden Dozentinnen und Dozenten beteiligt:

In Basel Herr Prof. P. Oelhafen

In Göttingen die Herren Professoren und Dozenten W. Felsch, H. Goenner, G. Hegerfeldt, H. Hofsäss, H. Holdgrün, R. Kree, W. Lauterborn, H. P. Lieb, G. von Minnigerode, H. Roesky, C. Ronning, H. Roos, G. Schmahl, K. Schönhammer, L. Smith, K. Winzer.

Publications

During doctoral studies

- M. Büttner, P. Reinke, and P. Oelhafen, *UPS studies on fullerene desorption from defect-rich carbon surfaces*, in preparation
- M. Büttner and P. Oelhafen, *XPS study on the Evaporation of Gold Submonolayers on Carbon Surfaces*, Surf. Sci. 600 (2006) 1170
- M. Büttner, H. Kröger, I. Gerhards, D. Mathys, and P. Oelhafen, *Changes in the electronic structure of gold particles upon thiol adsorption as a function of the mean particle size*, Thin Solid Films 496 (2006) 180
- M. Büttner, T. Belsler, and P. Oelhafen, *Stability of Thiol-Passivated Gold Particles at Elevated Temperatures Studied by X-ray Photoelectron Spectroscopy*, J. Phys. Chem. B 109 (2005) 5464-5467
- H.-G. Boyen, A. Ethirajan, G. Kästle, F. Weigl, P. Ziemann, G. Schmid, M. G. Garnier, M. Büttner, and P. Oelhafen, *Alloy Formation of Supported Gold Nanoparticles at Their Transition from Clusters to Solids: Does Size Matter?*, Phys. Rev. Lett. 94 (2005) 016804
- H.-G. Boyen, K. Fauth, B. Stahl, P. Ziemann, G. Kästle, F. Weigl, F. Banhart, M. Hessler, G. Schutz, N. S. Gajbhiye, J. Ellrich, H. Hahn, M. Büttner, M. G. Garnier, P. Oelhafen, *Electronic and magnetic properties of ligand-free FePt nanoparticles*, Advanced Materials 17 (2005) 574
- M. Manolova, V. Ivanova, D. M. Kolb, H.-G. Boyen, P. Ziemann, M. Büttner, A. Romanjuk, P. Oelhafen, *Metal deposition onto thiol-covered gold: Platinum on a 4-mercaptopyridine SAM*, Surf. Sci. 590 (2005) 146
- G. Kästle, A. Schröder, H.-G. Boyen, A. Plettl, P. Ziemann, O. Mayer, J. Spatz, M. Möller, M. Büttner, P. Oelhafen, *Electrical Resistivity of Epitaxial Au Films Surface-Modulated by Arrays of Pt Nanoparticles*, Eur. J. Inorg. Chem. (2005)
- H. Kröger, P. Reinke, M. Büttner, and P. Oelhafen, *Gold cluster formation on a fullerene surface*, J. Chem. Phys. 123 (2005) 114706
- P. Reinke, S. Eyhusen, M. Büttner, et al., *Interaction of Fe+ with the C-60 surface: A study about the feasibility of endohedral doping*, Appl. Phys. Lett. 84 (2004) 4373-4375
- T. Baunach, V. Ivanova, D. M. Kolb, H.-G. Boyen, P. Ziemann, M. Büttner, P. Oelhafen, *A New Approach to the Electrochemical Metallization of Organic Monolayers: Palladium*

Deposition onto a 4,4-Dithiodipyridine Self-Assembled Monolayer, Advanced Materials
Volume 16 (2004) 2024-2028

Earlier publications

- C. Ronning, M. Büttner, U. Vetter, et al., *Ion beam deposition of fluorinated amorphous carbon*, J. Appl. Phys. 90 (2001) 4237-4245
- C. Ronning, O. Wondratschek, M. Büttner, et al., *Superhard, conductive coatings for atomic force microscopy cantilevers*, Appl. Phys. Lett. 79 (2001) 3053-3055